Mechanobiological model of bone tissue regeneration on scaffolds

Marco Antonio Velasco Peña

Universidad Nacional de Colombia
Facultad de Ingeniería, Departamento de Ingeniería Mecánica y Mecatrónica
Bogotá, Colombia
2016

Mechanobiological model of bone tissue regeneration on scaffolds

Marco Antonio Velasco Peña

Thesis in partial fulfillment of
the requirements for the degree of:
Doctorate in Engineering – Materials Science and Technology

Director:
Ph.D. Eng., Diego Alexander Garzón Alvarado

Investigation Line:
Biomechanics

Universidad Nacional de Colombia
Facultad de Ingeniería, Departamento de Ingeniería Mecánica y Mecatrónica
Bogotá, Colombia
2016

To my beloved wife Laura

To my parents and brothers

Acknowledgements

I would like to thank all people who have helped me during my graduate study.

I specially want to thank my director Diego Alexander Garzón Alvarado, professor at the Doctorate in Engineering - Science and Technology of materials, for his wise, patient, and careful guidance in conducting this work, and the National University of Colombia for the human and professional quality of all its faculty and staff.

I also would like to express my sincere gratitude to Carlos Alberto Narváez and Yadira Lancheros, who worked with me writing research papers derived from this thesis.

To my brothers Leonardo and Hugo for their cooperation and encouragement.

To my wife, Laura, for her immense love, support, understanding, patience, and wisdom in difficult times.

Abstract

Scaffolds are one of the most used strategies of tissue engineering in the treatment of bone defects; they help to meet the mechanical function of load bearing that bones play in the human body. The design and fabrication of scaffolds made of biodegradable polymers is of particular interest. As they erode, scaffolds leave empty space that can be occupied by new regenerated bone. For the scaffold to meet the clinical requirements, it is vital to pay attention to the design of the geometry of the implant's porous structure, the manufacturing technique, and performance of the scaffold once implanted. To enter in this field, the development of a mechanobiological model of bone regeneration process on scaffolds is presented here. In this thesis, we are obtaining an irregular three-dimensional pattern using a reaction-diffusion. Degradation of a representative volume element of the scaffold is studied due to a hydrolysis process, and the regeneration of bone tissue on the scaffold is modeled. Finally, some scaffolds are manufactured using additive manufacturing to study its mechanical properties. In conclusion, it is found that the proposed geometry can be useful for the design of scaffolds and may be considered for future designs and experimental work in order to develop biodegradable scaffolds similar to trabecular bone.

Keywords: bone scaffold; regeneration; reaction-diffusion; finite element method.

Resumen

Los andamios son una de las estrategias de la ingeniería de tejidos que más se usa en el tratamiento de defectos óseos. Ellos ayudan a suplir la función mecánica de soporte de carga que desempeñan los huesos. El diseño y fabricación de andamios hechos de polímeros biodegradables resulta de especial interés. Mientras ellos se erosionan, dejan espacio vacío que puede ser ocupado por el nuevo hueso regenerado. Para lograr un andamio que cumpla los requerimientos clínicos se debe prestar atención al diseño de la geometría de la estructura porosa del implante, la técnica de fabricación y el desempeño del andamio una vez implantado. Para incursionar en este campo, se plantea el desarrollo de un modelo mecanobiológico del proceso de regeneración ósea sobre scaffolds. En esta tesis se desarrolla la obtención de un patrón tridimensional irregular

usando un sistema reacción-difusión, se estudia la degradación de un elemento representativo del volumen del andamio debido a un efecto de hidrólisis y se modela la regeneración de tejido óseo sobre el andamio. Finalmente, se fabrican algunos andamios mediante manufactura aditiva para revisar sus propiedades mecánicas. En conclusión, se encuentra que la geometría propuesta puede ser útil para el diseño de los andamios y puede ser considerada para futuros diseños y pruebas experimentales que ayuden a desarrollar andamios biodegradables similares al hueso trabecular.

Palabras clave: andamio hueso; la regeneración; reacción-difusión; método de elementos finitos.

Contents

Page

Figure list

Page

Table list

Introduction

One area of common interest for engineering, medicine, biochemistry and other disciplines is the study of materials and manufacturing processes required to produce scaffolds for bone regeneration. Progress in this field of tissue engineering is essential, since bone diseases are very common and they cause physical disability and inability to achieve quality of life.

There are many cases where injuries are not able to cure just with the help of mechanical fixing. This is because a bone portion has been lost or damaged. For these cases, it is necessary to fill the void space left using scaffolds made with biomaterials. Biomaterial is defined as "a compound pharmacologically inert designed to be implanted or incorporated within the living system." In this sense, the biomaterial is implanted in order to replace or regenerate tissues and achieve their functions. Bone regeneration materials are biocompatible materials that stimulate and support new bone growth.

Bone pathologies are a significant percentage in the inability of people. Bone tissue may suffer various diseases that could be caused by hormonal deficiencies, infection or excessive mechanical loads, among other reasons. Some of the diseases or pathologies of bone tissue are fractures, osteogenesis imperfecta, osteoporosis, osteomalacia, osteomyelitis and cancer. Factors such as age, industrial, or traffic accidents are the causes of the loss or damage of bone tissue. In Colombia, according to the Integrated Information System of Social Protection (SISPRO), 1.7 million people were diagnosed with diseases or injuries of the musculoskeletal system and connective tissue during 2013. This represents approximately 14% of the diseases diagnosed that year [1]. Also, the average age of the population has greatly increased, thereby growing cases of osteoporosis [2]. In Colombia, according to the National Administrative Department of

Statistics (DANE), life expectancy of Colombians rose nearly two years between 2005 and 2010.

Moreover, the events of the armed conflict in this country have caused victims suffering damage in bone tissues, which, in many cases, require reconstructive treatments. The Colombian National Observatory of Disability estimated that by April 2015, the number of people with disabilities, who are victims of armed conflict, were 149287 [3]. For example, a research done in 2006, showed that only the Central Military Hospital in Bogota received 348 wounded people in combat a year. About 70 of them needed reconstruction of bone tissue with procedures beyond fixing and immobilization [4]. From 1990 to March 2016, there have been 9162 injured by landmines and unexploded ammunition [5]. Often, the physical damage caused by these devices involve not only partially affected limb tissue loss but complete loss of limbs. All these victims need treatments that will help them restore their quality of life and overcome their disability.

It becomes necessary to rebuild damaged bone tissue to continue fulfilling its function. For these cases, tissue engineering developments where scaffolds are combined with stem cells and growth factors are the therapeutic strategies used in regenerative medicine. In the area of bone tissue, there can be found various companies and institutions around the world that provide some of these technologies. However, biomaterials are high cost and its availability is limited. As an example, a study argues that 1 g of bone substitute costs about 100 USD [6], while another notes that the cost of replacing organs was estimated at 8% of the cost of health throughout the world in 2009 [7]. In Colombia, 16198 bone grafts were distributed in 2012, 14568 in 2013 and 12484 in 2014. This is a decline of about 13% per year [8].

Therefore, it is advisable to study the mechanobiological process of bone regeneration on scaffolds. This would be useful to produce scaffolds that can improve the quality of life of patients who require it. With this in mind, the overall aim of the thesis is to make a computational model to evaluate in-silico by testing the bone regeneration process on a scaffold considering its geometrical and physicochemical properties. To achieve this goal, the following specific objectives have been proposed:

- Develop tools to generate three-dimensional patterns and to control its geometric characteristics.
- Simulate biomaterial implant degradation due to biochemical stimuli in in-vivo implantation.
- Simulate bone tissue growth on the scaffold due to external stimuli in in-vivo implantation.
- Establish the mechanical behavior of the scaffold during the process of bone regeneration.

The development of this thesis is as follows. In chapter 1 a review of the state of the art design and use in bone tissue engineering materials is made. Chapter 2 describes a methodology to generate porous structures from reaction-diffusion systems. In Chapter 3, the computer simulation of the degradation of a representative volume of a scaffold made of a biodegradable polyester hydrolysis by considering a mechanism element is presented. Chapter 4 discusses aspects to be considered in the modeling of bone regeneration process and presents a simulation of bone regeneration process. Finally, in Chapter 5 the process of design and manufacture of an implant designed with the methodology proposed in Chapter 2 is discussed.

1 Design and materials of biodegradable scaffolds for bone tissue engineering

In this chapter a review about design and manufacture of scaffolds for bone tissue engineering is presented. First, fundamental aspects about bone, tissue engineering, and considerations related to scaffold design are established. Second, issues related to scaffold biomaterials, and manufacturing processes are discussed.

1.1 Description of the bone tissue

Bones are rigid organs that consist of osseous tissue, bone marrow, endosteum, periosteum, cartilage, nerves, and vascular channels constituting the skeleton of vertebrate animals. Osseous tissue, which fulfills mechanical functions, is formed by connective tissue cells such as osteocytes, osteoblasts and osteoclasts in an extracellular matrix composed mainly of minerals, proteins, and water [9], [10]. The bone composition and configuration will vary according to factors such as the anatomical location, supported load, age, and gender of the individual, and the possible diseases that he or she could suffer [11], [12]. In regard to bone composition, the mineral phase is between 60 and 70 wt.%, water between 5 and 10 wt.%, while the remaining portion is an organic matrix of collagen and other proteins.

The mineral phase of bone is essentially a calcium phosphate, called hydroxyapatite, presented in the form of nanocrystals with sizes between 25 and 50 nm in length [13]. Variations in the chemical composition of hydroxyapatite modify its physical properties, specially its solubility [14]. On the other hand, biochemical properties mainly depend on the organic phase of the extracellular matrix of bone. Approximately 90% of the organic phase is formed by type I collagen. The remainder consists of proteins, lipids and other

macromolecules such as growth factors, cytokines, osteonectin, osteopontin, osteocalcin, osteoinductive proteins, sialoproteins, proteoglycans, phosphoproteins, and phospholipids [15]–[17]. The mineral and organic phases determine the mechanical properties of bone as a composite.

According to its structure, osseous tissue may be cancellous (trabecular) or cortical (lamellar). Cancellous bone is a network of interconnected porosities, ranging between 50 and 90%, with a solid portion which is formed of struts and plates that can adopt different configurations. It is located at the epiphysis of long bones and the interior of cuboid bones. Cortical tissue is located at the bone surface and it has a homogeneous and compact macrostructure. It is found mainly at the bone diaphysis and its thickness varies according to the bone anatomical location. The microscopic structure of cortical bone is composed of lamellar, plexiform and haversian tissue. The plexiform tissue is formed by layers in which there are channels to help bone vascularity. The haversian tissue is within the lamellar tissue, and surrounding the lacunae, or osteons where osteocytes reside. Osteons are arranged along the tissue and is a structural unit of the cortical bone. Figure 1-1 illustrates the types of osseous tissue and its components and Figure 1-2, the shape and variations of cancellous tissue.

Bones have mechanical, synthetic and metabolic functions. The mechanical functions are: protection of internal organs, body support and interaction with muscles and tendons to generate body movement [13]. The synthetic function is conducted by the bone marrow, where bone and blood cells are synthesized in a process called hematopoiesis [18]. Metabolic functions are related to act as a reservoir of calcium [19], phosphorus, growth factors and fat and the regulation of blood pH releasing alkaline salts [20].

Referring to mechanical function, bones are the structural elements of the human body. The skeletal system supports loads due to the different activities of an individual as holding things, walking, pushing, etc. These loads induce tensile, compressive or shear stresses on the bone tissue. More complex stresses such as those caused by bending or twisting of bone can be decomposed into the three basic aforementioned stresses. To study these stresses, bone mechanical properties such as elasticity modulus, compressive, and tensile strength are important. These properties are highly dependent on the position of the bone and the condition of the individual. Besides, mechanical

properties of bone vary depending on the load orientation with respect to the orientation of the tissue (anisotropy) and the speed to which the load is applied (viscoelasticity) [11], [21]. Ref. [22] provides a good source of data and models of mechanical properties for different types of human bones. Some important mechanical properties are listed in Table 1-1.

Figure 1-1: Types of bone tissue and its components. From: Meng et al. [23]

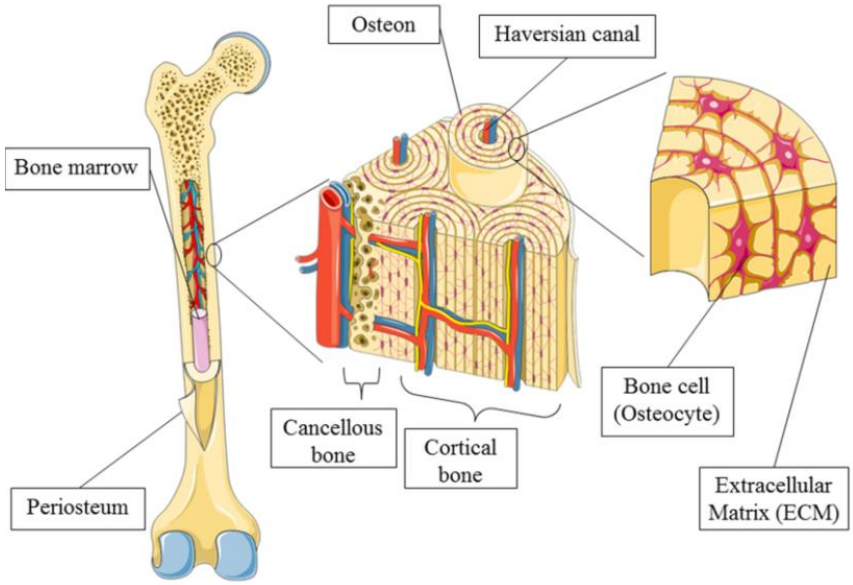

Figure 1-2: Shape and variations of spongy tissue. Top row: µCT in different bones of the same individual (lumbar spine, femoral head, and calcaneus Core). Bottom row: µCT of the same bone (iliac crest) of different individuals. From: Ma and Elisseeff [24]

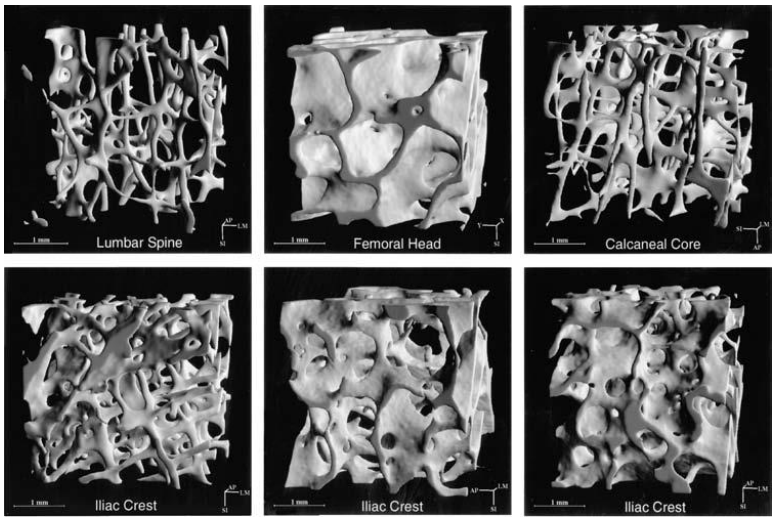

Table 1-1: Mechanical properties of bone. From: Bandyopadhyay-Ghosh [25] and Knudson [26]

PROPERTY	CORTICAL BONE	CANCELLOUS BONE
Tensile strength (MPa)	50-150	10-100
Compressive strength (MPa)	130-230	2-12
Young's Modulus (GPa)	7-30	0.02-0.5
Strain to failure (%)	1-3	5-7
Shear strength (MPa)	53-70	
Shear modulus (GPa)	3	

Other important physical property of osseous tissue is permeability that describes the porosity and interconnectivity of tissue. Permeability is estimated between $0.003x10^{-6}$ and $11x10^{-6}$ $m^4/N.s$ for trabecular bone in humans and $0.98x10^{-11}$ and $7.8x10^{-11}$ $m^4/N.s$ in cortical bone for canine and bovine animals [27]. A detailed explanation of permeability in bone can be found in Refs. [28], [29].

Bone tissue may suffer various diseases that can be caused by excessive load or hormonal deficiencies, among other reasons [30], [31]. Bone tissue, as an engineering material, can fail because mechanical loads originate stresses higher than the limit a healthy bone can bear, or because the mechanical properties of bone decreases by various pathologies making the bone weak and prone to be damaged. Some of the diseases of bone tissue are:

- Fracture: partial or total loss of bone continuity. It is caused by traumas by mechanical loads that exceed the allowable stresses of the bone. There may be associated factors to the extent allowable stresses are conditioned by other diseases that affect bone density. They can be classified by considering the type of trauma, fracture shape, the location, and direction of the load [32].
- Osteogenesis Imperfecta: bone embrittlement due to deficiencies in the collagen matrix [33].
- Osteoporosis: Loss of bone minerals by hormonal deficiencies [34].
- Osteomalacia or rickets: Loss of bone mineral caused by nutritional deficiencies [35].
- Osteomyelitis: bone infection caused by bacteria [36], [37].

- Cancer: Primary or metastatic causes progressive damage of bone tissue and its functions [38].

As mentioned above, those diseases affect multiple demographic groups according to their socioeconomic conditions. For example, in developed countries the average age of the population has considerably increased becoming in more cases of osteoporosis [2].

1.2 Bone tissue engineering

Tissue engineering combines the use of cells, engineering materials and physicochemical factors to improve or replace the biological functions of damaged tissues or organs. It uses the principles and methods of engineering, biology, and biochemistry to understand the structure and function of normal and pathological mammalian tissues and to develop biological substitutes in order to restore, maintain, or improve its function [39]. A wide area of interest for tissue engineering is the development of scaffolds that contribute to bone regeneration processes [40]. This development could follow some or all of the stages listed below [41]:

1. Scaffold fabrication.
2. Growth factor placement in the scaffold or damaged area.
3. Seeding of an osteoblast population into the scaffold in a static culture (petri dish).
4. Growth of premature tissue in a dynamic environment (spinner flask).
5. Growth of mature tissue in a physiologic environment (bioreactor).
6. Surgical transplantation of the scaffold.
7. Tissue-engineered transplant assimilation/remodeling.

The number and the way that previous stages are combined give complexity to the bone regeneration processes in tissue engineering. For scaffold fabrication, factors like size, mass, porosity, surface / volume ratio, form, surface shape, and chemistry of the element to be manufactured, and composition, structure, molecular weight and molecular orientation of the biomaterial must be considered. For stages that occur in *in-vitro* environments, variables like culture medium, pH, fluid flow, mechanical stimuli, temperature, origin of cells, number of cells, mobility of the cells, and cell activity affects

the growth of new tissue. Finally; defect sites, species, gender, age, inflammatory process, immunological process, mechanical stimuli, biochemical stimuli, enzymes and vascularization determine the bone regeneration processes in *in-vitro* environments [27].

1.3 Socioeconomic considerations

In 2007, it was calculated that the whole area of tissue engineering consists of 50 companies employing 3000 equivalent full time positions worldwide [42]. In 2010 the number of companies related to regenerative medicines increased significantly to 391, but only a small portion of these has a commercial product [43]. About 500000 bony grafts are performed each year in the United States [44] which are in correspondence with the assessment that between 5 and 10% of the 6 million fractures that occurred in North America were delayed or not consolidated [45].

Scaffolds, implants, biomaterials, cell based therapies and growth factors are usually considered as bone grafts substitutes in bone tissue engineering. Diverse analyses show different market sizes and their growth rates depending on what it is denominated as bone graft substitute: The global bone graft substitute market was valued at $1.9 billion in 2010 and it is forecast to reach $3.3 billion in 2017 [46]. Another source states that the market for orthopedic biomaterials in the United States was at almost $3.4 billion in 2012 [47]. Another study affirms that 1g of bone graft substitute costs approximately 100 USD and the volume of materials estimated was close to 10 tons per year in 2010 [6]. The European market for bone graft substitute products for spinal fusion was valued at USD 177 million in 2010 and its growth rate is projected close to 17% per year, reaching an estimated of $461 million in 2016. [48]. The global bone graft substitute market consists of eight different segments [47]: orthopedic bone graft substitute, growth factors, stem cells, cell therapies, orthopedic hyaluronic acid viscosupplementation, orthopedic tendon graft, orthopedic cartilage repair and spinal machined bone allograft. Growth factors represent the largest segment, close to 40% of the market. The segments related to synthetic materials represent only about 15% of the market, but their growth rate is the largest (close to 15% per year) [6].

The cost of replacing organs was estimated in 8% of the worldwide health costs in 2009 [7]. The high cost of tissue engineering is associated not only with research and development but also with the regulations governing human healthcare products [49]. Besides, some reasons for the size and growth rates of the bone tissue engineering markets are aging but also more active population, the increase of overweight issues in population, the increased interest of individuals in their own healthcare, the improvement of public health systems around the world and the development of orthopedic procedures for people of all ages [50].

1.4 Growth factors

Growth factors are substances, like cytokines or hormones, which act as biochemical signals capable to trigger cellular processes like growth, proliferation or differentiation, among others. The most considered growth factors in bone tissue engineering are listed below:

- *Bone morphogenetic proteins (BMPs):* BMPs are a family of cytokines that stimulates the proliferation of chondrocytes and osteoblasts and increases extracellular matrix production. BMPs induce the differentiation of mesenchymal stem cells into osteoblasts. BMPs allow not only skeletal tissue formation during embryogenesis, growth and adulthood, but also bone healing process. In newborns' skeletons, BMPs can be found in the collagen fibers of the bone matrix, and also in cells located in the periosteum, and the bone marrow. After a fracture, BMPs growth factors diffuse from bone matrix and activate osteoprogenitor cells which, in turn, produce more BMPs [51]. The BMP 2, BMP 4 and BMP 7 are the only growth factors that can singly provoke bone formation in *in-vitro* cultures and at *in-vivo* heterotopic sites. BMP1-3 increase the production of collagen type I and osteocalcin in *in-vitro* osteoblasts like cells, and improve the formation of mineralized bone nodules from bone marrow mesenchymal stem cells [52]. BMPs are the most representative bone graft substitute of growth factors segment due to their therapeutic possibilities [7], [42], [53]. Studies of combined application of BMPs and scaffolds showed that these growth factors promote novo bone tissue growth inside the porous structure [54]–[58].

- *Fibroblast growth factors (FGFs):* FGFs stimulate the proliferation of mesenchymal cells, osteoblasts and chondrocytes. FGFs enhance growth of different tissues due to their angiogenic properties [58], [59].
- *Insulin-like growth factors (IGFs):* IGFs promote the proliferation of osteoblasts and chondrocytes as well as induce matrix secretion from both cell types [58], [59]
- *Platelet-derived growth factors (PDGFs):* PDGFs increase the proliferation of chondrocytes and osteoblasts. However, depending on their concentration levels, they have also been implicated in bone resorption [58], [59].
- *Transforming growth factors-β (TGF-β):* TGFs-β cause the differentiation of mesenchymal cells into chondrocytes and may also induce chondrocyte and osteoblast proliferation [60]. Like PDGFs, they have been seen to increase bone resorption at certain concentrations playing a role in coupling bone formation and resorption activities [58], [59]
- *Parathyroid hormone (PTH):* PTH enhances the release of calcium from the bone extracellular matrix and induces osteoclast differentiation from stem cells. It plays a role in the inhibition of osteoblast functions [58], [59].

1.5 Scaffolds

Scaffolds are fundamental devices for the regeneration of lost or damaged tissues and they have become an important tool in tissue engineering [61]. Their functions, from the mechanical point of view, consist of bearing external loads and giving shape to the tissue that is regenerated on it [62]–[64]. From the biological point of view, those structures support the development of the extracellular matrix and cell colonization. In addition, scaffolds should allow transit of nutrient substances from the surrounding tissue or the culture media and waste disposal coming from the tissue being formed. Therefore scaffold stiffness, mechanical resistance, and permeability are important properties. An additional scaffolds' desirable feature may be a controlled degradation after they are implanted in order to get void space where new tissue can grow.

The mechanical properties and degradation of the scaffold depends on the material properties and the porosity geometry of its structure, meanwhile permeability depends on

its structure. The mechanical properties of the scaffold must be similar to the properties of the replaced bone tissue in order to prevent stress shielding. Finally, the degradation rate must be as close as possible to the tissue growth rate to maintain stable properties in the tissue-scaffold compound during the regeneration process.

1.5.1 Design considerations

A bioactive scaffold reacts in a controlled manner with its environment in order to stimulate specific biological responses where it is placed. The development of scaffolds to promote cellular growth inside them has been one of the fundamental goals of bone tissue engineering [41], [65], [66]. The biomechanical processes of bone regeneration are complex, so the requirements for scaffold design are diverse [20], [67]–[73]. Some of the most important design considerations are listed below:

- *Biofunctionality*: Ability of the scaffold to meet the functional requirements for which it was designed, restoring the functions of the replaced tissue.
- *Biocompatibility*: Ability to support a normal cellular activity, including molecular signaling systems, without eliciting or evoking local or systemic adverse effects to the host. Among the undesirable effects that must be eliminated, minimized, or controlled upon scaffold implantation in the body are: citotoxicity, genotoxicity, immunogenicity, mutagenicity, thrombogenicity and swelling. For example, inflammation should be avoided because it can decrease the regeneration rate and promote tissue rejection.
- *Bioresorbability or biodegradability*: Ability to degrade over time in *in-vitro* or *in-vivo* environments, preferably at a controlled resorption rate in order to create space for new tissue to grow. In other words, it is expected that, as long as cells proliferate, void space in the scaffold increases and degradation rate of the material should match growth rate due to the healing or regeneration process. It is related with biocompatibility because degradation products should be non-toxic, and must be able to get metabolized and eliminated from the body. For example, the degradation behavior of the scaffolds should vary based on applications such as 9 months or more for scaffolds in spinal fusion, or 3 to 6 months for scaffolds in craniomaxillofacial applications. [74]

- *Mechanical properties*: Mechanical properties such as elastic modulus, tensile strength, fracture toughness, fatigue, elongation percentage, etc. should be as close as possible to the replaced tissue (mechanical compatibility) in order to prevent bone loss, osteopenia or "stress shielding" effect associated with the use of bone grafts. They are related to bioresorbability because the variation in mechanical properties due to degradation process should be compatible with bone regeneration process. A scaffold must have enough mechanical strength to retain its structure in order to comply with its mechanical function after its implantation, in the case of hard, load-bearing tissues as bone. The large variation in mechanical properties as seen in Table 1-1 makes it difficult to design an ‘ideal bone scaffold’.
- *Pore size and porosity*: A three dimensional design affects the spatial distribution and location of cells, nutrients and oxygen, thus affecting the viability of the new formed tissue. Porous scaffolds facilitate the migration and proliferation of cells, providing an appropriate microenvironment for cell proliferation and differentiation and allowing the mass transfer of nutrients, oxygen and waste metabolic products within the structure. Scaffolds should have a large internal surface area due to overall porosity and pore size. The surface to volume ratio of porous scaffolds is affected by the pore size. A large surface area allows cell adhesion and proliferation, whereas a large pore volume is required to contain and later deliver enough cell population for healing or regeneration process. Mass transfer and cell migration will be inhibited if pores are not connected even if the overall porosity is high. Unfortunately, an increase in porosity causes a decrease of mechanical properties such as compressive strength, and increases the complexity for scaffold manufacturing. On the other hand, osseous tissue typically have been arranged on curved surfaces; therefore, to mimic this biomorphic pattern, pores are intended to have curved cross-sections [20].

Regard to bone scaffolds, there are some specific features like:

- *Osteoconductivity*: Ability to allow the bone cells to adhere, proliferate and form extracellular matrix on its surface and pores [74]. This property is related to the biodegradability because the scaffold material must be reabsorbed to make space

for the mature tissue that it initially helped to support. Besides, scaffolds act as a mold of the desired anatomical form.

- *Osteoinductivity*: Ability to induce new bone formation through biomolecular or mechanical stimuli, recruiting progenitor cells and allowing differentiation in a controlled phenotype or particular lineages [75].
- *Osteogenicity*: Ability to act as an osteoblasts or mesenchymal cells (capable to derive in an osteoblastic lineage) reservoir because these cells can form and mineralize the extracellular matrix of new osseous tissue.
- *Osteointegrity*: Ability to form strong bonds with surrounding osseous tissue allowing material continuity and proper transfer load.

Finally, additional functions for bone scaffolds could be:

- Act as carrier of drugs (i.e. antibiotics and/or anti-inflammatories), growth factors or cultured cells.
- Radiolucency: Ability to differentiate radiographically with respect to the tissue where it was implanted.
- Formability: Ability to be shaped by a manufacturing process in order to obtain the necessary internal and external geometry.
- Sterilizability: Ability to ride out and facilitate a process of microbial destruction after being manufactured and before being used.
- Stability on storage (shelf life): Ability to preserve their physical, chemical and dimensional properties within the estimated storage period between manufacture and its use.

The conflicting nature of the above desired characteristics was described by Karageorgiou and Kaplan [76] who reported that higher porosities induce greater bone ingrowth but lower mechanical stiffness and strength. Therefore, scaffold porosity must lie within a critical range small enough to maintain the mechanical integrity of the scaffold and large enough to provide optimal bioactivity [68].

1.5.2 Design scales

The design and fabrication of scaffolds for bone regeneration applications attempt to obtain and control architecture at different levels due to external form and internal structure to meet the clinical requirements specified in the previous section. The architecture has different properties and characteristics depending on the dimensions of a scaffold element. Three basic scales refer to different features and processes:

The macro–meso scale describes the geometry measured in millimeters. Among its features are:

- Scaffold external shape (appropriated to the site where it will be implanted)
- Mechanical Properties
- Density
- Porosity: As a percentage of volume of the scaffold is empty.

The microscale describes features in the order of micrometers as:

- Pore size
- Interconnectivity of pores and tortuosity
- Degradability

The features in nanometers include factors such as:

- Surface topology of the pores
- Surface Physical Chemistry

1.5.3 Porosity design

Pore size and porosity are important geometric properties in scaffolds for bone regeneration because they affect the phenotype and the amount of tissue that grows on the element. As mentioned before, interconnected pores are necessary for bone tissue regeneration because they allow migration and proliferation of osteoblasts and

mesenchymal cells besides vascularization. It is observed that even a biomaterial like hydroxyapatite must have a porous structure in order to promote bone growth *in-vivo* [77] or a high porosity to allow cell seeding *in-vitro* [78]. Scaffolds implanted *in-vivo* with pore sizes close to 100 μm allow chondrogenesis but scaffolds with pores close to 350 μm, or above promote osteogenesis [79]. Although intensive research has been developed in both experimental and computational modeling, there are not final conclusions about the optimal porosity and pore size of a scaffold for bone regeneration. For example, the porosity range is between 50 to 90% for scaffolds that are not subjected to mechanical loads [80] meanwhile the recommended size of the pores varies between 150 and 600 μm [81], from 400 to 1200 μm [82] and 350 μm, or above [76]. The variety of conclusions may be due to the complexity of the process of bone regeneration, which is multivariable and multiobjective [83]. Considering this, and the emergence of solid free form manufacturing methods to fabricate scaffolds [84] that allow to control geometry characteristics better than other conventional methods like salt leaching, there is an increasing interest in porosity design. Giannitelli et al. [72] showed an extensive review of design approaches used to create porous structures in the scaffolds noting that these geometries can be obtained in three ways: Periodic structures, non-periodic structures and optimization techniques. Periodic porous structures can be based on CAD systems for solid and surface modeling, such as constructive solid geometry (CSG) using primitives like cubes, cylinders and spheres to represent the pores [85]–[91] and boundary representation (B-Rep) supported on facets and vertices [92]. In the last years, there has been researches on the use of implicit surfaces like triply periodic minimal surfaces [93]–[98] and space-filling curves like Hilbert curves [99]. Meanwhile, non-periodic structures have been developed based on image of bone surfaces [100], trabecular bone portions [101], [102], foams [103], stochastic methods and Voronoi diagrams [104]. The disadvantage of periodic and non-periodic structures is the necessity of trial and error methods to determine if they are suitable for a particular purpose [105], [106]. In contrast, optimization methods [107] using finite element methods obtain porous structures considering different objectives as mechanical properties and permeability [64], [65], [108]–[110].

1.6 Biomaterials for bone tissue engineering

A number of definitions have been developed for the term ‘‘biomaterials’’. One definition is: “Material exploited in contact with living tissues, organisms, or microorganisms” [111]. Another definition is: ‘‘A biomaterial is a substance that has been engineered to take a form which, alone or as part of a complex system, is used to direct, by control of interactions with components of living systems, the course of any therapeutic or diagnostic procedure, in human or veterinary medicine’’ [112]. In general, biomaterials are intended to interface with biological systems to evaluate, treat, augment or replace any tissue, organ, or function of the body and are now used in a number of different applications throughout the body. The major difference of biomaterials from other classes of materials is their ability to remain in a biological environment without damaging the surroundings and without being damaged in that process.

Natural, ceramics, polymers and composites can be used as biomaterials. Natural materials can be the bone from the same individual, from individuals of the same species, or form different species. On the other hand, ceramic materials are based on calcium phosphates and bioglasses. They have good osteoinductive properties but low mechanical properties and manufacturing difficulties. Polymers such as those derived from polyglycolic acid (PGA) and polylactic acid (PLA) have easy formability, good mechanical properties and biodegradability according to their molecular weight but low osteoinductive capacity. For their part, ceramic-polymer composite materials allow to obtain a biodegradable material, with good mechanical strength, osteoinductive, osteoconductive, and conformability properties by combining the properties of each material family. Here we mention some of the most common biomaterials for bone tissue engineering:

1.6.1 Grafts

A biomaterial commonly used for bone regeneration is osseous tissue taken from the same individual (Autografts). Autografts are considered the "gold standards" because they are osteoinductive, osteoconductive, and osteogenic. This material is normally taken from a site that is not under mechanical load such as the iliac crest. Autografts contain cells and growth factors that support the process of bone regeneration and do not exhibit

risk of rejection and disease transmission [113]. Some drawbacks of autografts are the necessity of additional surgeries, possible infections, bone morbidity, pain, and limited availability. Considering the osseous tissue source, there are allografts (tissue from individuals of the same species) or xenografts (tissue from individuals of different species). Allografts presented benefits as ready availability and easy handling, but require treatments such as freeze drying, irradiation or acid wash, among other processes to prevent rejection by the receptor and remove any possible infections from the tissue before implantation; but, these procedures can affect tissue mechanical and biological properties. Xenografts that usually come from cows and coral [114] could be osteoinductive and osteoconductive and low cost with high availability but have the disadvantages of immune response and risk of transmission of animal diseases [115].

1.6.2 Ceramics

Ceramic materials are a group of inorganic oxides and salts used in bone tissue engineering because of their similarity to the mineral component of bone in the case of calcium phosphate or because their capacity of strength bonding to osseous tissues in the case of bioglasses [113]. Some ceramic materials used in bone regeneration are listed below:

Calcium phosphates: Calcium phosphates are a family of minerals composed of calcium ions (Ca^{2+}), orthophosphates (PO_4^{3-}), metaphosphates, or pyrophosphates ($P_2O_7^{4-}$). The most common calcium phosphates for tissue engineering are: Hydroxyapatite (HA), Calcium sulphate hemihydrate (CSH), Gypsum, calcium sulphate dehydrate (CSD), Calcium carbonate, Dicalcium phosphate (DCP), Octacalcium phosphate (OCP), β-tricalcium phosphate (β-TCP), Biphasic calcium phosphate (BCP) and β-calcium pyrophosphate (β-CPP) [6]. Commercially available calcium phosphates proceed of natural or synthetic sources and are processed in many physical forms like particles, blocks, cements and coatings on metal implants or ceramic-polymer composites.

The most commonly calcium phosphate for bone tissue regeneration is hydroxyapatite (HA) which is a crystalline calcium phosphate ($Ca_5(PO_4)_3(OH)$) present in bones. Depending on its source, it can be natural or synthetized. For example, it can be produced from calcium carbonate and monoammoniumphosphate at ambient pressure

[116] or from natural sources like cattle or coral [117]. Some HA presentations exhibit a very similar bone structure with osteoconductive characteristics allowing connective tissue wrappings to start the regeneration process.

Calcium phosphates are bioactive materials because of their ability to form bone apatite like material or carbonate hydroxyapatite on their surfaces. They have the ability to promote cellular function and expression, besides the capacity of form a strong bind between bone and biomaterial interface. In addition, calcium phosphates biomaterials processed in porous forms are capable to bind and collect growth factors and become osteoinductive biomaterials [118], [119]. Calcium phosphates are materials that allow osteoblasts adhesion and promote mesenchymal cells migration. Related to degradation, tricalcium phosphates are capable of tunable bioresorption rate [120]. Different calcium phosphates can be used simultaneously to improve the scaffold performance [121].

Calcium phosphates applications in bone regeneration include their use as a scaffold in periodontal treatment, healing of bone defects, fracture treatment, total joint replacement, orthopedics, craniomaxillofacial reconstruction, and spinal surgery. Moreover, calcium phosphates are widely applied as a coating material to provide strength to polymeric scaffolds or to enhance the bioactivity of metallic surfaces [117].

Bioglasses: Bioglasses are a family of bioactive glasses composed of molecules of SiO_2, Na_2O, CaO and P_2O_5 in variable proportions. There are several types of bioactive glasses: conventional silicates, such as Bioglass 45S5; phosphate-based glasses; and borate-based glasses. A hydroxycarbonate apatite (HCA) layer is formed on the surface of the glass, following initial glass dissolution. HCA is similar to bone hidroxyapatite and interacts with collagen to bind the bioglass with the host tissue. Osteoinductivity in bioglasses is related to the stimulus of dissolution products of these biomaterials on osteogenic cells; besides, the HCA layer provides a surface capable to enhance attachment and proliferation of those cells. As a calcium phosphate, the HCA layer adsorbs protein and growth factors promoting new bone formation. An advantage of bioglasses above calcium phosphates is their faster degradation rate [122].

Bioglasses are used in bone regeneration like periodontal pocket elimination, alveolar ridge augmentation, maxillofacial reconstruction, spinal surgery and

otorhinolaryngological reconstruction [123], [124]. They can be processed and manufactured to generate three-dimensional scaffolds with different porosities and surface characteristics. [113]

1.6.3 Polymers

In tissue engineering, biopolymers are synthetic organic materials which are biocompatible with humans. In bone tissue engineering, biopolymers must exhibit an important property: biodegradability. This feature is important in order to obtain a scaffold that can be naturally unmounted while osseous tissue grows. Poly(α-esters), like polyglycolide PGA, polylactides PLA or polycaprolactone PCA, or polyurethanes degraded by hydrolysis. Poly(amino-acids) and collagen degraded by enzymatic action. Considering its ease of obtention and wide medical use [125] erosion of PLA has been studied by multiple authors [62], [126], [127]–[129] considering water diffusion into bulk polymer. Polymers such as those derived from polyglycolic acid (PGA) and polylactic acid (PLA) have mechanical properties and biodegradability which may vary according to their molecular weight and easy formability but low osteoinductive capacity [41]. Considering the scope of this thesis, biopolymers are better detailed in section 3.1 Polymers at page 59 of this document.

1.6.4 Biocomposites

The literature review has shown in recent years a trend in the development of scaffolds made of ceramic-polymer composites [130]. This is because ceramics such as calcium phosphates have excellent osteoinductive properties but low degradability, low mechanical strength and difficulty in forming processes for controlling the physical and geometrical characteristics required from the scaffold. In turn, polymers such as PLA exhibit poor osteoinductivity but better mechanical properties and degradability rates and they can be molded using various manufacturing processes that allow better control of its geometric characteristics. The development of ceramic-polymer composites allows biodegradable materials with good mechanical and biological properties as seen in Table 1-2 and Table 1-3.

Table 1-2: Porous biocomposites used for bone tissue engineering. NA. Data not available. From: Chen et al. [130]

BIOCOMPOSITE		PERCENTAGE OF CERAMIC (WT.%)	POROSITY (%)	PORE SIZE (μm)	STRENGTH (MPa)	ELASTIC MODULUS (GPa)	ULTIMATE STRAIN (%)
Amorphous CaP	PLGA	28 to 75	75	>100	NA	65	NA
β-TCP	Chitosan-gelatin	10 to 70	NA	322 to 355	0.32 to 0.88	3.94 to 10.88	NA
HA	PLLA	50	85 to 96	100×300	0.39	10 to 14	NA
	PLGA	60 to 75	81 to 91	800 to 1800	0.07 to 0.22	2 to 7.5	NA
	PLGA	NA	30 to 40	110 to 150	NA	337 to 1459	NA
Bioglass®	PLG	75	43	89	0.42	51	NA
	PLLA	20 to 50	77 to 80	approximately 100 (macro); approximately 10 (micro)	1.5 to 3.9	137 to 260	1.1 to 13.7
	PLG	0.1 to 1	NA	50 to 300	NA	NA	NA
	PDLLA	5 to 29	94	approximately 100 (macro); 10 to 50 (micro)	0.07 to 0.08	0.65 to 1.2	7.21 to 13.3
Phosphate glass A/W	PLA-PDLLA	40	93 to 97	98 to 154	0.017 to 0.020	0.075 to 0.12	NA
	PDLLA	20 to 40	85.5 to 95.2				
Bioglass	PGS	90	>90	300 to 500	0.4 to 1.0	NA	NA
Human cancellous bone		70	60 to 90	300 to 400	0.4 to 4.0	100 to 500	1.65 to 2.11

Table 1-3: Properties of bone graft substitutes. Adapted from : Ma y Elisseeff [24] and Brown et al. [131].

PROPERTY	ALLOGRAFT	POLYMERS	CERAMICS	COMPOSITES	CELL BASED THERAPIES	GROWTH FACTORS
Biocompatibility	Yes	Yes	Yes	Yes	Yes	Yes
Osteoconductivity	Yes	Yes	Yes	Yes	No	No
Osteoinductivity	Yes	No	No	Yes	No	Yes
Osteogenicity	Yes	No	No	No	Yes	No
Osteointegrity	Yes	No	Yes	Yes	Yes	No
Mechanical Match	No	Yes	Yes	Yes	No	No

1.7 Scaffold fabrication techniques

Various manufacturing methods have been used to achieve certain properties at different scales. These methods are classified into conventional and additive manufacturing methods. Conventional methods are solvent casting/particulate leaching, phase inversion/particulate leaching, fiber meshing/bonding, melt molding, gas foaming, membrane lamination, hydrocarbon templating, freeze drying, emulsion freeze drying, solution casting and ceramic sintering. These methods use physicochemical phenomena to ensure internal structures with a variable pore size between 100 and 500 μm with porosities up to 90% [27]. They have the disadvantage that the internal structure consists of randomly arranged trabeculae and physical properties as permeability variation are difficult to control. Meanwhile, methods of additive manufacturing, also called rapid prototyping (RP) or free-form modeling (SFF), which can be used for scaffold fabrication are fused deposition modeling (FDM), three dimensional printing or plotting (3DP), selective laser sintering (SLS) and stereolitography (SLA). These methods achieve large scaffolds with oriented structures but fail to obtain high porosity with small pores. A list of specific materials, processing methods, and properties obtained are given in Table 1-4. An alternative to solid bone scaffolds are injectable bone cements [132], [133]. These are mainly used in the fixation of prostheses and filling bone cavities and kyphoplasty treatments [134].

1.8 Discussion

Bone tissue engineering is a complex and challenging area. From a social point of view, it can provide benefits to population around the world but it implies a high cost that not all health systems of countries, like Colombia, can maintain in a sustainable manner over time. Nevertheless, the global bone graft substitutes market is actually growing, mainly due to the population needs and the improvement of the health services. In this context, design and manufacture of biodegradable scaffolds is one of the mayor research and development interests in tissue engineering. This chapter gives a review about the scaffold design considerations and requirements, the biomaterials that can be selected for a biodegradable scaffold and their related manufacturing processes.

Table 1-4: Manufacturing techniques for polymer and ceramic-polymer composites. From: Meyer et al. [27]

FABRICATION METHOD	MATERIAL	POROSITY	ELASTIC MODULUS (GPa)	PERMEABILITY (m^4/Ns)
Porogen leaching and compression molding				
Particle leaching	PLGA	80–92%	0.1–1.88*	$2.1x10^{-9}$–$16.1x10^{-9}$*
Compression molding/ Particle leaching	PLLA	78–97%	0.5–13	–
Compression molding / Particle leaching	PLGA	87%	6.6–12.9	–
Foaming/Particle leaching	PLGA	95%	0.4–0.5	–
Fiber				
Electrospinning	PCL	85%	1–20	–
Electrospinning	PCL	–	7.1–33.2	–
Fiber	PGA	95%	–	$2.6\ x10^{-6}$–$4.7\ x10^{-6}$
Woven fiber	PGA	70–74%	0.14–0.2 300–500^	$0.4\ x10^{-15}$–$0.9\ x10^{-15}$
Additive manufacturing methods				
Fused deposition modeling	PCL	48–77%	4–77	–
Nozzle deposition	PLGA/ PLLA/ TCP	74–81%	17–23	–
Nozzle deposition	HA	41%	1,110–1,240	–
Nozzle deposition	PEOT/ PBT	29–91%	0.2–13.7	–
3D printing	PLLA	0%	187–601	–
Stereolitography	PCL	37–55%	54–65	–
Inverse prototyping	HA	40%	1	–
	Collagen I	–	0.1–1	–
	POC	30/50/70%	0.35–1.05	
	PCL—dry		–	$6.9\ x10^{-6}$–$40\ x10^{-6}$
	PCL—wet		–	$2.9\ x10^{-7}$–$15.4\ x10^{-7}$

During the scaffold design process there are many considerations to be made: biofunctionality, biocompatibility, biodegradability, mechanical properties, and porosity are among the most important ones. Designing a biodegradable scaffold is a complex process in three ways: First, there are contradictions between the design parameters which must be considered, for example, high porosity versus high mechanical stiffness. Second, the scaffold must be designed using patient-specific parameter values in order to satisfy its functional requirements, thus it is necessary to estimate individual porosity, pore size and mechanical properties of the affected tissue. Third, the scaffold has to be

designed as easy as possible to manufacture, therefore design for manufacturability concepts must be taken into account.

As shown, many biomaterials and their manufacturing processes were developed; but, limited work has been done in order to obtain scaffolds specific and complex clinical requirements. One of the future challenges in bone tissue engineering is to design and to manufacture biodegradable scaffolds with a homogeneous growth rate over their entire volume, using pore size gradients or specific distributions of embedded growth factors. This requires manufacturing processes with higher resolution and biofabrication capabilities.

2 Modeling scaffold structure using a reaction-diffusion system

Scaffolds, cells seeding and growth factors are the main strategies used in tissue engineering [61]. One area of tissue engineering concerns researches on alternatives for new bone formation and replacement of its function. Scaffolds have been developed to meet this requirement, allowing cell migration, bone tissue growth and transport of metabolic substances. Scaffolds are made from different biomaterials and manufactured using several techniques that, in some cases, do not allow full control over the size and orientation of the pores characterizing the scaffold as mentioned in the previous chapter. A novel hypothesis that a reaction–diffusion system can be used for designing the geometrical specifications of the bone matrix is thus presented here. The hypothesis was evaluated by making simulations in 2D and 3D reaction-diffusion models in conjunction with the biomaterial scaffold. The results showed the methodology's effectiveness in controlling features such as the percentage of porosity, size, orientation, and interconnectivity of pores in a matrix produced by the proposed hypothesis.

2.1 Introduction

One of the major objectives of bone tissue engineering is to achieve similar geometries than those of trabecular bone. Up to date, there exist several methodologies for scaffolds design based on regular and irregular structures [72]. Most constructive approaches are based on regular arrangements: an internal geometry filled with a periodic distribution of unit cells. Unit cells are constructed with computer aided design (CAD) tools using design primitives like cylinders, spheres, cones, blocks organized in rectangular or radial layouts [135]. The advantages of such regular porous structures consist of their easier modeling, physical simulation and manufacturing. Besides the unit cell approach, there are parameterized models using mathematical functions to generate implicit surfaces with

porosity gradients [136]. It should be noted that those methodologies can be complemented by optimization techniques to improve the mechanical strength or permeability [137]–[142]. Although, periodic or regular porous structures can be relatively sophisticated, they are still limited to represent the structures present in nature [72], [137]. On the other hand, irregular structures are obtained from fractal curves or clinical images. For example, space-filling curves, continuous fractal curves that covers domains like planes or tridimensional spaces can create irregular architectures that are not generally achieved in models made with unit cell approaches [143]. Besides, variable porous structures can be acquired directly from computed tomography bone images [144]–[146]. Finally, designed structures can be fabricated using additive manufacturing methods such as SLA, SLS, FDM, 3D Printing and many others [147].

Although most of the work of bone scaffold modeling is supported in regular porous structures, it is important to consider that some studies show that imposing the same shear stresses might not be adequate for bone scaffold regeneration. Regeneration and remodeling of osseous tissue is not only caused by a high value of stress or strain but also by differences or gradients of those signals in nearby sections of bone tissue [148], [149]. This raises the possibility that irregular structures may be better to stimulate tissue regeneration due to less uniform stress distributions than those observed in regular structures. Another possible explanation for the irregular structure visible in trabecular bone is that regular structures have a tendency to exhibit catastrophic failure opposite to irregular structures [150]. As a result, biomimetic design has been introduced and widely used as an alternative method for irregular porous structure modeling.

For the previous reasons, computer simulation in tissue engineering has increased during recent years due to the costs involved in the experimental testing of Scaffolds [151]; modeling techniques have thus been developed to describe scaffold’s internal geometry determining their behavior in certain physical-chemical conditions. One approach involves obtaining and reconstructing these materials’ structure using X-ray computed tomography [152]. There are also design techniques for ordered [70], [110] or random porous structures; Voronoi decomposition implemented using CAD systems [153], [154] and reaction–diffusion (RD) systems are random structure design techniques [155], [156].

Reaction-diffusion systems consist of one or more reactive substances where reactive (synthesis and degradation) and diffusive events (transport) create patterns that can be stable or unstable in time and/or space[157]. The reaction-diffusion systems studies began with Turing's theoretical work [158] and Belousov's discoveries as mentioned by Zaikin and Zhabotinsky [159]. Turing showed in his work about mathematical modeling of reaction-diffusion systems that diffusion generates instability under certain parameters; small perturbations in one substance concentration can cause a variable pattern in space. He postulated that reaction-diffusion systems may be one of the mechanisms causing the morphogenesis of living beings. The Reaction-diffusion system research has been developed from this initial work along theoretical and experimental lines such as nonlinear analysis of reaction-diffusion systems [155], [156] modeling patterns and structures of living beings [160], [161], simulating predators and prey populations [162], searching for evidence of reaction-diffusion systems as a morphogenetic process [163], physical and chemical process modeling [164], and to a lesser extent, manufacturing materials [157].

Murray and Meinhardt's studies may be highlighted among the works that implemented reaction-diffusion systems to study morphogenesis. Murray has shown that a reaction-diffusion system can generate different patterns depending on the form and domain size [165]. Meinhardt's book developed multiple morphogenesis reaction-diffusion systems describing patterns in both animals and plants [166]. Reaction-diffusion systems have been used in Garzón-Alvarado's work in the field of bone morphogenesis to explain endochondral ossification [167]. Tabor used them for elucidating the origin of trabecular bone structure [168], Tezuka for describing bone remodeling [169], Courtin modeled cancellous bone structure with them [170], and Chaturvedi modeled the skeletal pattern in a growing embryonic vertebrate limb [171]. It is worth noting that, except for Refs. [170] and [171], the aforementioned work deals with 2D models and tends to be more qualitative than quantitative in describing how changing reaction-diffusion system parameters influence the patterns thus generated.

Some authors have studied 3D reaction-diffusion systems by nonlinear analysis. Callahan has analyzed Lengyel–Epstein and Brusselator models for identifying the parameters creating lamellar, face-centered FCC, body-centered BCC, or prism patterns [172]. Leppanen has studied the morphology and stability of the patterns obtained by the Gray Scott model and suggested that they may be a neuronal growth system [155]. Shoji has

simulated FitzHugh–Nagumo systems, obtaining the structures described by Callahan as well as gyroid and perforated sheets [173]. Such work was focused on obtaining a qualitative description of patterns without assessing their geometric properties.

Maselko [174] and Grzybowski [157] have suggested using reaction-diffusion systems for manufacturing materials. There is some experimental evidence that biomaterials such as hydroxyapatite [175], [176] and agarose [177] can exhibit reaction-diffusion systems characteristics but no studies have yet been made into how porous structures can be obtained by using reaction-diffusion systems or how to quantitatively control some of their geometric characteristics.

Therefore, the purpose of this chapter is to develop a design methodology for bone regeneration scaffolds, which is inspired in the self-assembling behavior that occurs during the formation of mineralized collagen composites such as trabecular and cortical bone [178]. We used a reaction-diffusion system in order to synthesize 3D porous structures according to the patient's requirements of pore distribution, size, shape, and connection. Different pore sizes and orientations could be achieved varying reaction-diffusion system parameters; these features could provide different isotropic or anisotropic physical properties and could be useful in order to stimulate bone growth in a specific orientation. A finite element model, based on the Schnakenberg system, was thus constructed and the 3D porous structures obtained in domains with sizes and shapes comparable with commercial Scaffolds, were analyzed.

Reaction-diffusion based-designed Scaffolds can be useful in tissue engineering because they mimic the trabecular bone and could be a new approach to manufacturing Scaffolds. Reaction-diffusion systems could control the internal architecture of the Scaffolds in terms of pore size and orientation, and overall porosity. Thus, reaction-diffusion systems could obtain Scaffolds of greater dimensions than other manufacturing methods.

2.2 Materials and methods

Considering a reaction-diffusion system as a morphogenesis process, we supposed that a 3D porous scaffold structure could be obtained by using this model. We developed the hypothesis in this section.

2.2.1 Assumptions required for scaffold design using reaction-diffusion systems

According to the main hypothesis, the manufacturing of self-assembled Scaffolds requires a biomaterial with four fundamental features:

- The species comprising the reaction-diffusion system must allow Turing pattern formation (such patterns being stable in time and unstable in space). Examples of real chemical reactions generating spatial patterns can be found in Refs. [179] and [180].
- The species comprising the reaction-diffusion system and their environment must be biocompatible in two periods: when the reaction takes place and when the biomaterial is degraded. For example, an active reaction-diffusion system within an agarose matrix (a biomaterial gel used as scaffold material) is presented in Ref. [177].
- The biomaterial must retain the Turing pattern resulting from the reaction-diffusion system in order to obtain the porous structure by polymerization depending on the concentration of one of the reaction-diffusion system species. Similar examples of substances depending on the concentration of one reaction-diffusion system species can be seen in Ref. [172].
- The reaction-diffusion system parameters must be able to control the shape, connection, amount, and distribution of cavities or pores in the biomaterial. Numerical reaction-diffusion system simulations where patterns vary according to the parameters are presented in Refs. [181] and [182].

These assumptions meant that Scaffolds had to be manufactured with minimal mechanical intervention. Self-assembled Scaffolds can be tailored to satisfy patient's needs of specific pore size and structure, according to their clinical records. Thus, scaffold design must consider two geometric levels. First, the scaffold external architecture requires knowledge about the shape and volume of the bone defect to be repaired. The Scaffold size defines the manufacturing method if it is made out of the patient and then implanted. Second, the scaffold internal structure is defined by pore size, porosity, and mechanical characteristics of replaced bone, and cell growth needs. Those properties can be obtained using computerized tomography (CT), magnetic resonance (MRI), X-rays,

densitometry, and mechanical testing, among other techniques [152], [183]–[185]. Scaffold requirements can also be controlled and designed just by the reaction-diffusion system and the polymerization reaction variables.

The theory necessary to design a scaffold by meeting the above requirements started from this hypothesis. A hypothetical reaction-diffusion system capable of developing Turing patterns is shown, followed by the theory of copying material.

2.2.2 The external chemical reaction

A hypothetical Schnakenberg chemical reaction as described by Maini and Othmer [186] was first supposed, this being an autocatalytic reaction given by:

$$X \underset{K_1}{\overset{K_2}{\rightarrow}} A \qquad (2.1)$$

$$2X + Y \overset{K_3}{\rightarrow} 3X$$

$$B \overset{K_4}{\rightarrow} Y$$

By the law of mass action, the reaction rate is directly proportional to the product of active concentrations of the reactants; then, the reaction kinetics is given by:

$$\frac{d[X]}{dt} = K_1[A] - K_2[X] + K_3[X]^2[Y] \qquad (2.2)$$

$$\frac{d[Y]}{dt} = K_4[B] - K_3[X]^2[Y]$$

Where K_1, K_2, K_3 and K_4 are positive constants. Assuming that *A* and *K* are constants, the previous system of equations only rely on *X* and *Y* variables. Note that *X* is created in the presence of *Y* and *Y* is destroyed in the presence of *X*. This hypothetical equation has been widely used in numerical experiments [187], explanations of morphogenesis, and other biological applications [177].

The equation's dimensionless process and behavior analysis can be seen in Appendices A and B. The dimensionless equation is derived from the kinetic equation, including a

diffusive term that considers the spatial movement of each molecule, written as a reaction-diffusion system given by:

$$\frac{\partial u}{\partial t} - \nabla^2 u = \gamma \underbrace{(a - u + u^2 v)}_{f(u,v)} \qquad (2.3)$$
$$\frac{\partial v}{\partial t} - d\nabla^2 v = \gamma \underbrace{(b - u^2 v)}_{g(u,v)}$$

Where *a*, *b, u* and *v* represent the reactants *A, B, X* e *Y* at a dimensionless level, γ is a dimensionless constant and *d* is dimensionless diffusion constant (see Appendix A for details). Furthermore, terms *f* and *g* represent the reactive term of the equation. This equation has space instabilities converging in time if it is verified that equation parameters are in a Turing Space (see Appendix B).

2.2.3 Polymerization reaction

Suppose a biomaterial obtained by polymerization of one specie in the reaction-diffusion equation due to concentration level of it. In other words, once the reaction-diffusion system reaches stability, the biomaterial inherits the spatial pattern that occurs in the Turing instability generated by the Schnakenberg equations. To model pattern formation in the biomaterial, it has been assumed that polymerization follows a step-growth process like the used to produce some synthetic polymers as polyesters, polyamides, polyurethanes [188]. This is given by a step function activated when exceeding a threshold value of reaction-diffusion system molecules. Once the polymerization function of the material is activated the final shape of the scaffold is obtained. The equation is given by:

$$\frac{dM}{dt} = C \frac{[X]^n}{[X]^n + [S]^n} \frac{t^p}{t^p + T^p} \qquad (2.4)$$

Where *M* is the biomaterial concentration, *S* is the threshold concentration value *X* which starts the polymerization, *t* is the time from initiating the polymerization process, *T* is the threshold time value which initiates polymerization, *C* is a constant speed and *p* and *n* are

constants defining the slope of the threshold function. The dimensionless form is given by (see Appendix A):

$$\frac{dm_s}{dt} = c\frac{u^n}{u^n + s^n}\frac{{t_a}^p}{{t_a}^p + {T_a}^p} \tag{2.5}$$

Where m_s is the dimensionless concentration of the biomaterial, c and s are constants, u is the dimensionless concentration of X (see appendix A), t is the dimensionless time and T_a is the dimensionless time threshold which starts the polymerization process. Figure 2-1 and Figure 2-2 show the behavior of threshold functions.

Figure 2-1: Example of threshold polymerization function. For s = 1.0

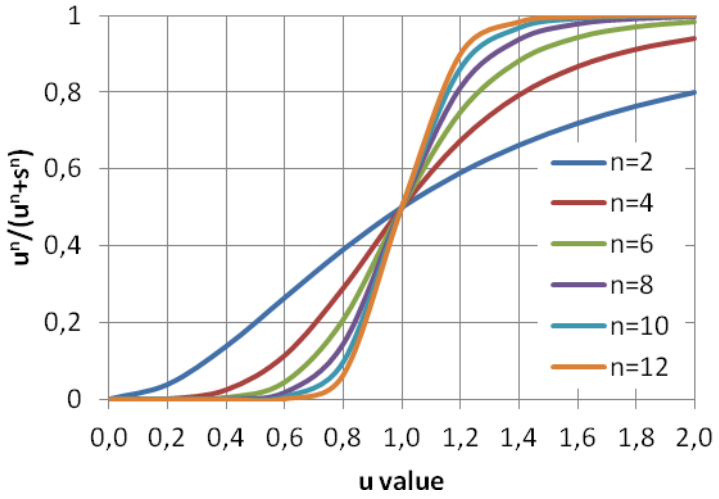

Figure 2-2: Examples of threshold polymerization function over time. For T_a = 1.0

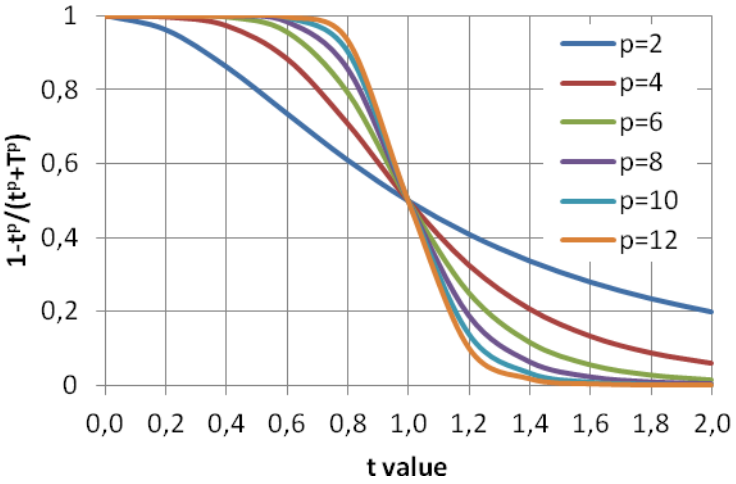

2.2.4 Analysis of wave number in the reaction-diffusion system

Chemical reaction, diffusion process, and polymerization function were proposed by manipulating the parameters using linear stability analysis (Appendix B) to design a scaffold. As shown in Appendix B *d, γ, a* and *b* are the dimensionless parameters of a reaction-diffusion system that allows controlling structures and forms of Turing patterns. Conversely, when designing a scaffold, it is necessary to know the required wave number to define the number of pores in one direction, besides *a* and *b*; after this, values of *d* and γ are obtained.

The wave number indicates the number of half sine waves in each of the directions x and y. Figure 2-3 provides an explanation for a wave number (4.2), which notes 4 half waves in *x* direction and 2 half waves in *y* direction. If each spot is considered as a pore, two pores in *x* direction and one in *y* direction are predicted.

Figure 2-3: Explanation of the correspondence of the wave number and Turing pattern for a (4.2) value. Note the relationship between wave number with shape and distribution of pores. Two pores in *x* direction and one in *y* direction are formed

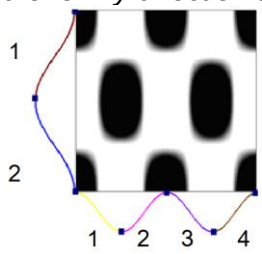

The points $K^2_{\min}$ and $K^2_{\max}$ ($\in \Re$) (see Appendix B) define an interval where the wave numbers or eigenvalues (Pores in the considered case) define the solution of the reaction-diffusion system. These points are given by:

$$K^2_{\min} = \frac{\gamma(df_u + g_v) - \sqrt[2]{(\gamma(df_u + g_v))^2 - 4d\gamma^2(f_u g_v - f_v g_u)}}{2d} \qquad (2.6)$$

$$K^2_{\max} = \frac{\gamma(df_u + g_v) + \sqrt[2]{(\gamma(df_u + g_v))^2 - 4d\gamma^2(f_u g_v - f_v g_u)}}{2d}$$

Where *d* y γ are dimensionless constants of the model; $f_u = 2uv - 1$, $f_v = u^2$, $g_u = -2uv$ and $g_v = -u^2$ are the derivatives of the reactive term. The interval given by $(K^2_{\min}, K^2_{\max})$

defines the wave number of the reaction-diffusion system solution in a Turing space as long as constraints given in (2.7) are complained:

$$\begin{aligned} &f_u g_v - f_v g_u > 0 \\ &f_u + g_v < 0 \\ &d f_u + g_v > 0 \\ &\left(d f_u + g_v\right)^2 > 4d\left(f_u g_v - f_v g_u\right) \end{aligned} \tag{2.7}$$

To clarify the instability behavior, it is necessary to define the domain geometry over which the solution takes place. In [34] is solved on a square, but information for various types of domains [36] can be provided. For example, considering a rectangle with length of each side in the direction of x and y are L_x and L_y respectively:

$$R = \left\{(x, y) \in \Re^2 \middle| 0 < x < L_x \wedge 0 < y < L_y \right\} \tag{2.8}$$

Then the wave numbers: *m* (half waves in *x*) and *n* (half waves in *y*), with *m*, *n* integers, will be in the range given by:

$$I = \left\{ (m,n) \in Z^2 \middle| K_{\min}^2 < \pi^2 \left(\frac{m^2}{L_x^2} + \frac{n^2}{L_y^2} \right) < K_{\max}^2 \right\} \tag{2.9}$$

Therefore, given the values of $(K_{\min}^2, K_{\max}^2)$ certain values of *m* y *n* that define the pores distribution in a domain can be found. In a square domain, as described in (8), the number of whole pores in *x* direction is given by $\frac{m}{2L_x}$, and $\frac{n}{2L_y}$ in *y* direction. An exhaustive review of the methodology to find the wave numbers can be found in Appendix B.

This chapter proposes the design process, for which, given $K_{\min}^2$, $K_{\max}^2$, *a* and *b* allows to find γ y *d*, which satisfies the requirements of the Turing space (2.7) and allow to obtain *m* y *n*. Thus, the nonlinear equations (2.6) that allow finding these parameters are solved using Newton-Raphson method [38], where the residuals are given by:

$$\gamma_{\min} = \left[\gamma\left(df_u + g_v\right) - 2dk_{\min}^2\right]^2 - \gamma^2\left(df_u + g_v\right)^2 + 4d\gamma^2\left(f_u g_v + f_v g_u\right) \quad (2.10)$$
$$\gamma_{\max} = \left[2dk_{\max}^2 - \gamma\left(df_u + g_v\right)\right]^2 - \gamma^2\left(df_u + g_v\right)^2 + 4d\gamma^2\left(f_u g_v + f_v g_u\right)$$

And the entries of the tangent matrix are given by:

$$\frac{d\gamma_{\min}}{dd} = 2\left[\gamma\left(df_u + g_v\right) - 2dk_{\min}^2\right]\left(\gamma f_u - 2k_{\min}^2\right) - 2\gamma^2\left(df_u + g_v\right)f_u + 4\gamma^2\left(f_u g_v + f_v g_u\right) \quad (2.11)$$
$$\frac{d\gamma_{\min}}{d\gamma} = 2\left[\gamma\left(df_u + g_v\right) - 2dk_{\min}^2\right]\left(df_u + g_v\right) - 4\gamma^2\left(df_u + g_v\right)^2 + 8d\gamma\left(f_u g_v + f_v g_u\right)$$
$$\frac{d\gamma_{\max}}{dd} = 2\left[2dk_{\min}^2 - \gamma\left(df_u + g_v\right)\right]\left(2dk_{\min}^2 - \gamma f_u\right) - 2\gamma^2\left(df_u + g_v\right)f_u + 4\gamma^2\left(f_u g_v + f_v g_u\right)$$
$$\frac{d\gamma_{\max}}{d\gamma} = 2\left[2dk_{\min}^2 - \gamma\left(df_u + g_v\right)\right]\left(-\left(df_u + g_v\right)\right) - 4\gamma\left(df_u + g_v\right)^2 + 8d\gamma\left(f_u g_v + f_v g_u\right)$$

Therefore, values of *d* and γ that meet the requirements of the wave number and modulate the pores distribution for a specific application can be found.

2.2.5 Hypothesis testing using numerical simulation

To test the hypothesis of scaffolds design using reaction-diffusion systems, the equation system given by (2) and (3) is solved using the finite element method. Newton-Raphson method is also used to solve the nonlinear problem that evolves over time. The time integration has been made using the trapezoidal rule. Then *u*, *v* and m_s must be obtained by proper interpolation functions as given in [39, 44-45]. The exhibition starts with the weak formulation of the problem and follows a procedure similar to that used in Ref. [181]. Let (2.3) and (2.5) rewritten as:

$$\frac{\partial u}{\partial t} - \nabla^2 u - \gamma(a - u + u^2 v) = 0 \quad (2.12)$$
$$\frac{\partial v}{\partial t} - d\nabla^2 v - \gamma(b - u^2 v) = 0$$
$$\frac{dm_s}{dt} - c\frac{u^n}{u^n + s^n}\frac{{t_a}^p}{{t_a}^p + {T_a}^p} = 0 \quad \text{in } \Omega$$

Multiplying (2.12) by a weighting function, integrating over the domain and using the Gauss theorem it can be proved that (2.12) has Newton-Raphson method residuals given by the next set of equations (2.13):

$$r_u = \int_\Omega \frac{\partial u}{\partial t} w_1 d\Omega + \int_\Omega \nabla u \nabla w_1 d\Omega - \int_\Omega \gamma a w_1 d\Omega + \int_\Omega \gamma u w_1 d\Omega - \int_\Omega \gamma u^2 v w_1 d\Omega - \int_\Gamma (\nabla u \bullet n) w_1 d\Gamma = 0 \quad (2.13)$$

$$r_v = \int_\Omega \frac{\partial v}{\partial t} w_2 d\Omega + \int_\Omega \nabla v \nabla w_2 d\Omega - \int_\Omega \gamma b w_2 d\Omega + + \int_\Omega \gamma u^2 v w_2 d\Omega - \int_\Gamma (\nabla v \bullet n) w_2 d\Gamma = 0$$

$$r_w = \int_\Omega \frac{\partial m_s}{\partial t} w_3 d\Omega - \int_\Omega c \frac{u^n}{u^n + s^n} \frac{{t_a}^p}{{t_a}^p + {T_a}^p} w_3 d\Omega$$

Where w_1, w_2 and w_3 are weighting functions and n is the normal vector directed out the domain over the boundary (see Figure 2-4). Considering that homogeneous Neumann boundary conditions had to be imposed, then the boundary terms of Eqs. (2.13) disappeared.

Figure 2-4: Description of Ω domain and Dirichlet Γ_u and Neumann Γ_q boundaries. In formulation of equation (2.13) the term $\int_\Gamma (\nabla u \bullet n) w_1 d\Gamma$ corresponds to Neumann boundary.

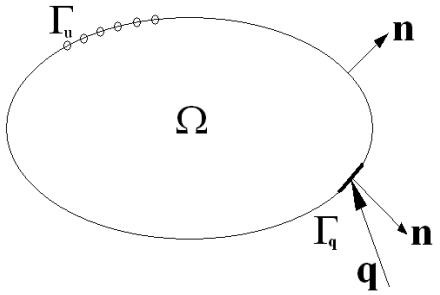

Variables were written in terms of nodal values using weighting functions such as given in Refs. [189] and [190] to obtain the discrete solution:

$$u^h = \mathbf{N_u}(x, y)\mathbf{U} \quad (2.14)$$

$$v^h = \mathbf{N_v}(x, y)\mathbf{V}$$

$${m_s}^h = \mathbf{N}_m(x, y)\mathbf{M}_s$$

$\mathbf{U}$, $\mathbf{V}$ y $\mathbf{M}_s$ are the values of *u, v* and m_s at nodal points and the superscript *h* indicates the variable discretization in finite elements. By substitution of (2.14) in (2.13) and

choosing weighting functions as the shape functions, Newton-Raphson method residual vectors are given by (2.15):

$$\begin{aligned}
\underline{r_u^h} &= \int_\Omega \mathbf{N}^T \frac{\partial u^h}{\partial t} d\Omega + \int_\Omega \nabla \mathbf{N}^T \nabla u^h d\Omega - \int_\Omega \mathbf{N}^T \gamma a d\Omega + \int_\Omega \mathbf{N}^T \gamma u^h d\Omega - \int_\Omega \mathbf{N}^T \gamma \left(u^h\right)^2 v^h d\Omega = 0 \\
\underline{r_v^h} &= \int_\Omega \mathbf{N}^T \frac{\partial v^h}{\partial t} d\Omega + \int_\Omega \nabla \mathbf{N}^T d \nabla v^h d\Omega - \int_\Omega \mathbf{N}^T \gamma b d\Omega + \int_\Omega \mathbf{N}^T \gamma \left(u^h\right)^2 v^h d\Omega = 0 \\
\underline{r_m^h} &= \int_\Omega \mathbf{N}^T \frac{\partial {m_s}^h}{\partial t} d\Omega - \int_\Omega \mathbf{N}^T c \frac{u^n}{u^n + s^n} \frac{{t_a}^p}{{t_a}^p + {T_a}^p} d\Omega = 0
\end{aligned} \tag{2.15}$$

Where $\underline{r_u^h}$ and $\underline{r_v^h}$ are the residual vectors calculated at the new time step. Meanwhile the second term $\underline{r_m^h}$ is calculated in the previous step.

Each of the positions (inputs) of the Jacobian matrix are given by (2.16):

$$\begin{aligned}
\frac{\partial \underline{r_u^h}}{\partial U} &= \frac{1}{\alpha \Delta t} \int_\Omega \mathbf{N}^T \mathbf{N} d\Omega + \int_\Omega \nabla \mathbf{N}^T \nabla \mathbf{N} d\Omega + \gamma \int_\Omega \mathbf{N}^T \mathbf{N} d\Omega - \gamma \int_\Omega \mathbf{N}^T \left(2u^h\right) v^h \mathbf{N} d\Omega = 0 \\
\frac{\partial \underline{r_u^h}}{\partial V} &= -\int_\Omega \mathbf{N}^T \gamma \left(u^h\right)^2 \mathbf{N} d\Omega \\
\frac{\partial \underline{r_v^h}}{\partial U} &= \gamma \int_\Omega \mathbf{N}^T \left(2u^h\right) v^h \mathbf{N} d\Omega \\
\frac{\partial \underline{r_v^h}}{\partial V} &= \frac{1}{\alpha \Delta t} \int_\Omega \mathbf{N}^T \mathbf{N} d\Omega + d \int_\Omega \nabla \mathbf{N}^T \nabla \mathbf{N} d\Omega + \int_\Omega \mathbf{N}^T \gamma \left(u^h\right)^2 \mathbf{N} d\Omega \\
\frac{\partial \underline{r_m^h}}{\partial m} &= \frac{1}{\alpha \Delta t} \int_\Omega \mathbf{N}^T \mathbf{N} d\Omega
\end{aligned} \tag{2.16}$$

Where α is a characteristic parameter of temporal integration method and $\nabla \mathbf{N} = \left[\left(\nabla N^1\right)^T ... \left(\nabla N^{nnod}\right)^T\right]^T$ is the row vector of spatial first derivatives of shape functions. In this case we used 4-node bilinear elements.

2.2.6 Design process for self-assembled scaffolds

The process for the design methodology proposed above can be seen in Figure 2-5, summarizing the steps for scaffold synthesis with a reaction-diffusion system. In brief, the

patterned structure could be generated by varying *a, b, γ*, and *d* equations parameters. In fact, the attractor state and the generated pattern are unique and independent of the initial conditions for no instantaneously growing domains. Considering this, reaction-diffusion equations were solved to prove the design hypothesis; biomaterial equation parameters were adjusted during such design process to obtain the required scaffold geometry.

Figure 2-5: Scaffold design process using a Reaction-Diffusion system

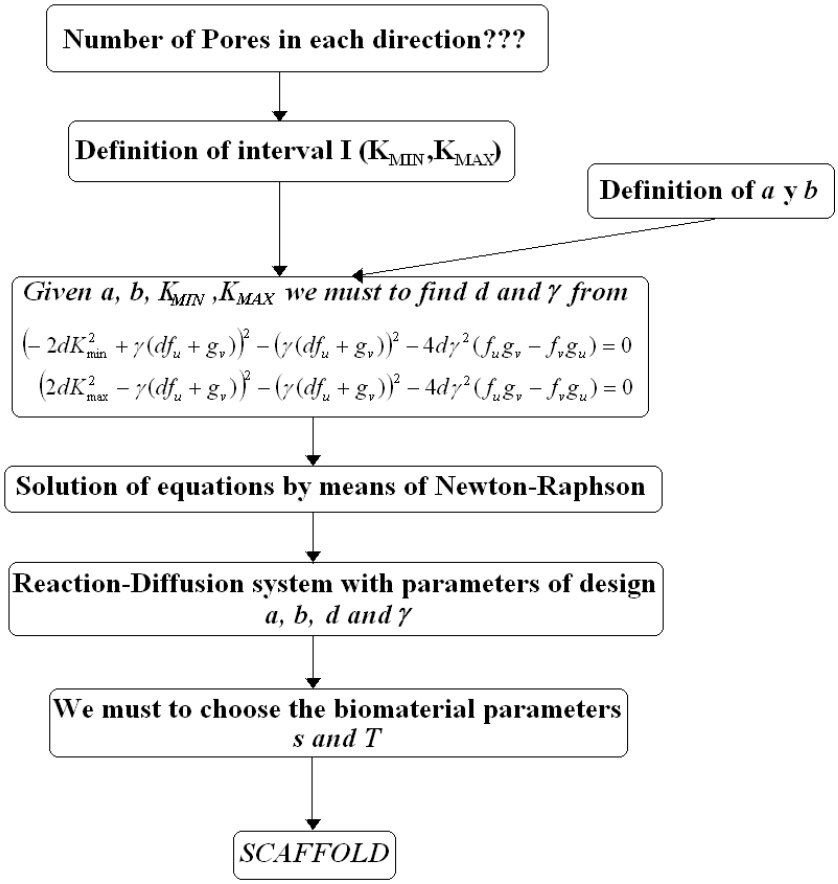

2.3 Application examples and results

This section presents numerical examples and results. 2D and 3D application examples were performed. The solution of reaction-diffusion system was found in 2D for a square domain, as well as the wave numbers predicted by linear stability theory. Initial tests were made for verifying the theoretical prediction. Several types of domains were then chosen on which reaction-diffusion equations and biomaterial equations were simulated. Likewise, initial 3D tests were developed on a unitary cube and other solid shapes.

The finite element method with Newton–Raphson method was implemented in FORTRAN for solving the resulting equation system and all examples were resolved as illustrated below on a 4,096-MB RAM Laptop with 800-MHz speed processor. In all cases, the dimensionless problem was solved with null initial conditions for biomaterial and random conditions around steady state (see Appendix B) for the reaction-diffusion system. The choice of random initial conditions around the steady state was similar to injecting two substances into a cavity, meaning that each concentration at the beginning of the reaction could not be accurately determined. Null flow on all geometries' boundaries was also considered.

Dimensionless parameters with running reaction-diffusion system simulations, shown below, were obtained by the process described in Appendix A. It was assumed that reference reactant length, time, and concentration values were magnitudes of unit value to simplify analysis and reading the results so there was correspondence between dimensional and dimensionless parameter numerical values. Distance in mm was particularly used as reference.

2.3.1 Initial numerical tests in 2D

The mesh used for the examples shown is the same in all cases, which has 2500 bilinear, 4-node elements each, for a total of 2601 nodes (see Figure 2-6). Moreover, the initial conditions are equal for all examples, with small random perturbations of 10% around the steady state. Initially the reaction-diffusion system was solved for square domains in order to have a framework to compare all subsequent numerical tests.

Figure 2-6: Mesh used in the numerical solution. The mesh has 2500 elements and 2601 nodes.

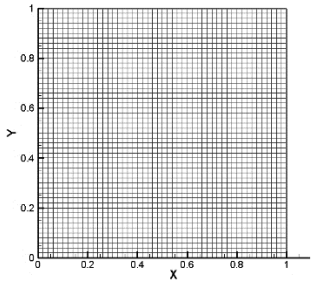

Figure 2-7 shows the results for the variable *u* of the Schnakenberg equation. Note the formation of dot patterns (cases b, d, e, g, h, i, k, l, n) and rows (a, c, f, j, m). Special attention deserves the case m) where $m^2 + n^2 = 25$. There are two possibilities of Turing pattern formation, this is, the dynamics of the system can choose among forming a wave number $(m = 4, n = 3)$, or, it could also form a pattern of type $(m = 5, n = 0)$. By the principle of minimum energy, in this case the pattern was formed $(m = 5, n = 0)$. All examples are in full agreement with those obtained in Turing pattern formation in reaction-diffusion systems literature [191].

Figure 2-7: Turing Patterns in steady state for different wave numbers. a) (1,0), b) (1,1), c) (2,0), d) (2,1), e) (2,2), f) (3,0), g) (3,1), h) (3,2), i) (3,3) j) (4,0), k) (4,1), l) (4,2), m) (5,0) and n) (4,4). For further reference see Table B.1 in appendix B. The black color indicates concentration values higher than 1.0. Black: high concentration, white: low concentration. Diagrams show *u* concentration in a reaction-diffusion system.

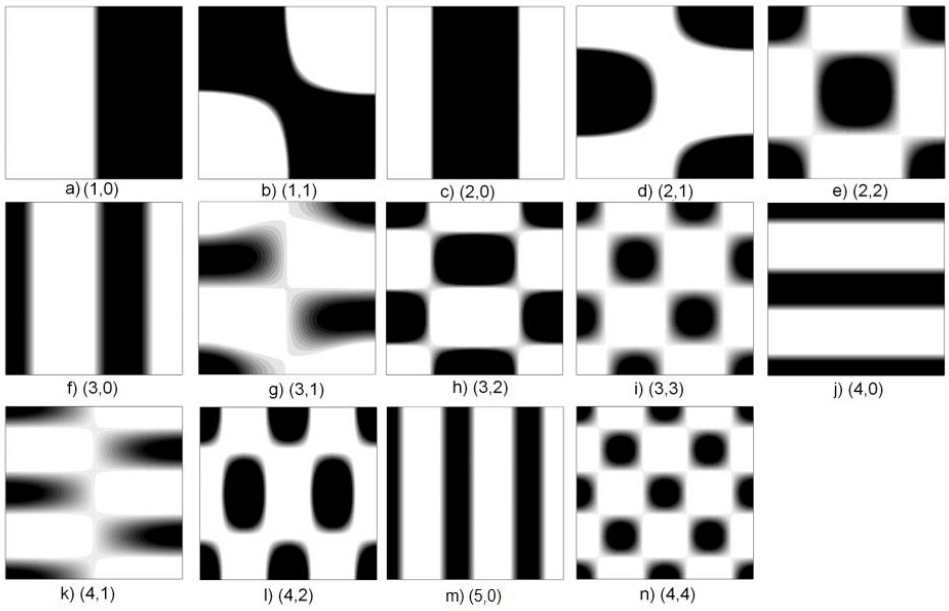

2.4 Simulations on 2D domains

2D tests were performed on figures of different sizes and forms based on the catalog of Kasios orthopedics products [192]. Figure 2-8 shows the mesh used to test the hypotheses stated.

Figure 2-8: Different geometries used for testing the hypothesis of the chapter. Figure a) Circle of Radio 4 mm with 5652 nodes and 5525 elements. b) Square of side 4 mm with 10,201 nodes and 10,000 elements. c) Wedge similar to that shown in Ref. [192], with 32,761 nodes and 32,400 elements.

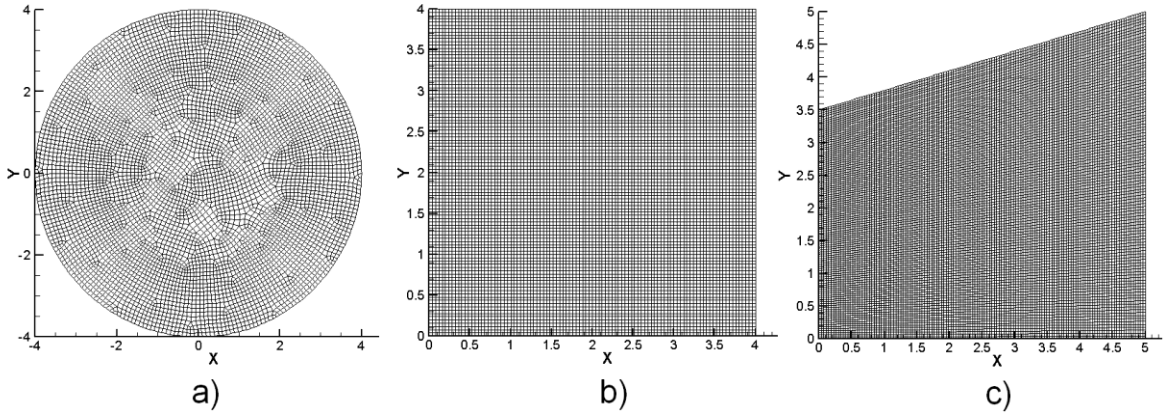

Figure 2-8 a) shows, in 2D, a circle with similar measures to those observed in commercial scaffolds [30]. Circle diameter is 8 mm. In the same way, a square scaffold was developed in Figure 2-8 b); besides, a wedge-shaped scaffold is showed in Figure 2-8 c.

Figure 2-9: a) Biomaterial distribution (black means there is biomaterial and white its absence in the scaffold). b) Results for the *u* variable of reaction-diffusion system, c) results for the variable *v*.

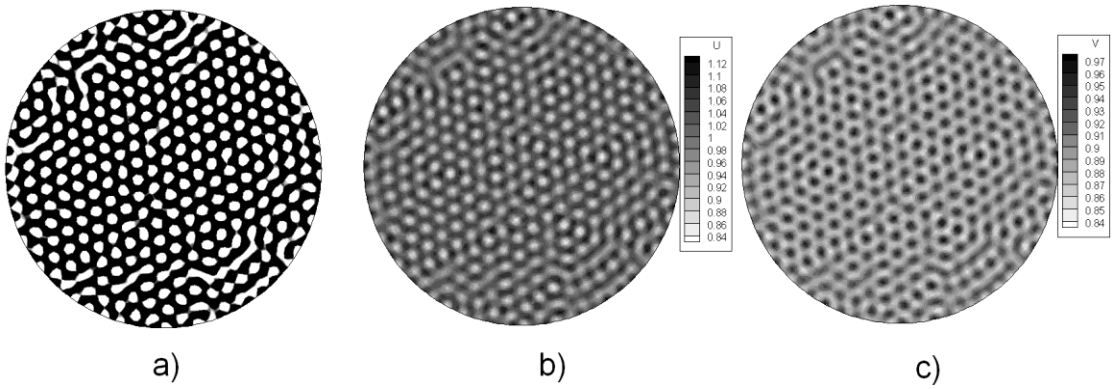

Figure 2-9 b) and c) shows the formation of circular spots patterns for the variables u and v. Note that circular spots are out of phase for each variable, i.e., where u is maximum, v is minimum and vice versa. The parameters used in the simulation are d = 8.6076, γ = 909.66, a = 0.1, b = 0.9, s = 0.95, T_a = 10.0. The threshold polymerization time T_a is the

time required for the reaction-diffusion system to reach steady state. In addition, other computational parameters are: Δt = 0.01 and used a total of 1000 steps. Plotting the concentration of the variable u pattern in Figure 2-11a), which provides the scaffold morphology, is obtained. In this case biomaterials polymerize in regions where the variable u has exceeded the threshold value of s = 0.95 and a polymerization time Ta = 10.0. A homogeneous distribution of holes, mostly circular, can be observed over the entire domain. As the scaffolds listed in the Kasios manufacturer catalog [192], average pore diameter is 350 μm and the distance between each pore is 500 μm. The resulting porosity is 65%.

Figure 2-10: a) Biomaterial distribution (black means there is biomaterial and white its absence in the scaffold). b) Results for the *u* variable of reaction-diffusion system, c) results for the variable *v*.

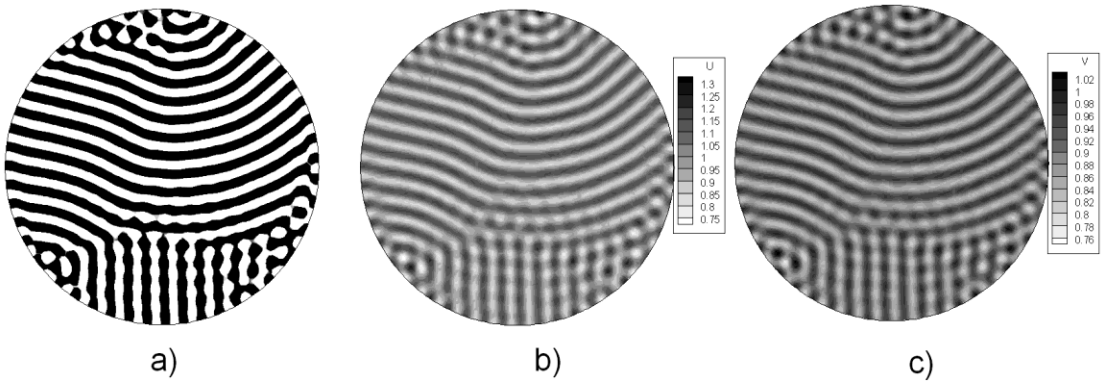

Change of reaction-diffusion system parameters provides a different structure as seen in Figure 2-10, different to Figure 2-9. In this case the parameters are d = 8.7176, γ = 625.35, a = 0.1, b = 0.9, s = 0.95, T_a = 10.0. It shows the formation of channels in the scaffold from Schnakenberg system patterns (see Figure 2-10 a). Note that this example shows intricate channels that may allow bone growth. The channels average width is 350 μm and the distance between channels is 500 μm. It should be noted that channels have a homogeneous structure throughout the scaffold which, however, has some isolated cylindrical pores in the top left and bottom right. The resulting porosity is 60%.

Figure 2-11: a) Biomaterial concentration (black means there is biomaterial and white its absence in the scaffold). b) Results for the *u* variable of reaction-diffusion system, c) results for the variable *v*.

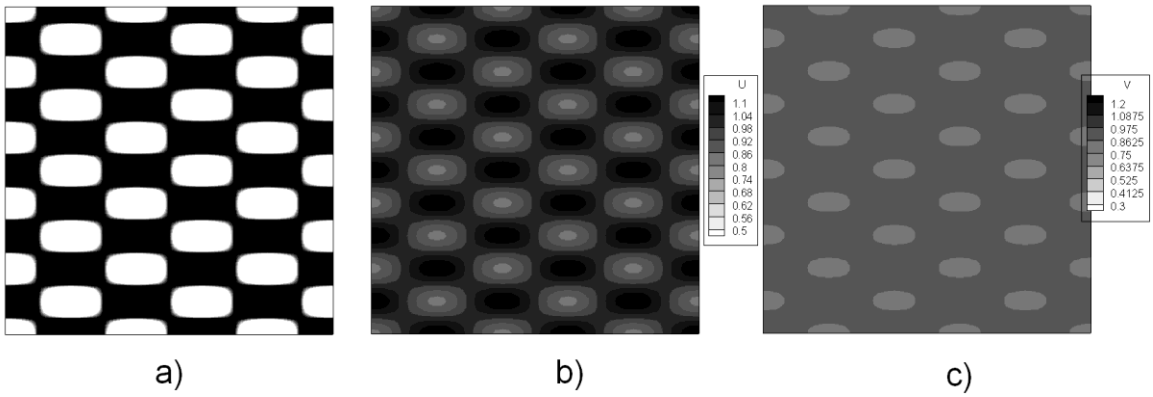

Changing the geometry to a square, Figure 2-12, and using the parameters d=8.6676, γ=230.82, a=0.1, b=0.9, s=0.95, T_a=15.0 different behavior of reaction-diffusion system is obtained. In this case, spots patterns on the Schnakenberg system allow polymerization of rectangular slightly elongated pores in the *x* direction as showed. The equivalent pore diameter is 420 μm; the distance between pores is 1600 μm in horizontal direction and 800 μm in vertical direction. Note, in this case, the special orientation of pores allows preferential growth of bone. The resulting porosity is 65%.

Figure 2-12: a) Biomaterial distribution (black means there is biomaterial and white its absence in the scaffold). b) Results for the *u* variable of reaction-diffusion system, c) results for the variable *v*.

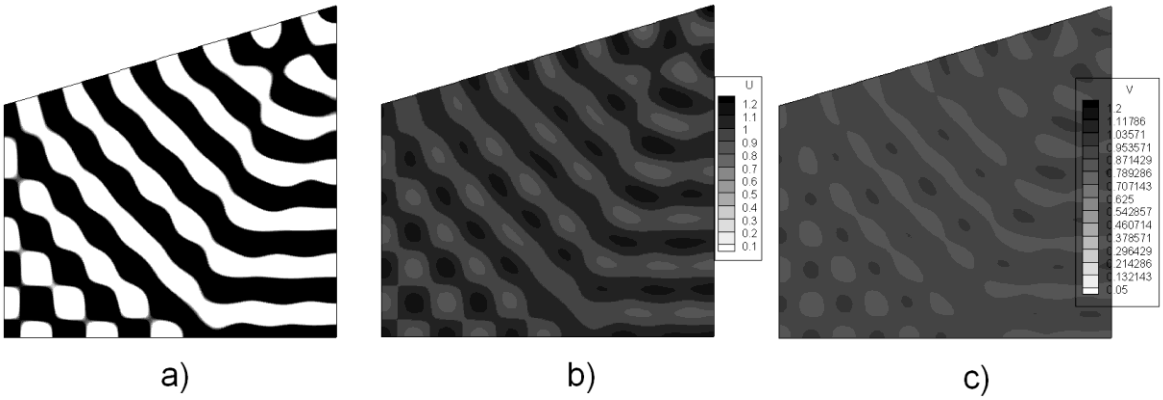

The case of wedge-shaped geometry, Figure 2-12, uses the parameters: d=8.6676, a=0.1, b=0.9, γ=230.82, s=0.95, T_a=15.0. The pattern forms a scaffold that has a mix of channels and pores (see Figure 2-12 a). Note that channels passing completely through the scaffold and the pores are located in the lower left and upper right corners. The width of each channel is 400 μm and the distance between channels is 800 μm. Resulting porosity is 55%.

2.5 Simulations on 3D domains

As in the two-dimensional case, in this case, numerical tests are performed on minimum basic geometries that conform a larger scaffold. In this case unitary cubes were used and different parameters were chosen in order to get porous structures with an orientation defined by the designer. The geometry for all numerical tests is similar, using unitary cubes with 17,576 nodes and 15,625 elements. Furthermore, all simulations have as parameters: Δt = 0.01, with 1000 steps. On the other hand, each of the structures is achieved by inheritance of Turing pattern, therefore, total time of stabilization Ta = 10.0 is used.

Simulation with wave number (2,2,2). Numerical tests were conducted on unitary cubes in order to observe the fundamental structure of the scaffolds. To define the structure shown in Figure 2-13, a Matlab program was used as described in appendix B. By the parameters, $a = 0.1$, $b = 0.9, K_{\min}^2 = 11.0$ and $K_{\max}^2 = 12.999$ results are obtained as $d = 8.6123$ and $\gamma = 346.3578$ and the wave number is determined as $(2,2,2)$. Results show the formation of two half waves in each of the *x* and *z* directions. The structure formed is similar to FCC crystal structure with centered pores on each side of the figure besides at the corners as seen in Figure 2-13 a), b) and c); meanwhile, BCC crystal structure is observed in Figure 2-13 e) and f). Varying polymerization threshold value *s*, different porosities are obtained; therefore, a design curve showing porosity as function of the polymerization threshold value *s* can be plotted as seen in Figure 2-13 a), b), c), d), e), f) and g). It is important to mention that figures 2-13 e) f), and g) are not possible as scaffold geometries, as they show solids not connected between them. Figures 2-13 h) and i) show the results for *u* and *v* variables of a reaction-diffusion system.

Simulation with wave number (4,2,2). Similarly, using the parameters $a = 0.1$, $b = 0.9, K_{\min}^2 = 23.5$ and $K_{\max}^2 = 24.999$ and using the Matlab program with Newton Raphson method, parameters $d = 8.5737$ and $\gamma = 700.4675$ are obtained and the wave number is $(4,2,2)$. Results (see Figure 2-15) show the formation of four half waves in *x* direction and two half waves in each of the directions *y* and *z*. The structure formed a hollow face-centered cube in two of its opposite surfaces and two holes in each of the four remaining sides. In addition, there are holes in each vertex of the faces containing the greatest amount of pores. Figures 2-15 h) and i) show the results for *u* and *v* variables of a reaction-diffusion system.

Besides, varying the threshold polymerization value *s,* different porosities are obtained; so, a design curve showing porosity as a function of the polymerization threshold value *s* can be plotted as seen in Figure 2-16.

Simulation for wave number (2,2,0). In the case of Figure 2-17, a wave number of (2,2,0) is considered so two half waves in front and back faces with no waves in the remaining sides are obtained. The structures have a central hole in the middle of faces and edges of the cube in *y* direction. Varying the polymerization threshold value *s,* different porosities are obtained; so, a design curve showing porosity as function of the polymerization threshold value *s* can be plotted as seen in Figure 2-18.

Figure 2-13: Results of different porosities depending on polymerization threshold value s (wave number (2,2,2)). a) s = 0.86, % porosity = 1.5, b) s = 0.87, % porosity = 5.3, c) s = 0.88,% porosity = 12, d) s = 0.89,% porosity = 23, e) s = 0.90,% porosity = 51, f) s = 0.91,% porosity = 77, g) s = 0.92,% porosity = 88, h) distribution for *u* variable of reaction-diffusion system (black) and i) for *v* variable (black)

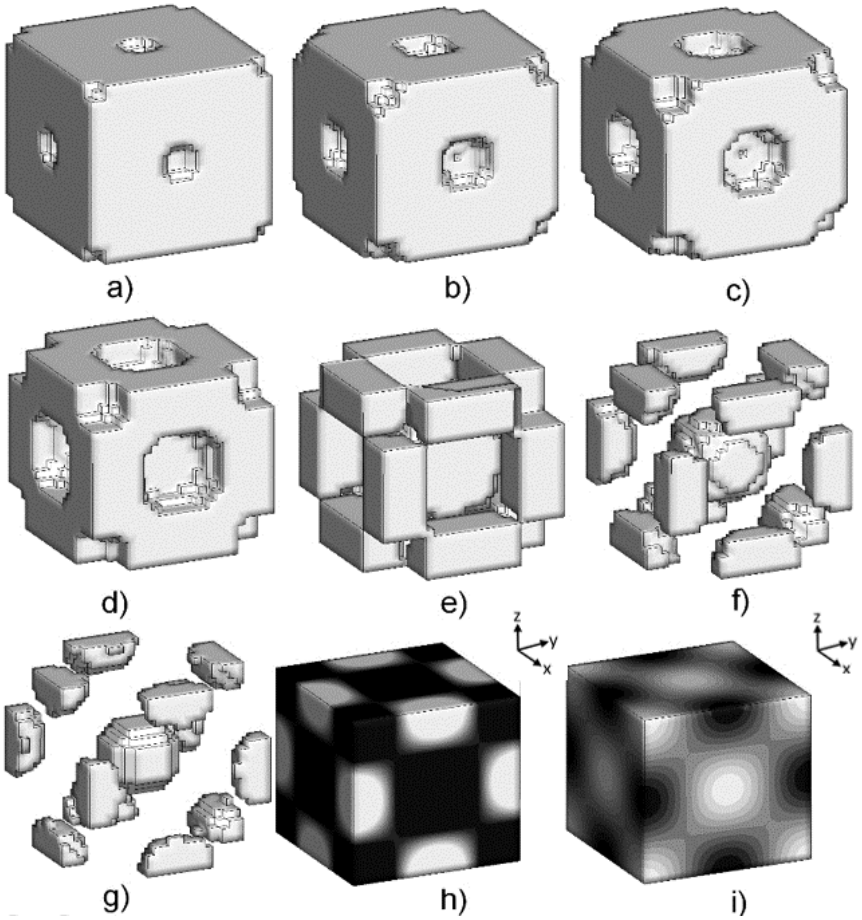

Figure 2-14: Percentage of porosity as a function of polymerization threshold value *s* for a wave number (2,2,2)

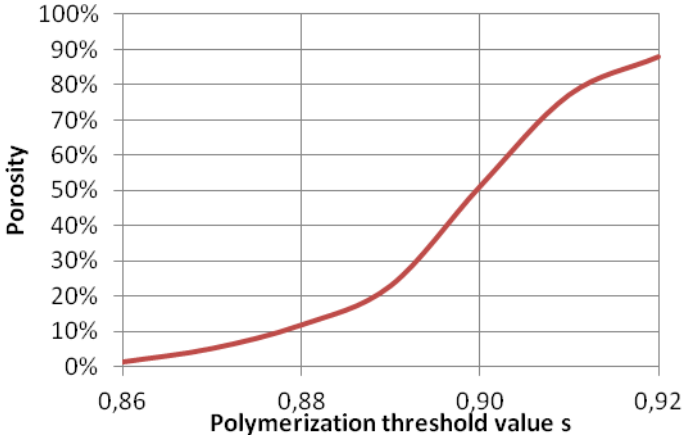

Figure 2-15: Results of different porosities depending on the threshold of polymerization (wave number (4,2,2)). a) s = 0.96, % porosity = 11.1, b) s = 0.97, porosity = 13.5%, c) s = 0.98, porosity = 19.5%, d) s = 0.99,% porosity = 29.4, e) s = 1.0, porosity = 55.4%, f) s = 1.01,% porosity = 81.4, g) s = 1.02,% porosity = 91.8, h) results for *u* variable of reaction-diffusion system and i) for *v* variable

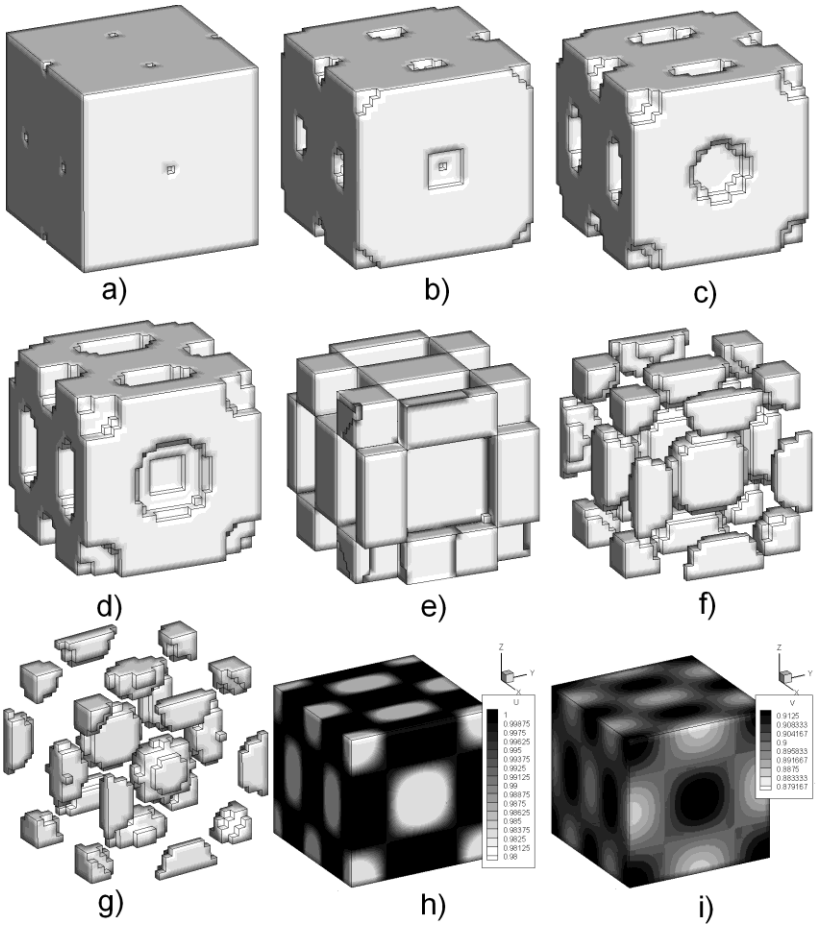

Figure 2-16: Percentage of porosity as a function of polymerization threshold value *s* for a wave number (4,2,2).

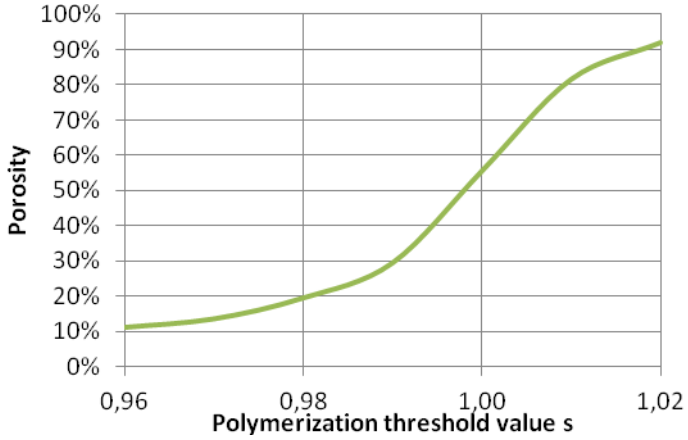

Figure 2-17: Results of different porosities depending on the threshold of polymerization (wave number (2,2,0)). a) s = 0.96,% porosity = 3, b) s = 0.97,% porosity = 11, c) s = 0.98,% porosity = 21, d) s = 0.99,% porosity = 34, e) s = 1.0, porosity = 55.2%, f) s = 1.01,% porosity = 71.1, g) s = 1.02, porosity = 81.1%, h) results for *u* variable of reaction-diffusion system and i) for *v* variable

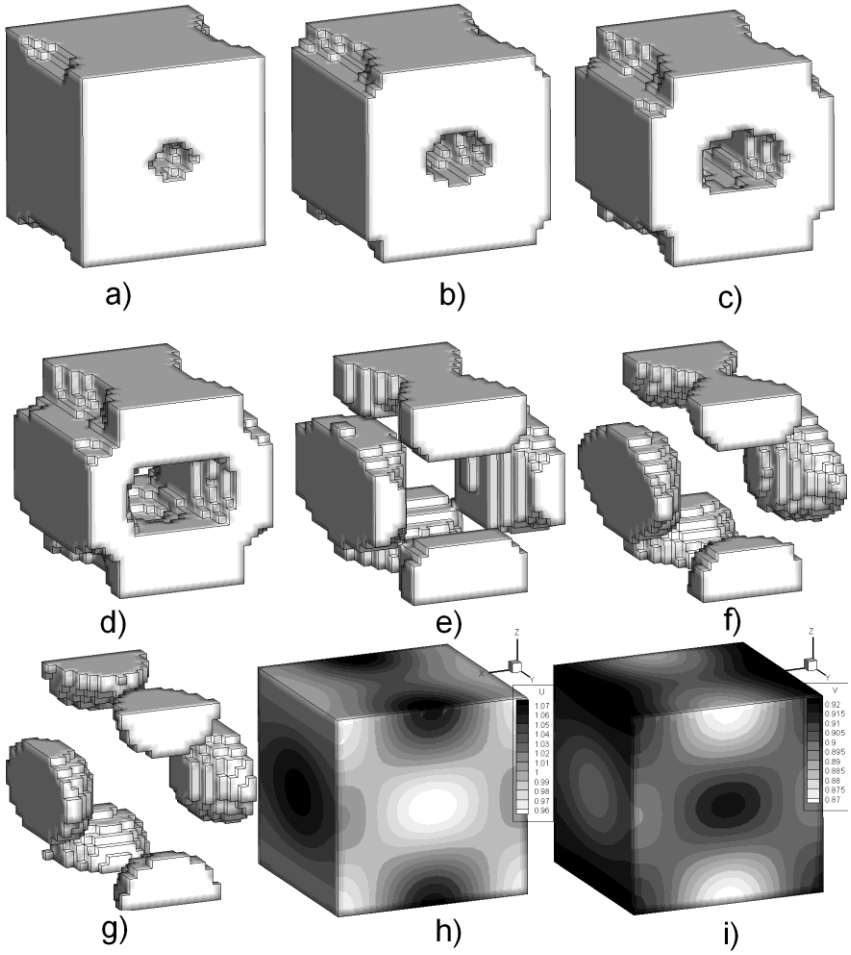

Figure 2-18: Percentage of porosity as a function of polymerization threshold value s for a wave number (2,2,0)

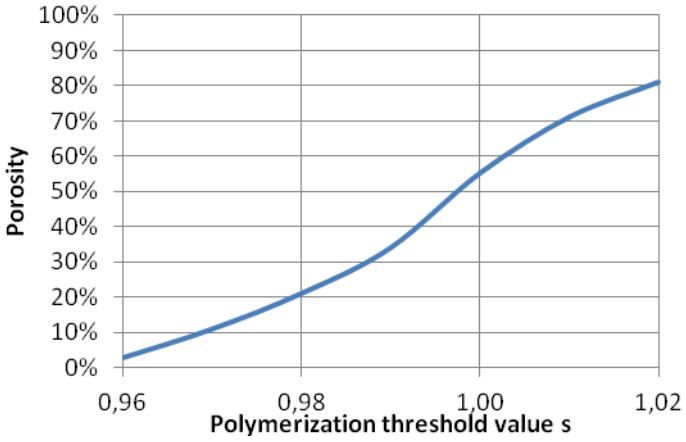

2.6 Simulation over domains similar to bone scaffolds for clinical applications

Figure 2-19 shows other shapes for the manufacture of a tridimensional scaffold. In the following simulations, different parameters of the reaction-diffusion system are used. For biomaterial, the value s = 0.9 and different curing times T_a are considered. In the first set of results, the first example 3D, polymerization time is variable therefore the obtained structures do not correspond to final the Turing patterns, this allows the formation of a transitional structure not corresponding to the final state of the reaction-diffusion system. The second simulation uses a set of parameters that conforms a final pattern compound by lamellae structures. The last example shows results for a set of parameters that give a complex structure in the scaffold. All the examples use the meshes and geometries described in Figure 2-19. Figure 2-19 a) shows a cube of 3 mm per side (in the simulation 46,656 nodes and 42,875 cubic elements were used). Figure 2-19 b) shows a cylinder with radius 1.5 mm and height of 3 mm (at the simulation 36,312 nodes and 33,462 elements were used). Finally, Figure 2-19 c) shows a wedge similar to those given in catalog [192] with approximate dimensions of a cube of 3 mm per side (in the simulation 29,791 nodes and 27000 elements were used)

Figure 2-19: Meshes for the simulation of scaffold construction over different geometries. a) Cube of 3 mm per side (in the simulation 46,656 nodes and 42,875 cubic elements were used). b) Cylinder with radius 1.5 mm and height of 3 mm (at the simulation 36,312 nodes and 33,462 elements were used). c) Wedge similar to those given in catalog [192] with approximate dimensions of a cube of 3 mm per side (in the simulation 29,791 nodes and 27000 elements were used)

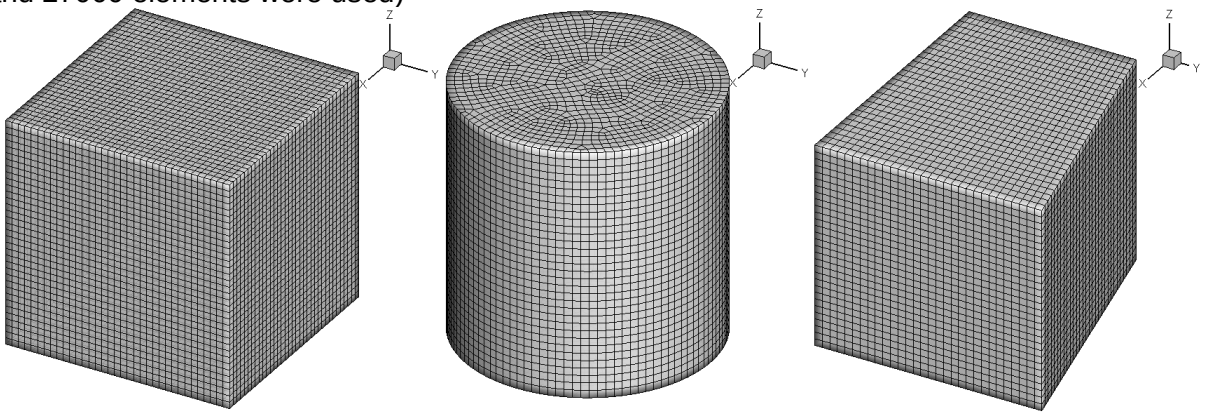

Simulation with parameter variation of polymerization time: Figure 2-20 shows the scaffold formation for a value of T_a (polymerization time) different to the time necessary to stabilize the Turing pattern. In all cases, the time T_a = 50.0 and model parameters are d = 8.6123, a = 0.1, γ = 346.3578, b = 0.9. Furthermore, Δt = 0.01 and the total steps are 5000 and s = 0.9. Note the formation of an intricate system of channels and pores with an average pore size of 400 μm. It should be noted that the final outcome of each scaffold is not the steady-state pattern of a reaction-diffusion system with Turing patterns. Therefore, the scaffold corresponds to an intermediate pattern in the path of a reaction-diffusion system to stabilize over time.

Figure 2-20: Simulation results of the scaffold construction on different geometries. a) Scaffold on a cube, b) values of the variable u for T_a = 50, c) Scaffold on a cylinder, d) values of the variable u for T_a = 50, e) scaffold on a wedge, f) values of the variable u for T_a = 50

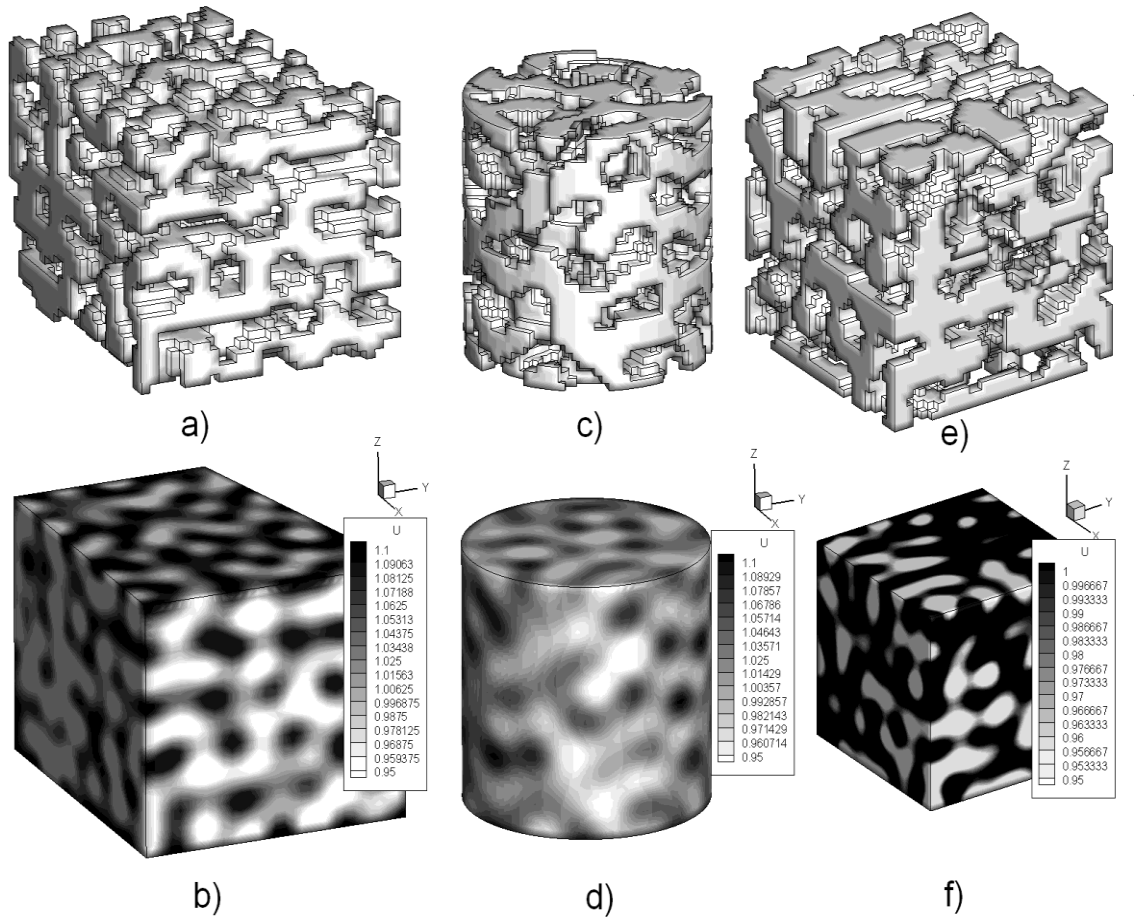

Simulation of a matrix developed from a stable Turing pattern. In the following example the parameters are d = 8.6123, a = 0.1, b = 0.9, γ = 346.3578. Furthermore, Δt = 0.01 and the total number of steps is 8000. In this case, Turing pattern development for the formation of the scaffold (steady-state) is considered. Therefore, T_a = 80.0 is the time value necessary to reach a steady-state Turing pattern. Figure 2-21 a) and b) shows two different views of the results for the scaffold formation on the geometry of a wedge. Note the shape of the plates that allow the anisotropic growth of bone. The distance between plates is 600 μm and width of the foil is about 400 μm. Figure 2-21 c) and d) show the formation of plates on a cylinder (with a width of foil of 400 μm and a distance between plates of 600 μm. Special attention requires Figure 2-21 e) and f) which are two different views of a scaffold on the geometry of a cube. In this case, the simulation is at time T_a = 70, so it does not show the final result of Turing pattern formation and therefore the final pattern but an interesting result of this simulation is the formation of continuous trabeculaes on one side of the array that can confer mechanical rigidity to the scaffold.

Figure 2-21: Simulation results of scaffold construction on different geometries. a) Scaffold on a wedge, a) and b) different views to the scaffold on a wedge geometry, c) and d) on a cylinder geometry and, e) and f) on a cube geometry. Note the formation of trabeculaes on one side. Simulation parameters are d = 8.6123, a = 0.1, b = 0.9, γ = 346.3578. Furthermore, Δt = 0.01 and the total number of steps is 8000

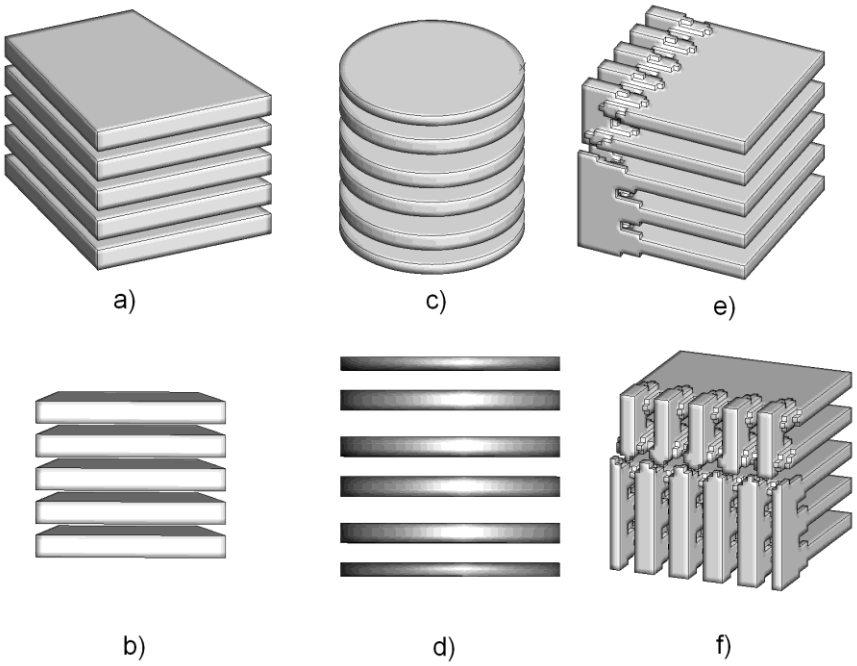

Examples for other scaffold figures developed from stable Turing pattern. A final example of the formation of a scaffold on the same geometric shapes used in previous examples but with different parameters was developed as Figure 2-22 shows. The parameters used are d = 8.5737, a = 0.1, b = 0.9 and γ = 700.4675. Furthermore, Δt = 0.01 and the total number of steps is 15000. In this case, as in the previous one, a Turing pattern development is recognized for the scaffold formation. Therefore, a time value T_a = is necessary to reach a steady-state temporal pattern. Figure 2-22 a) shows the result for a wedge. Note the formation of complex channels and holes throughout the structure. The average distance between channels is 300 μm. The porosity is 53%. Figure 2-22 b) shows the result for a cylinder. Note the formation of complex channels and holes throughout the structure; however, it appears that the channels are developed preferentially in the direction of the plane of the circle. The average distance between channels is 400 μm. The porosity is 54%. Figure 2-22 c) shows the scaffold formation on a cube-shaped geometry. Note the formation of well-distributed pores with a pore size of 300 μm. The resulting porosity is 55%.

Figure 2-22: Simulation results of scaffold construction on different geometries. a) Scaffold on a cube, b) Scaffold on a cylinder, c) Scaffold on a wedge

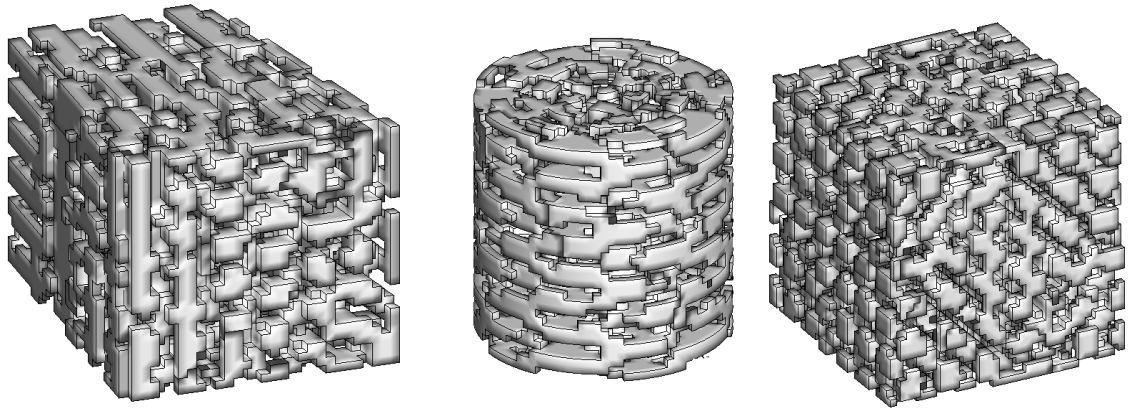

2.7 Discussion and conclusions

This chapter has reported the computational simulation of two and three dimension patterns obtained by varying Schnakenberg model parameters to establish a methodology for designing scaffold geometries for bone regeneration. Important features such as pore size and distribution and percentage porosity could be controlled depending on the value

for parameters K, a, b, d, γ, T_a and s in the considered model. The synthesized structures are similar to cancellous bone and could be self-assembled in situ.

The work began by studying a 2D reaction-diffusion system where Turing space analysis determined the possible ranges of values for parameters a, b, d, and γ in the reaction-diffusion system. All simulated cases were performed with Turing space parameters defined by a set of conditions defined in Eq. (7). It was found that wave number K determined pore spatial distribution frequency and that there could be more than one wave number K for the same parameters, so the system adopted the wave number having greater stability, according to the minimum energy principle. Figure 2-7 shows how different wave numbers gave patterns composed of circular, elliptical, or striped shapes in a 2D system, whereas, in three dimensions, they were widespread in a solid having spherical or ellipsoid pores and lamellar structures respectively.

Figure 2-13, 2-15 and 2-17 show how the pattern obtained in three dimensions could be changed according to wave numbers K. As shown in Appendix B, wave number value depended on Schnakenberg model values d and γ and domain size. Figures 2- 9 to 2-12 show how varying parameters d and γ determined pore or channel occurrence. It could be seen in 2D circular domain simulations that increased d and decreased γ values in pattern formation led to channels (d =8.7176 and γ = 625.35) instead of uniformly spaced pores (d =8.6076 and γ = 909.66). The same values (d =8.6076 and γ = 909.66) produced different patterns depending on domain geometry, forming symmetrical patterns of holes in the square in Figure 2-11 and a mixture of channels and holes in the wedge in Figure 2-12. This showed that domain geometry and size caused changes in the pattern generated by a reaction-diffusion system even if the parameters were the same.

3D simulation showed that d and γ values could modify pore order and/or distribution. Increased d and decreased γ values (d =8.6123 and γ = 346.36) led to the formation of patterns having lower wave number (2, 2, 0) compared to wave number (4, 2, 2) obtained with d =8.5737 and γ = 700.4675 parameters. Figure 2-21 shows how lamellar structures could be obtained using parameters d =8.6123 and γ = 346.36, causing wave number (2, 2, 0). Turing patterns similar to a spongy structure could be obtained as those appearing in Figure 2-20 and Figure 2-22 having parameters d =8.5737 and γ = 700.4675. Parameters mainly determined a structure's percentage of porosity. The percentage of

porosity increased as the value of s increased. It should be noted that the simulations reached temporary stability after time T_a with initial random spatial conditions.

The typical nonlinear behavior of reaction-diffusion systems could be observed with small parameter changes in all simulations and domains, causing significant changes in the morphology of the obtained pattern and the interaction between various reaction-diffusion system parameters. Although the structures obtained may have seemed disorderly or randomly organized, channel and trabecula widths were relatively uniform.

The porous or lamellar solid structures obtained in this study were consistent with other reaction-diffusion system studies like those of Kapral [193], Callahan [172] and Leppanen [194]. Figure 2 21 provides lamellar patterns, similar results also having been mentioned by Leppanen [194]. Figure 2 20 and Figure 2-22 show porous patterns having a similar shape to bone tissue and porous Scaffolds produced by particle leaching [24]. This technique's computational cost is low compared to others like that of Leppanen [194] since 500000–2000000 time steps are required in his 3D simulations to obtain stabilized patterns whilst stable structures were obtained here with 8000 time steps or less.

This work was aimed at obtaining porous structures from reaction-diffusion systems that could be used in Scaffolds for bone regeneration. A design methodology was thus based on analyzing DR system parameters for controlling the geometry of the developed pattern. It should be noted that this approach may be useful for modeling not only scaffold formation but also phenomena involving cell proliferation and tissue growth conditioned by growth factors or other chemical or physical signals. It has been shown that composite structures can be obtained by pores or channels and that the size and distance between them was relatively uniform and could be controlled. Both 2D and 3D patterns obtained in the simulations showed pore size and channel width consistent with the ideal 200–800 μm pore size mentioned in Ref. [195].

Some considerations and simplifications made in this work must be considered. The first concerns the experimental data supporting the model; however, it should be noted that nearly 30 years passed between Turing's work on reaction-diffusion systems as a mechanism for morphogenesis [196] and the first experimental evidence [163]. The second consideration is that the model assumed that at least one species led to

biomaterial polymerization. The third aspect concerns the simplification of domain size and reaction-diffusion system shape. Several authors, like Shoji [173], have reported the influence of domain size and shape on the generated pattern's form and stability. Available information regarding a commercial matrix for bone regeneration has been used in this study [192]. A fourth simplification considered Neumann conditions at domain boundaries. Actually, there may have been flux at the boundaries changing reaction-diffusion system patterns. Considering diffusion coefficients and reaction constants was also an oversimplification, as these are subject to various factors in the microenvironment where the reaction takes place.

Other systems, such as Brusselator RD, Gray-Scott, and Lengyel–Epstein, should also be studied to broaden the scope of this work [173]. The effect of domain and mesh element size should be analyzed regarding the obtained pattern's wavelengths. The numerical method's effect on pattern stability and shape should also be assessed. Subsequent work will consider Scaffolds in nonconventional geometries and impose Neumann boundary conditions to simulate biological substance flow rate along the boundaries.

Further research will be developed in order to manufacture reaction-diffusion structures using SFF techniques [197], [198] such as fused deposition material (FDM) [199]–[202], selective laser sintering (SLS),[92], [203]–[207] 3D printing (3DP) [208]–[211], among other processes. Scaffolds made by reaction-diffusion systems, such as other porous Scaffolds, could be used for other TE applications. They allow cell adhesion and proliferation of many cell types according to the organ or tissue that must be replaced. For example, Scaffolds for skin, cartilage, and liver replacement are mentioned in Ref. [39]. Again, geometrical properties such as porosity and related physical properties such as mechanical strength and permeability could be achieved by varying reaction-diffusion system parameters according to the specific application.

Despite the simplifications and the need for further studies, this work has been useful for several reasons. The model was useful in bone tissue engineering because it controlled geometric characteristics such as pore size and porosity percentage, these are design requirements necessary for enabling mobility and cell proliferation in addition to nutrient and waste transport inside the implant. The ability to vary implant pore size can also be used for providing preferential orientation of the implant structure conferring anisotropic

physical properties. From the numerical simulation viewpoint, it has helped in analyzing Turing patterns in three dimensions, a lacking work area, as mentioned by Shoji [173]. From a functional standpoint, this work compared to others such as Refs. [172] and [173], provided a methodology for controlling the geometry of the patterns so obtained, being important for scaffold's clinical applications. This work has provided a possible line of experimental research that can approach the resolution of complex problems in tissue engineering.

3 Modeling degradation of polymeric scaffolds

As the new bone growth, it is necessary scaffold degradation. Biodegradable materials for bone scaffolds applications could be ceramics, polymers or composites. Ceramics based on calcium phosphates show excellent osteoconductivity but low degradation rates [212]. Calcium phosphates degradation is due to multiple mechanisms like dissolution, precipitation, hydrolysis, and phase transformation [14]. Furthermore, polymers degradation occurs by hydrolysis and enzymatic action [213]. For their part, ceramic-polymer composite materials have good mechanical strength, osteoinductive, osteoconductive and conformability properties combining base materials properties [214]. In this chapter, a simulation of degradation process is performed assuming a hydrolysis mechanism.

3.1 Polymers

In tissue engineering, biopolymers are synthetic organic materials which are biocompatible with humans. They may be of natural or synthetic origin. Among the synthetic polymers most used for bone tissue regeneration are polylactic acid (PLA), polyglycolic acid (PGA), and copolymers of PLA-PGA (PLGA). Properties of some polymers and co-polymers biomaterials are listed in Table 3-1.

Poly (α-ester)s: Poly(α-ester)s are thermoplastic polymers with hydrolytically labile aliphatic ester bonds in their chains. Poly(α-ester)s can be developed from a variety of monomers using ring opening and condensation polymerization routes changing the monomeric units. Bioprocess methods can be used to develop some Poly(α-ester)s [215]. The Poly(α-ester)s are biodegradable, non-toxic and biocompatible. Among the class of Poly(α-ester)s, the most extensively investigated polymers are the poly(α-hydroxy acid)s,

which include poly(glycolic acid) and the stereoisomeric forms of poly(lactic acid). The most extensively studied monomers for aliphatic polyester synthesis for biomedical applications are lactide, glycolide and caprolactone [213]. Poly(α-ester)s mainly are degraded by hydrolysis bulk erosion. The polymeric matrices degrade over their all cross-section and have erosion kinetics that usually are non-linear with discontinuities [216].

Polyglycolide (PGA) is a highly crystalline polymer (45–55% crystallinity); therefore, exhibits a high tensile modulus with very high degradation rate due to organic solvents. The first biodegradable synthetic suture that was approved by the FDA in 1969 was based on polyglycolide [217]. Non-woven polyglycolide scaffolds have been widely used as matrices for tissue regeneration due to its excellent degradability, good initial mechanical properties, and cell viability. High mechanical properties of PGA are due to its high crystallinity. Self-reinforced forms of PGA show higher stiffness than other degradable polymeric systems used clinically and exhibit an elasticity modulus of approximately 12.5 GPa. Polyglycolide degrades by non-specific scissions of the ester chain. PGA loses its strength in 1–2 months when hydrolyzed and losses mass within 6–12 months. In the body, PGA degradation product is glycine which can be excreted in the urine or converted into carbon dioxide and water via the citric acid cycle [218]. Due to its good initial mechanical properties, polyglycolides have been investigated as bone internal fixation devices (Biofixs). However, the high rates of degradation and acidic degradation products limit the clinical applications of PGA. Therefore, copolymers containing PGA units are being developed to overcome those disadvantages.

Polylactide (PLA) is a chiral molecule and exists in two optically active forms: L-lactide and D-lactide. Their polymerization forms a semi-crystalline polymer and PLA behaves as crystalline or amorphous depending on these stereoisomers. The polymerization of racemic (D,L)-lactide and mesolactide results in the formation of amorphous polymers [219], [220]. The molar mass of the polymer as well as the degree of crystallinity have a significant influence on the mechanical properties [221].

Poly-L-lactide (PLLA) is a slow-degrading polymer compared to polyglycolide, has good tensile strength and a high Young’s modulus (4.8 GPa approx.); therefore, it is useful for load bearing applications, such as orthopedic fixation devices [213]. It has been reported that high molecular weight PLLA can take between 2 and 5.6 years for total resorption in

vivo [222]. On the other hand, semicrystalline PLA is preferred to the amorphous polymer when higher mechanical properties are desired. Semicrystalline PLA has an approximate tensile modulus of 3,5 GPa, tensile strength of 50MPa, flexural modulus of 5 GPa, flexural strength of 100 MPa, and an elongation at break of about 4% [223].

Poly(lactide-co-glycolide) (PLG): Both L- and DL-lactides have been used for co-polymerization with glycolide monomers in order to obtain different degradation rates. PLG degradation rates depend on a variety of parameters including the LA/GA ratio, molecular weight, and the shape and structure of the matrix. For example, 50/50% poly(DL-lactide-co-glycolide) degrades in approximately 1–2 months, 75/25% PLG in 4–5 months and 85/15% copolymers in 5–6 months. [224]. The popularity of these co-polymers can be attributed to the FDA approval for use in humans and its good processability [213].

Polycaprolactone (PCL): PCL is a semicrystalline polyester obtained by the ring opening polymerization of monomeric units of 'ε-caprolactone'. PCL presents hydrolytic degradation due to the presence of hydrolytically labile aliphatic ester bonds; however, the rate of degradation of homopolymer is rather slow (2–3 years) respect to polymers like PLA. PCL has low tensile strength (approximately 23MPa) and high elongation at breakage (>700%) [213]. It can be used in conjunction to other materials for load-bearing applications [225].

3.2 Biomaterial degradation

In the case of scaffolds made of biodegradable polymers, many resorption mechanisms are identified depending on the material type as seen in Table 3-2 [6]. In those models water molecules diffuse into the polymer and break the link into polymer molecules. These phenomena cause a molecular weight decrease besides a decrease of elasticity modulus. After a certain threshold of molecular weight the polymer is considered completely degraded [62], [216]. A more elaborate model is proposed by Chen [226] including autocatalysis. Han proposed a model that includes the effect of crystallization [227]. On the other hand, ceramics such as calcium phosphates and hydroxyapatite degrade by dissolution and osteoclasts effect, as modeled in Ref. [228].

Table 3-1: Mechanical properties of typical polymers and copolymers for tissue engineering. [218], [229], [230]

MATERIALS	COMPRESSIVE / TENSILE STRENGTH (MPA)	YOUNG'S MODULUS (GPA)	MELTING POINT (°C)	GLASS-TRANSITION TEMP (°C)	LOSS OF STRENGTH (MONTHS)	LOSS OF MASS (MONTHS)
PDLLA poly(L-lactide)	35–150		Amorphous	55–60	1–2	12 to 16
	29–35	1.9–2.4				
PLLA poly(L-lactide)	870–2300	10–16	173–178	60–65	6	?
	28–50	1.2–3.0				
	40–120					
PGA poly(glycolide)	340–920	7–14	225–230	35–40	1–2	6 to 12
PLGA	41.4–55.2	1.4–2.8		—		
PCL poly(e-caprolactone)		0.4	300–500	−65–−60		>24
85/15 DLPLG poly(DL-lactide-co-glycolide)		2.0	3–10	50–55		5 to 6
75/25 DLPLG poly(DL-lactide-co-glycolide)		2.0	3–10	50–55		4 to 5
65/35 DLPLG poly(DL-lactide-co-glycolide)		2.0	3–10	45–50		3 to 4
50/50 DLPLG poly(DL-lactide-co-glycolide)		2.0	3–10	45–50		1 to 2

3.3 Degradation model

Here, degradation is defined as a molecular change due to the division of the polymeric chains. This degradation can be homogeneous or heterogeneous when it occurs in certain areas of the polymer depending on the variation of its composition. In the case of a scaffold made of PLA, degradation is due to hydrolysis which causes a change in molecular weight and in turn a change in its mechanical properties. Water diffused into the polymer breaks the ester bonds leading to the formation of oligomers and monomers. In this model, the diffusion rate is assumed constant. Rapid diffusion leads to bulk erosion while surface erosion is caused by slow diffusion. Degradation produces a progressive decrease in the mechanical properties of the polymer and ultimately a scaffold loss mass.

Table 3-2: Resorption mechanisms for biomaterials for scaffolds used in bone regeneration. From: Bohner [6]

MATERIAL TYPE	MATERIAL	DEGRADATION MECHANISM
Ceramic	Bioglass	Generally: very limited degradation through partial dissolution
	Plaster of Paris (= calcium sulphate hemihydrate, CSH) Gypsum	Dissolution
	Dicalcium phosphate dehydrate (= calcium sulphate dihydrate, CSD)	Dissolution and/or conversion into an apatite
	Calcium carbonate	Dissolution or Cell-mediated depending on the mineral phase
	Dicalcium phosphate (DCP) Octacalcium phosphate (OCP) β-tricalcium phosphate (β-TCP) Biphasic calcium phosphate (BCP) Precipitated hydroxyapatite crystals β-calcium pyrophosphate (β-CPP; β-Ca2P2O7)	Cell-mediated
	Sintered hydroxyapatite	Practically no degradation
Metal	Magnesium (alloy)	Corrosion
	Iron (alloy)	Corrosion
	Tantalum, Titanium	Practically no degradation
Polymer	Polylactides, polyglycolides Polycaprolactone	Hydrolysis
	Cellulose Hyaluronan Fibrin Collagen Chitosan	Transport to lymph nodes Hyaluronidase Plasmin Collagenase Lysozyme

A numerical model that couples the molecular weight and the modulus of elasticity is used. It is assumed that the modulus of elasticity is proportional to polymer molecular weight. In turn, polymer molecular weight changes depending on the value of water concentration into the polymer.

To model the hydrolysis phenomenon of hydrolysis representative volume elements, (RVE) was chosen. The RVE can be considered as a unitary cell that can be arranged in a spatial matrix to obtain the desired structure. In turn, the RVE are divided into voxel or

hexahedral type elements to facilitate meshing. The boundary conditions do not consider the flow of water or other substances to or from the RVE.

Considering that the dominant mechanism for biodegradation of Polylactides is hydrolysis as mentioned in Table 3-2, in this study we adopt the degradation model proposed by Adachi et al [62]. A summary of the model is presented here.

Elasticity module E_s is proportional to the polymer's molecular weight:

$$E_s(W(t)) = E_{s0}\frac{W(t)}{W_0} \tag{3.1}$$

In (9) E_{s0} is the elasticity module at an initial molecular weight W_0.

Meanwhile, molecular weight is changing in time due to a hydrolysis process:

$$\dot{W}(c) = -\beta c \tag{3.2}$$

Where β is a biomaterial constant and *c* is water concentration varying between 0 and 1. For its part, c is depending on a diffusion equation:

$$\dot{c} = \alpha\nabla^2 c \tag{3.3}$$

Where α is the diffusion coefficient of water in biomaterial.

3.4 Results and discussion

This section presents numerical examples and results show the degradation of scaffold unit cells. Numerical tests were developed in a 3D cube, in order to obtain degradation evolution due to hydrolysis. The Finite element method with a Newton-Raphson scheme was implemented in a FORTRAN code to solve the resulting equation system. All the examples were resolved in a Laptop of 4096 MB RAM and 800 MHz speed processor

After the unit cells were obtained with the three different wave numbers as described in the previous chapter, numerical tests were conducted with the degradation model in order to examine their microstructural evolution due to hydrolysis. The considered material properties for the hypothetical scaffold were: initial elasticity modulus Es_0 = 20 GPa, Poisson's ratio v_s= 0.3, initial molecular weight W_0 = 70 000 g/mol, diffusion coefficient α = 4.0×10^{-4} mm^2/day, and degradation rate constant β = 4000/day. Those properties are similar to the ones exhibit by the Polylactic acid [62], [125]. Figure 3-1 a) and b) show the evolution of the water concentration and the elastic modulus, respectively, for the unit cell obtained with wave number (2,2,0). It takes 127 days for fully degradation. Figure 3-2 shows the degradation process for the unit cell obtained using the wave number (2,2,2). Figure 3-2 a) illustrates the evolution of the water concentration and Figure 3-2 b) illustrates the elastic modulus. The full degradation of the unit cells takes 118 days.

The degradation process for the (4,2,2) unit cell is illustrated in Figure 3-3. The evolution of the water concentration and the elastic modulus is shown in Figure 3-3 a) and b), respectively. The full degradation of the structure occurs after 91 days.

Figure 3-1: Degradation of the unit cell obtained with wave number (2,2,0) (a) water concentration (b) Elastic modulus.

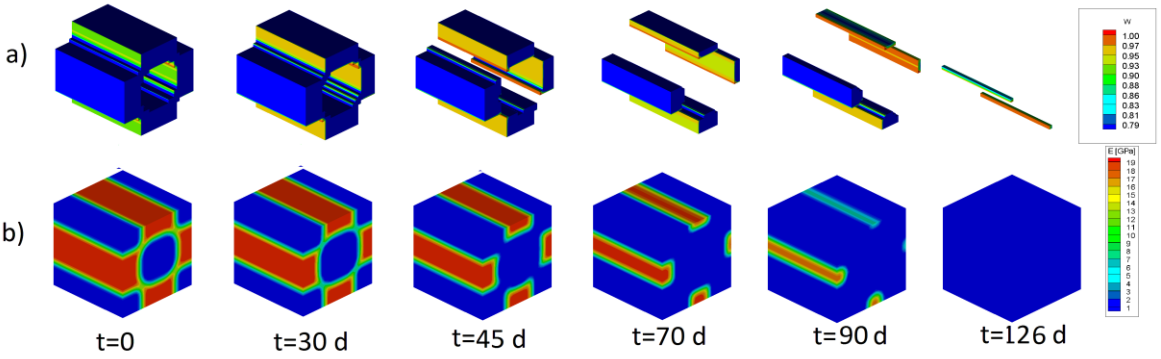

Figure 3-2: Degradation of the unit cell obtained with wave number (2,2,2) (a) water concentration (b) Elastic modulus

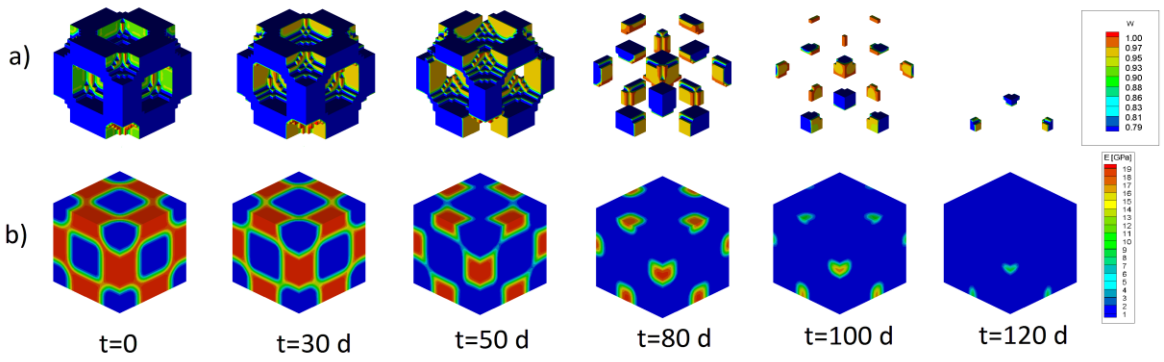

Figure 3-3: Degradation of the unit cell obtained with wave number (4,2,2) (a) water concentration (b) Elastic modulus.

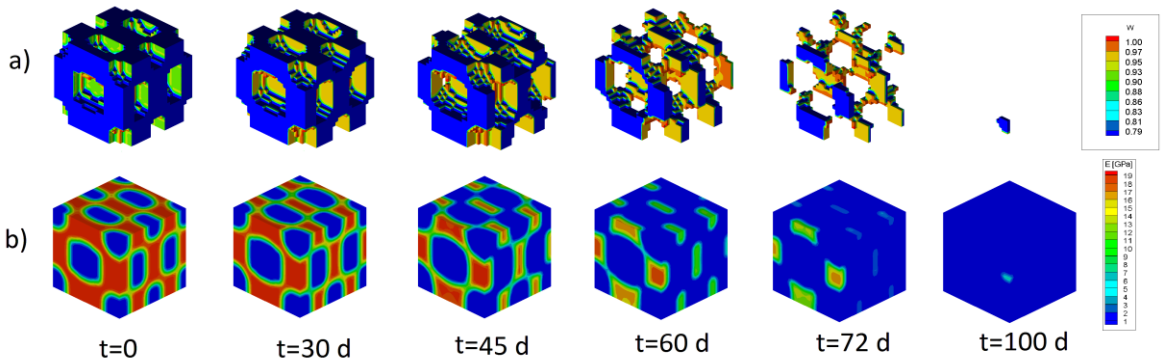

The Figure 3-4 illustrates the evolution of the normalized mass remaining over the degradation time. After 20 days, the degradation begins and it can be seen that the use of a high wave number decreases the time needed to achieve the full degradation.

Two coupled phenomena are appreciated in the obtained results: Degradation and erosion. Degradation as a change in the physicochemical properties of the polymer begins to manifest since the first days when there is a change of the elastic modulus of the polymer. Meanwhile, as it can be seen in Figure 3-4, the simulations show no apparent erosion for the first 20 days. From day 20 to day 50, approximately, similar

erosion rates are observed. Finally, from day 50 and subsequent, different degradation rates leads to higher mass decreasing in representative volume with wave number (4,2,2).

Figure 3-4: Normalized mass remaining over erosion time for the three unit cells

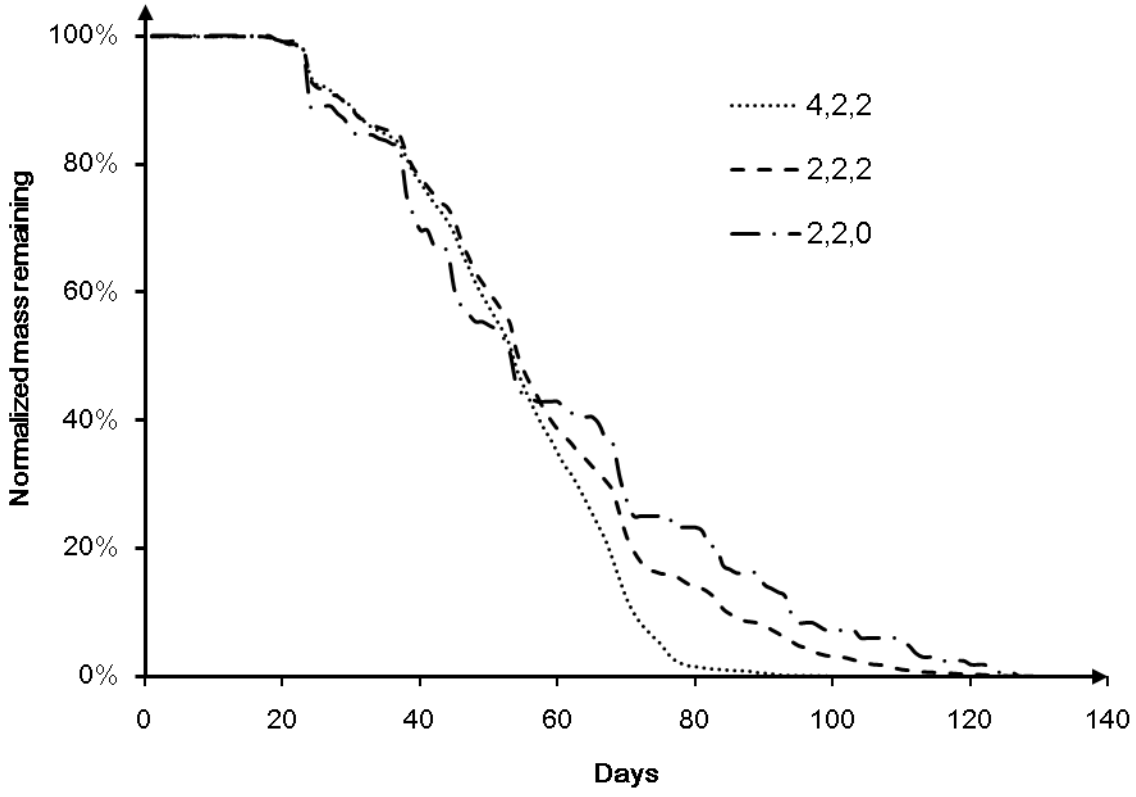

It is observed that the structure or geometry of the analyzed RVEs not only determine the initial stiffness of the scaffold but how it changes during the degradation process. The degradation rate of each RVE studied is affected by geometric parameters as the surface of the trabecula in contact with the aqueous medium and the width of the trabeculae which affects the distance that water must travel during the diffusion process into the polymer. It is noted that at lower wavenumbers, thicker trabecula is obtained and thus an increased degradation time. The object wavenumber (4,2,2) completely eroded at 80 days while the erosion time was close at 120 days for RVEs with wavenumbers (2,2,2) and (2,2,0).

3.5 Conclusions

The concept that a scaffold for tissue engineering must be removed as new tissue grows is widely accepted by the scientific community. However, the change of mechanical properties of stiffness and resistance can lead to scaffold premature failure. To avoid this problem, it is Important to know how the scaffold degradation and erosion occur but this is a challenging task. Computer simulation can be useful to analyze the complex phenomenon of degradation. Therefore, the aim of this chapter is to show the application of polymer in bone tissue engineering and to apply the hydrolysis model in the study of the degradation of hypothetical porous scaffolds.

Within various biopolymers, we decide to work on polylactic acid PLA considering this polymer is representative in the polyester family like PGA and PCL. PLA presents many advantages as it can be obtained from natural sources, biodegradability, and biocompatibility. Also, it is considered eco-friendly and with an easy formability as a thermoplastic polymer. The PLA in various isomeric, mixed or copolymerized forms can be used not only as a scaffold but besides to manufacture pins, plates and screws for bone fixation. The PLA in Its various forms is degraded generally by hydrolysis even that may be other mechanisms such as enzyme action. In the case of PLA, bulk erosion is the phenomenon that usually occurs. But, surface erosion should be preferred because its effects are easier to control. Then, it is desirable to use high molecular weight polymers to increase the degradation times.

The model used in this chapter is an elementary model for degradation due to hydrolysis. To obtain results closer to experimental observations it is necessary to consider more complex geometries and autocatalysis effects. During the hydrolysis process lactic acid released in the hydrolysis process accelerates the polymer degradation. Besides, acid degradation products may result in inflammatory processes altering the viability and motility of cells of regenerated tissue. In addition, experimental studies and computer models must be developed to establish the effects of polymer synthesis and scaffold manufacturing in the degradation and erosion parameters considered in the model.

4 Bone tissue formation under ideal conditions

In this chapter a review of the main theories of mechanobiology applied to bone regeneration is presented and subsequently bone growth on a polymeric implant is simulated. For this purpose, mechanobiology of bone tissue and computational models developed for simulating bone healing inside a scaffold are described. Finally, a simulation of an ideal process of bone regeneration over a biodegradable scaffold is developed.

4.1 Mechanobiology of bone tissue

Mechanobiology studies how mechanical stimuli influences the shape and structure of tissues of living beings; in particular, muscle, tendon, cartilage and bone tissues [231]. Mechanical and biochemical stimulus influence proliferation, differentiation and cell functions [232]. Therefore, mechanobiology would be useful to suggest clinical and tissue engineering strategies to control osseous tissue behavior.

Bone tissue is formed by a process called osteogenesis [233]. In this process, cells capable of tissue production interact with chemotactic factors to form bone. First, osteoblasts secrete substances to form osteoid tissue or immature bone, a non-mineral matrix compound of collagen and glycosaminoglycans [234]. Subsequently, the matrix mineralization occurs by deposition of hydroxyapatite [235], [236]. During this process, some osteoblasts become trapped in the newly formed bone and become osteocytes surrounded by osteons. Osteocytes maintain the extracellular matrix and it is hypothesized that they act as a network sensing mechanical stimuli that activates the bone remodeling units (BMU) formed by osteoblasts and osteoclasts.

Once the bone is formed, it can be remodeled or regenerated by mechanical and biochemical stimulus. Remodeling process takes place in old bone when tissue is replaced by new one in order to support changing loads or to replace bone with microdamage. It is estimated a turnover rate of 100% per year in the first year of life, 10% per year in late childhood [20] and nearest 5% per year in adult life [237]–[239]. Regeneration allows the creation of new tissue when an injury or lack of continuity occurs; for example, in case of fracture [240]–[242]. Both processes are carried out by BMUs [243]–[246], in which osteoclasts resorb deteriorated bone matrix and osteoblasts deposit new bone. Sometimes, those processes present disorders like in Paget's disease [247]. The processes of remodeling and regeneration are still under study because of the large number of physical and biological factors creating complexity in their interactions [21]. For example, it is hypothesized that osteocytes by piezoelectric phenomena respond to mechanical deformations or stresses and send signals to osteoblasts and osteoclasts so they engage and conform BMUs to perform the resorption or deposition of new bone [10].

Remodeling and regeneration requires actions at different scales. The mechanosensitive / mechanoresponsive process starts in nanoscale or molecular level activating genes and signals in cells [149], [248], it continues with a mechanotransduction process at cell level in nano - microscale activating electrical, chemical, or biochemical activity; for example, ion channels or integrins, the differentiation of mesenchymal cells into bone cells (osteocytes, osteoblasts and osteoclasts) and the interactions of those cells in the bone deposition and resorption processes [249]. Finally, in a macroscale, stimuli determine the mechanical properties of bone tissue, bone shape, and magnitude of the loads they can support. One example of shape and structure of bone adaptation due to mechanical loads is described in Wolff's law [250]–[252]. It states that bone adapts its internal and external form depending on the forces applied on it [253].

From the clinical point of view, mechanobiology is studied using *in-vivo* and *in-vitro* models. These methods can be expensive, time-consuming, and difficult to control and, in some cases, with ethical drawbacks. An alternative to these models are computational methods or *in-silico* experiments. Computational mechanobiology studies the effect of mechanical stimuli in the differentiation, growth, adaptation and maintenance of tissues, establishing qualitative and quantitative rules between the different variables involved in

these processes. In computational mechanobiology, numerical methods, generally finite element method FEM, are used to solve systems of equations describing the relationships between the variables and parameters of the studied phenomena. Whereas some variables and parameters of these processes may not be measurable, trial and error methods are applied. [254], [255].

4.1.1 Mechanical stimuli variables

A first task in computational mechanobiology is to determine which mechanical stimulus will serve as an input variable. It is still debated the mechanical stimuli that monitor the cells and the means they used to measure that signal [256]–[261]. Signals can be essentially a volumetric deformation component (change in size) and a deviatoric deformation component (change in shape). Several researchers have proposed various types of mechanical signals: Frost proposed a minimum stress value in the osseous tissue to trigger a bone apposition process [262], later, he changed the stress signal by a deformation signal [263], [264], Carter et al. propose the principal strain and hydrostatic stress as a mechanical signal [265], Claes and Heigele use the principal Strain and the hydrostatic pore pressure to study the fracture healing process [266], Lacroix and Prendergast use the deviatoric strain & fluid velocity to study tissue differentiation in fracture healing [267] and Huiskes studied Strain energy density or SED to predict bone remodeling [268]. The output variables help to describe the differentiation process (how many and which cell lines are produced), proliferation (which is the rate of growth), adaptation and maintenance of tissues (position and mechanical properties of formed tissues).

4.1.2 Regeneration and remodeling of bone tissues

The study of the bone regeneration process may consider tissue differentiation depending on the type and magnitude of the mechanical stimulus. There are four basic mechanoregulatory models of bone tissue differentiation. Pauwels postulated that high strains led to the formation of fibrous tissue, while higher pressures led to cartilage tissue [269]. Later, Carter proposed a model where the type of tissue depends on the direction and magnitude of the stress. For example, the osseous tissue is possible where stresses and deformations have low magnitudes due to tension [265]. Claes and Heigele [266]

developed a model that, unlike the previous two qualitative models, proposes ranges of values in which different types of tissues are obtained . For example, osseous tissue is generated by intramembranous ossification if the stress is ± 0.15 MPa and the strain is less than ±5%. Finally, Prendegrast proposed a model where tissues are not considered as a single material but as solid phase biphasic poroelastic materials. In this model, high fluid velocity values and deviatoric strains cause fibrous tissue [270].

Another line of research involves bone remodeling. This process includes the adaptation of the properties of the tissue that supports the mechanical loads. This line of work, developed by Carter and others [271], is one of the first to be used in computational models. It is considered that the bone tissue is a continuous system with variable apparent density ρ. This apparent density is expressed in terms of the stress σ to which the material is subjected. This is defined by the expression:

$$\rho = A\sigma^{\alpha} \tag{4.1}$$

Where A and α are constants. Considering α =0.5, it follows that:

$$\sigma^2 = 2EU \tag{4.2}$$

Where E is the elastic modulus and U the strain energy density. Regard to the elastic modulus E, experimentation leads to the relationship:

$$E = c\rho^3 \tag{4.3}$$

For example, one form of this equation that considers the viscoelastic behavior of the material is:

$$E_{axial} = C\dot{\varepsilon}^{0.06}\rho^3 \tag{4.4}$$

Where C is a constant that considers values of elastic modulus and density of reference while $\dot{\varepsilon}$ is the rate of deformation.

Therefore, and considering that bone remodeling is an optimization problem follows that the strain energy and bone density are related by:

$$\rho = c'U \tag{4.5}$$

4.1.3 Other processes

Besides bone regeneration and bone remodeling due to mechanical stimulus, other processes must be considered in bone tissue engineering. Sengers [151], in an extended review, analyzes the processes listed below:

- Proliferation: Growth of cell population due to mitosis. Exponential or logistic law are usually considered here [272], [273].
- Nutrient transport and consumption: nutrient concentration gradients due to cell population location and generation and disposal of waste substances. Regard the interaction of nutrient availability and cell proliferation reaction diffusion equations are employed as seen in [272], [273].
- Senescence: Decrease of cell population due to apoptosis [249], [274].
- Motility: Cells movement and adhesion throughout their environment due to taxis. Although, in bone remodeling and regeneration process is usually considered that osteoblasts are not migrating cells; models as random walk or diffusion sometimes are applied. Random walk is a stochastic process consists of a series of discrete steps of specific length. A random variable determine the step length and walk direction [68], [275]. Diffusion processes are used to predict osteoblast movement [276] or Darcy's law to model movement in porous media [277].
- Differentiation: Stem cells turn into other more specialized cell types. Regarding bone regeneration, mesenchymal cells turn into fibroblast, chondrocytes and osteoblasts due not only to mechanical signals as mentioned above but also to chemical factors.
- Extracellular matrix changes: cells like osteoblasts produce matrix components (i.e. collagen and hydroxyapatite) and matrix degradation may occur by the action of osteoclasts.

- Cell to cell interactions: Cells can communicate with each other in order to trigger processes. For example, osteocytes act as receptors of mechanical or chemical signals and dispose the formation of BMUs.

4.1.4 The Mechanostat Theory

Frost suggests that bone change must be considered in two phases: The internal, where the bone tissue changes its density, so its mechanical properties; and the external where there are changes due to the deposition or removal of osseous tissue on the bone surface [262]. In both cases the remodeling process is active depending on the value of the mechanical stimulus. It can be seen that in a range of mechanical stimulus, remodeling is inactive [268] (See Figure 4-1).

For external remodeling, the rate at which a bone is deposited or removed is given by:

$$\frac{dX}{dt} = C_x(U - U_n) \tag{4.6}$$

Where X is the thickness of the formed layer, U is the strain energy density (SED), U_n is a reference value and C_x is a proportionality constant. Similarly, the Young's modulus E change due to the mechanical stimulus is:

$$\frac{dE}{dt} = C_E(U - U_n) \tag{4.7}$$

Therefore, the description of the external remodeling process is given by:

$$\begin{aligned}
&\frac{dX}{dt} = C_x(U - (1+s)U_n) \text{ for } \mathrm{U} > (1+s)U_n \text{ (Bone formation)} \\
&\frac{dX}{dt} = 0 \text{ for } (1-s)U_n \geq U \leq (1+s)U_n \text{ (Lazy zone)} \\
&\frac{dX}{dt} = C_x(U - (1-s)U_n) \text{ for } \mathrm{U} < (1-s)U_n \text{ (Bone resorption)}
\end{aligned} \tag{4.8}$$

Meanwhile, the elasticity modulus change for internal remodeling is expressed as:

$$\frac{dE}{dt} = C_E(U - (1+s)U_n) \text{ for U} > (1+s)U_n \text{ (Stiffnessincrease)}$$
$$\frac{dE}{dt} = 0 \text{ for } (1-s)U_n \le U \le (1+s)U_n \text{ (Lazy zone)} \quad (4.9)$$
$$\frac{dE}{dt} = C_E(U - (1-s)U_n) \text{ for U} < (1-s)U_n \text{ (Stiffnessdecrease)}$$

This type of response model to mechanical stimulation is widely used in bone remodeling and bone regeneration simulations.

Figure 4-1: Rate of bone change as a function of the strain energy density (U). From: Frost [262].

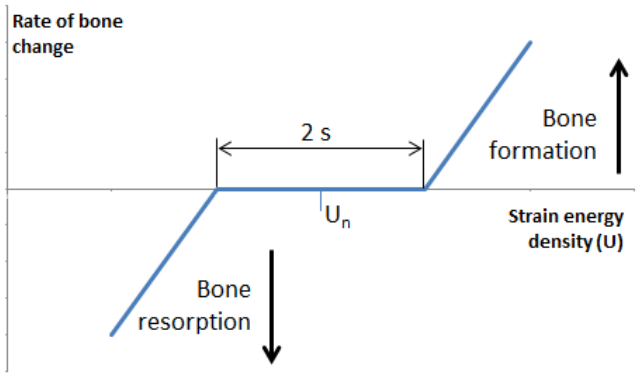

4.2 Mathematical modeling of bone regeneration on scaffolds

Considering the foregoing, there are two different and complex processes: Degradation, which decreases scaffold's mechanical properties and regeneration that increases stiffness and mechanical resistance of new bone tissue. Therefore, experimental [278]–[286] and computational models are required to show the system evolution over time and to help to identify the optimal initial properties of the scaffold when it is implanted. [103], [106], [109], [226], [287]–[297].

Computer simulations allow analyzing scaffold properties and their effect on growth rate and mechanical behavior of the tissue. Those models vary as different properties, assumptions, domains and solving approaches are considered. From the geometric point

of view the most studied property is porosity [68], [298], [299]. The development of additive manufacturing methods has generated interest in the effect of the shape and size of the scaffold pores. In those studies, a representative volume element (RVE), instead of the whole model of the scaffold, is studied [62], [226]. Simulations can be developed for different processes at different scales. At a nanoscale level, the mechanisms of cell adhesion to the walls can be studied [300], [301]. In the microscale, the effect of the shape and size of the pores can be considered [62], [226], and, at the meso and macroscale, the external shape of the scaffold and the effect of mechanical loads acting on it [100], [289], [302]. Finally, the use of homogenization and multiscale methods has allowed the researching of various phenomena influencing the process of bone regeneration [106], [303], [304] like substances transport [305], [306]. Some examples of computational mechanobiological models for fracture healing and bone regeneration on porous scaffolds are listed below in Table 4-1.

4.3 Computational implementation

In this section, three representative unit cells or volume elements representing the pores of the implant are studied. Each of the geometries of these cells was obtained from a reaction-diffusion model as discussed in Chapter 2. The cells are made from a cubic domain. In these domains, the degradation of the scaffold by hydrolysis (described in Chapter 3) and the growth of bone tissue which replaces the polymer, once this is completely hydrolyzed, were simulated. The model of scaffold degradation and bone tissue growth was implemented using the finite element method applied to a cubic mesh of 17576 nodes and 15625 elements. The side of the cube is assumed as 2.4 mm. All simulations consider a step increment of Δt = 1 day, until it reaches 130 days. It was considered that flow is null at the boundaries of the domain.

4.4 Results

This section presents the results of the degradation of the scaffold and the growth of bone tissue on it. Numerical tests were carried out with different parameters of the reaction-diffusion system in order to obtain three wave numbers that result into different geometrical configurations. Thus, the structure obtained from a wave number (2,2,0)

determines an inner structure formed by canals of uniform thickness, the structure obtained with the wave number (2,2,2) represents relatively uniform pores similar to a sphere and the wave number (4,2,2) would result into pores similar to ellipsoids.

Table 4-1: Computational mechanobiological models for fracture healing and bone regeneration on scaffolds

MODELED PHENOMENA	INPUT VARIABLE	OUTPUT VARIABLES	MATERIAL	CELLS CONSIDERED	REFERENCE
Fluid motion of a bone substitute applied to the high tibial osteotomy with three different wedge sizes	Fluid-induced shear stress	Elastic modulus, Poisson's ratio, porosity and permeability values that optimize the internal fluid motion			[307]
Cell growth In vitro vs. In silico	Local oxygen tension	Cell density	PLGA	Preosteoblast	[272]
Cell differentiation and proliferation on Biodegradable Scaffold	Shear strain and fluidic velocity	Cell differentiation Cell Growth Mechanical properties	PLGA	Mesenchymal cells Osteoblast Osteoclast Chondrocyte Fibroblast	[63]
Cell growth on porous scaffolds	Cell density	Cell density Pressure			[277]
Cell growth and distribution	Cell density	Cell density and distribution			[273]
Cell differentiation and proliferation on Biodegradable Scaffold	Porosity, Young's modulus and dissolution rate Shear strain and fluidic velocity	Cell differentiation	PLGA	Mesenchymal cells Osteoblast Osteoclast Chondrocyte Fibroblast	[68]
Cell differentiation and proliferation on Biodegradable Scaffold	scaffold stiffness, porosity, resorption kinetics, pore size and pre-seeding	Cell growth Scaffold mass loss permeability porosity	Polymer		[308]
Mechanical behavior and drug delivery	Stress Loads according different position in vivo	Drug release Stress	Hydroxyapatite		[309]
Cell growth and differentiation over implant porous surface	Force	Cell differentiation		Mesenchymal cells Osteoblast Osteoclast Chondrocyte Fibroblast	[310]
Proliferation and hypertrophy of chondrocytes in the growth plate	Stress	Cell proliferation		Chondrocyte	[311]

4.4.1 Scaffold canal-shaped

The Figure 4-2 shows the formation of the microstructure obtained for the variables *u* and *v*, when *s* is equal to 0,995 using the wave number (2,2,0). The reaction-diffusion system parameters were *d* = 8.6676, *a*= 0.1, *b* = 0.9 and γ = 230.82. The Turing pattern stabilized at a dimensionless time of *t* = 5.8, with a resulting porosity of 46%. The trabecular width obtained from the unit cell is 1.2 mm. Figure 4-2 a) and b) show the tissue regeneration and scaffold degradation, respectively. The Figure 4-3 shows the percentage of remaining volume of the scaffold as a function of time expressed in days. It is observed that 127 days are required for degradation and complete regeneration.

Figure 4-2: Bone tissue regeneration and scaffold degradation in a representative volume element obtained with a wave number (2,2,0). a) Growth of bone tissue. b) Degradation of the scaffold

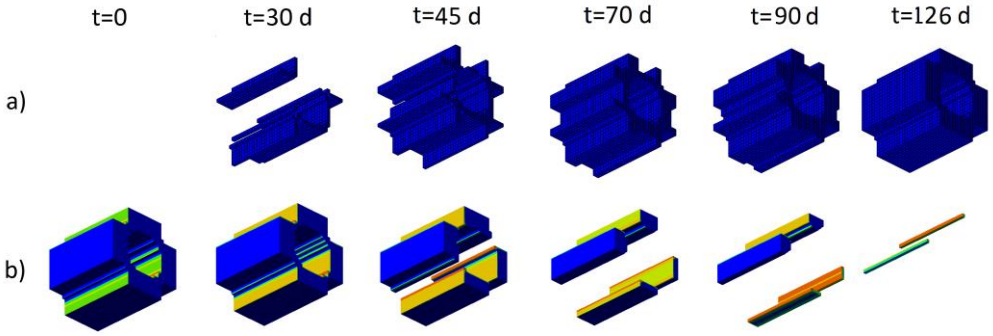

Figure 4-3: Bone tissue regeneration and scaffold degradation in a representative volume element obtained with a wave number (2,2,0) as a function of time

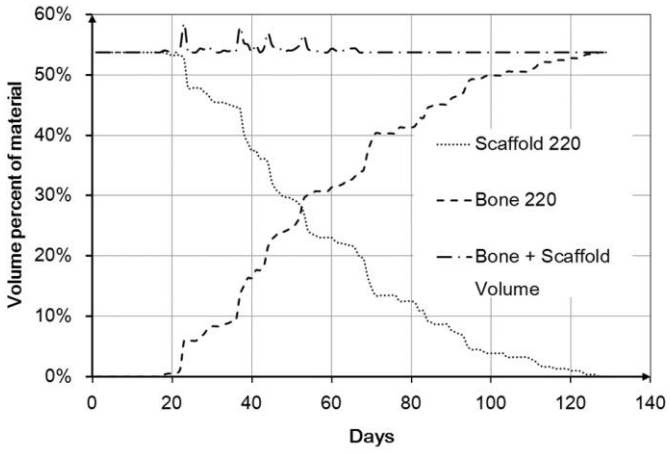

4.4.2 Scaffold with spherical pores

The Figure 4-4 shows the formation of the microstructure obtained for the variables *u* and *v*, when *s* is equal to 0,895 using the wave number (2,2,2). The reaction-diffusion system parameters were *d* = 8.6123, *a* = 0.1, *b* = 0.9 and γ = 346.3578. The Turing pattern stabilized at a dimensionless time of *t* = 8.4, with a resulting porosity of 32%. The trabecular width obtained from the unit cell is 1.2 mm. Figure 4-4 a) and 6 b) show the tissue regeneration and scaffold degradation, respectively. Figure 4-5 shows the percentage of remaining volume of the scaffold as a function of time expressed in days. It is observed that 118 days are required for degradation and complete regeneration.

Figure 4-4: Bone tissue regeneration and scaffold degradation in a representative volume element obtained with a wave number (2,2,2). a) Growth of bone tissue. b) Degradation of the scaffold

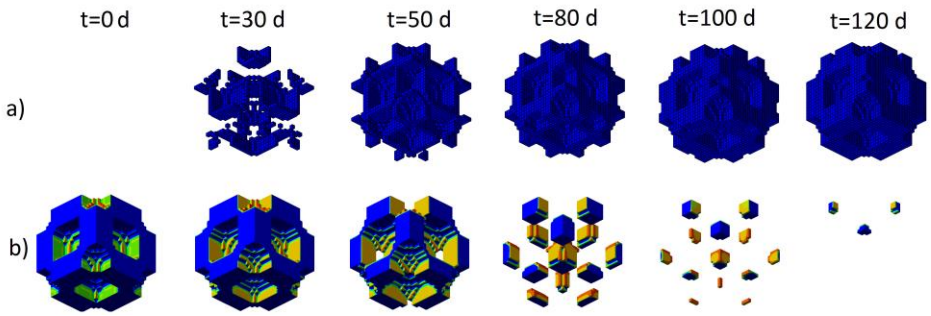

Figure 4-5: Bone tissue regeneration and scaffold degradation in a representative volume element obtained with a wave number (2,2,2) as a function of time

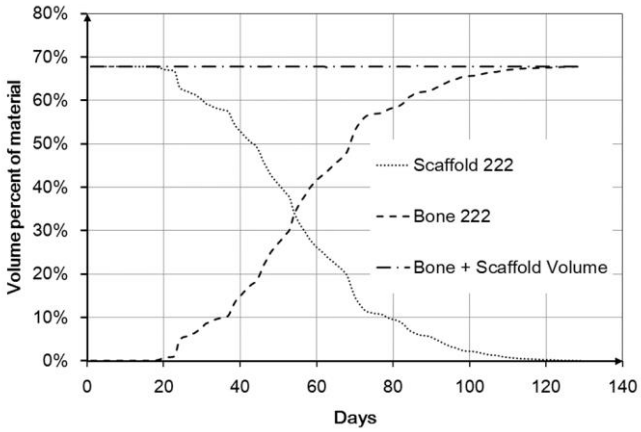

4.4.3 Scaffold with ellipsoid pore

The Figure 4-6 shows the formation of the microstructure obtained for the variables *u* and *v*, when *s* = *0.995* using the wave number (4,2,2). The reaction-diffusion system parameters are *d* = 8.5736, *a* = 0.1, γ = 700.4675, *b* = 0.9. The Turing pattern stabilized at a dimensionless time of *t* = 28.8, with a resulting porosity of 29.6%. The trabecular width obtained from the unit cell is 0,6 mm. Figure 4-6 a) and 9 b) show the tissue regeneration and scaffold degradation, respectively. Figure 4-7 shows that for this configuration, 91 days are required for the scaffold degradation and tissue regeneration.

Figure 4-6: Bone tissue regeneration and scaffold degradation in a representative volume element obtained with a wave number (4,2,2). a) Growth of bone tissue. b) Degradation of the scaffold.

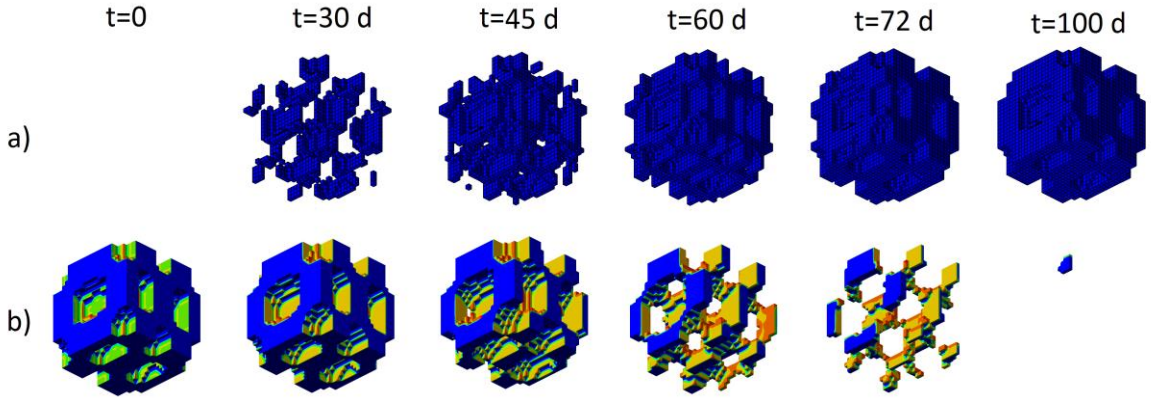

Figure 4-7: Bone tissue regeneration and scaffold degradation in a representative volume element obtained with a wave number (4,2,2) as a function of time

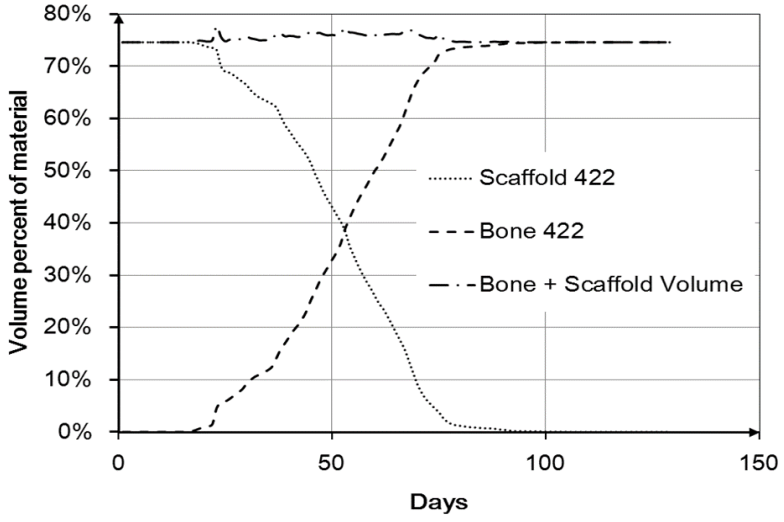

Finally, Figure 4-8 shows the evolution of the normalized mass remaining as a function of time as the degradation process occurs. After 20 days, the degradation begins to be considerable. It can be observed that the use of reaction-diffusion systems with a high wave number and higher porosity (4,2,2) decreases the time necessary for a complete degradation. We can also see that the degradation process in highly porous structures with a wave number (4,2,2), have higher smoothness in the evolution of degradation processes and bone formation than in structures with wave numbers (2,2,0).

Figure 4-8: Standard masses remaining in the degradation time of the three volumes considered for different wave numbers

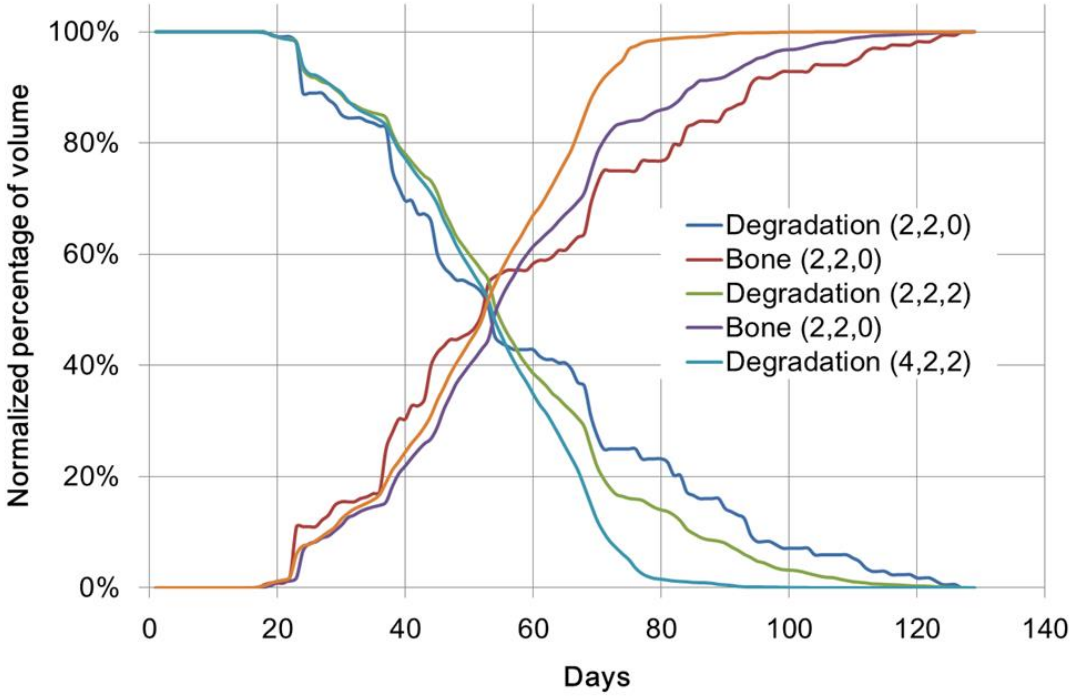

4.5 Discussion

The mechanobiological computational models of the bone regeneration and remodeling processes can assist the design of biodegradable scaffolds because they can help to understand the effect of scaffold properties on bone ingrowth, therefore, their results can

be used to optimize the scaffold structure in order to meet patient-specific mechanical and pore characteristics. A disadvantage of these models is that they involve many parameters whose values have to be estimated with in-vitro or in-vivo experimentation. It is necessary to rationalize the number of model parameters without loss of reliability of the numerical results.

The regeneration of bone tissue inside a biodegradable scaffold is a complex process in which two mechanisms act in a coupled manner. In the beginning of the sequence, a degradation process of the scaffold, where neither volumetric nor structural changes on the scaffold material, but a change on the mechanical properties of the polymer, due to hydrolysis, is observed. During this time, no appreciable growth of bone tissue is detected. After day 20, a rapid process of erosion is visible as loss of scaffold material in its periphery. This change triggers the growth of bone tissue on the scaffold. This phenomenon may be due to the change of the geometrical and mechanical properties of the scaffold that causes changes in the stress distribution acting as a mechanical signal which activates the bone regeneration process. It can be seen sustained growth of bone tissue between days 20 and 70 of the process (Figure 4-8). During this period, the regenerated bone assumes the mechanical function of the scaffold. After this time, the bone growth continues, but is lower for spherical pores or channels scaffolds represented in wave numbers (2,2,0) and (2,2,2) than those with ellipsoidal pores (4,2,2). The highest growth rate in the ellipsoidal pores could be explained by a larger surface area per unit volume which would facilitate cell adhesion. The results exposed here are similar to other works. Byrne et al. [68] study shows that in 60 days scaffolds regenerate between 70% and 85% of bone while the Gorriz et al. [312] study shows bone growth between 65% and 75% for the same period. Here bone growth is observed between 57% and 67% for 60 days as shown in Figure 4-8. Differences in percentages of regenerated tissue may be due to differences between different models as types of stimuli, phenomena and tissues considered.

In this study it can be seen that scaffolds lose their structural integrity depending on the shape of the pores and initial porosity. The scaffold with channels that had an initial porosity of 46% of their trabecular connectivity was lost by day 45. The scaffold with spherical pores which had an initial porosity of 32% of their trabecular lost connectivity at

day 65. Finally, the scaffold with ellipsoidal pores had an initial porosity of 24% of their trabecular losing connectivity at day 70. On the other hand, the regenerated bone tissue shows connectivity to day 45 for the scaffold with channels, by day 40 to the scaffold with spherical pores and from day 50 shows connectivity to the scaffold with ellipsoidal pores (Figures 4-2, 4-4 and 4-6).

As we can see in Figure 4.8, the simulations do not show an appreciable degradation in the first 20 days. This may be due to the time required to increase the concentration value of water in the interior of the trabeculae of the scaffold to be high enough to break the sufficient amount of molecular bonds. This allows the degradation of scaffold solid portion. From day 20 until day 50, approximately, we observed similar degradation rates. Finally, from day 50 there is degradation at different rates that lead to a high decrease of the mass in the element with ellipsoids pores.

Comparing with previous work, we can see that different approaches lead to similarities in the internal architecture of the scaffold. For example, from considerations of topology optimization, Almeida et al. [110] obtained structures similar to the canals and ellipsoids reported in this chapter. It is also noteworthy that the structures obtained in this work are similar to the surfaces used in previous works with gyroids surfaces [96], [313]. There is a previous report where reaction-diffusion systems may cause this type of surfaces [156]. On the other hand, the implementation of the model has a low computational cost since it required about 1000 or less time steps to model the complete degradation of each of the elements of the scaffold.

4.6 Conclusion

In this chapter some theoretical bases for the study were mechanobiology and analysis of bone regeneration processes on biodegradable polymers. It was shown that the rate of degradation, porosity and shape of the pores affect the rate of bone regeneration and, therefore, are important factors in scaffolds design. Mechanical strength can be increased by decreasing the porosity and degradation rate of the polymer. However, an important point for designing scaffolds is to make the growth rate of bone tissue the same at which the scaffold is degraded. Thus, there cannot be failures due to excessive mechanical load

for the amount of polymeric-tissue materials present in some instant or overgrowth of bone tissue in the periphery of the scaffold that closes the external pores. The scaffold design should ensure that this has stiffness as close to the bone to be regenerated. If stiffness is very low, there may be a fracture or deformation of the scaffold which can lead to premature collapse of the material or formation of other types of tissue like cartilage. If stiffness is too high may have stress shielding effects that weaken the surrounding tissue. It is in this type of studies where computer simulations can help to estimate the mechanical properties of the scaffold.

Although this work is similar to that described by other authors, it assumes a number of assumptions that must be taken into account to be improved in future works. For example, it is considered a hydrolysis process without autocatalysis and no change is set to the mechanical properties of tissue when it grows and matures. It is important that variables that represent the environment will be better defined. Regeneration processes in-vivo or in-vitro involve different processes and variables. For example, in an in-vivo scenario can occur growth of various types of tissue like connective, cartilage, and bone inside the scaffold, or an accumulation of acid products in the environment due to low vascularization, or low flow of medium for waste transport. Meanwhile, in in-vitro conditions can be growth of one class of tissue and pH level can be controlled within the scaffold using bioreactors. Besides, in order to obtain a more realistic model, the interaction with the environment should be considered.

5 Evaluation of geometric and mechanical properties of scaffolds for bone tissue applications manufactured with a Polyjet Printing system

5.1 Introduction

One of the major objectives of bone tissue engineering is to achieve similar geometries than those of trabecular bone. Up to date, there exist several methodologies for scaffolds design based on regular and irregular structures [72]. Most constructive approaches are based on regular arrangements: an internal geometry filled with a periodic distribution of unit cells. Unit cells are constructed with computer aided design (CAD) tools using design primitives like cylinders, spheres, cones, blocks organized in rectangular or radial layouts [135]. On the other hand, biomimetic design has been introduced and widely used as an alternative method for irregular porous structure modeling. However, a faithful reproduction of the structures present in nature, in most cases, is not strictly necessary: a simpler approach to the achievement of a biomimetic design to mimic tissues or organs functionality, is the global variation of porosity of the different regions according to a natural reference model [72], [314].

This chapter explores the modeling of geometric structures by reaction-diffusion models and the geometric and mechanical properties of these structures produced by additive manufacturing processes. For this purpose, porous structures are obtained from a Schnakenberg reaction-diffusion model. Later, those structures are fabricated using an additive manufacturing system and the capacity of these systems to reproduce the modeled geometry is estimated. Finally, structures stiffness is established by measuring

its modulus of elasticity. Results show that different geometrical characteristics of porous structures are possible by varying the parameters of the reaction-diffusion system. Additive manufacturing systems can reproduce complex geometries depending on the geometrical feature size; and, the modulus of elasticity determined by the geometric structure and specific characteristics of the selected manufacturing process.

5.2 Materials and methods

To obtain a porous structure that can be used as scaffold for osseous tissue engineering the process illustrated in Figure 5-1 is established. Based on a model of reaction diffusion it generates a geometric pattern in a specific domain. In this work the domains used are cube-shaped, cylindrical or wedge shaped. More complex shapes that resemble complete bones or portions of them may be used if it is required. From the retrieved pattern it is defined at the interior of the domain part which portions of it are considered solid (resembling trabeculae) or empty (representing pores). Once this process is done, a model of the scaffold geometry is obtained and it can be taken to manufacture using an additive manufacturing process.

Figure 5-1: Graphic description of the stages of the proposed process from scaffold design to manufacture

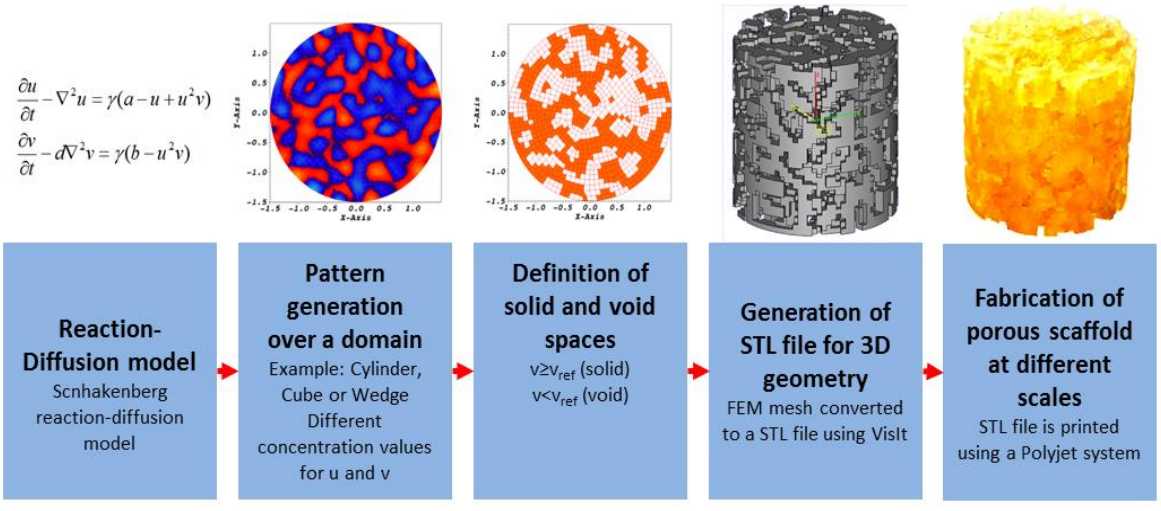

5.2.1 Geometry generation

Using the methodology proposed in chapter 2, a generation of geometric patterns will be done in three domains: a cube that has 3 mm in its side represented in a mesh 46656 nodes and 42875 cubic elements, a cylinder with a radius of 1.5 mm, 3.0 mm height represented in a mesh of 36312 nodes and 33462 elements and a wedge of minor height of 2.5 mm, major height of 3.5 mm, 4 mm length, and 3 mm width represented in a mesh of 29791 nodes and 27000 elements. Mesh elements are hexaedrical 8-node elements. The frontal views of the meshes are shown in Figure 5-3a, 5-4a and 5-5b respectively.

In order to solve the system of equations in the proposed domains, the finite element method along with the Newton-Raphson method programmed in FORTRAN are used. To obtain the porous structure from the previous process, elements that have a concentration value v above threshold value v_t are selected. They are defined by trial and error depending on the porosity that is desired to obtain.

Highest concentration of u are indicated with blue color and higher v concentrations are indicated for cube, the wedge and the cylinder in Figure 5-3b, 5-4b and 5-5b, respectively. To determine the porous structures, a threshold value of concentration v_{ref} is taken. V_{ref} values were obtained using a trial and error method as described in [76] in order to obtain porosities (void volume/domain volume) close to 50% that is the minimum porosity value recommended for bone scaffold applications. Porosity is calculated as V_o/V_f, where V_0 is the void space volume inside the V_f domain volume. The mesh elements that have a concentration value of v greater than v_{ref} are considered as solids. Finally, the resulting mesh of finite elements of the items selection process is displayed and exported to a STL file using the visualization software *VisIt* (Lawrence Livermore National Laboratory, Livermore, California, USA).

5.2.2 Scaffold Printing

The structure is manufactured using a 3D printing system Object Eden 260 (Stratasys, Eden Prairie, Minnesota, USA). This system uses the Polyjet technology that by means of a mobile jetting head on a horizontal plane sprays drops of photocuring liquid polymers in order to print the workpiece material and the support material. This deposition is done on

a tray that moves vertically to complete the three-dimensional construction (see Figure 5-2).

Figure 5-2: Polyjet printing system. The printed structure in Fullcure RGD720 material is embedded in the support material Fullcure 705

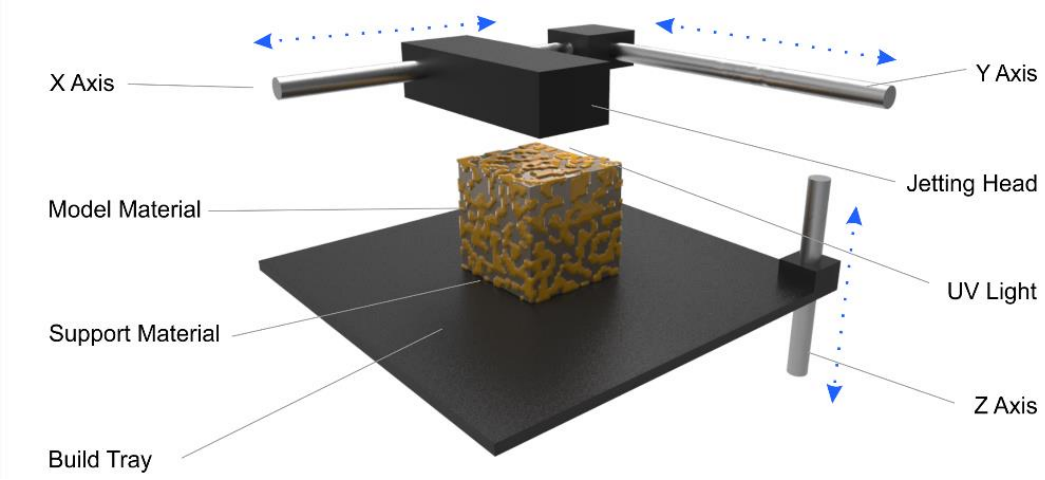

The materials used are Fullcure RGD720 (Elasticity modulus E = 2000 - 3000 MPa, Tensile Strength 55-60 MPa) for the structure material and Fullcure 705 for support material. Although the RGD720 material is not a biomaterial, it has mechanical properties similar to Fullcure MED610 that can be used in the printing system Polyjet and complies with ISO standard ISO 10993-1: 2009. It also has similar mechanical properties of modulus of elasticity compared with PDLLA (E = 1900 MPa), PLGA (E = 2000 MPa) or calcium phosphate compounds chitosan-gelatin (E = 3940 MPa to 10880 MPa) [130], [315].These materials are specific to this printing technology. The manufacturing is done at full resolution of manufacture of X-axis: 600 dpi; Y-axis: 600 dpi; Z-axis: 1600 dpi.

Scaffold fabrication is based on STL files. This is done at different scales (*1 x, 5x* and *10x*) with respect to the measures initially proposed for a better visualization of the designed geometry details. The software of additive manufacturing system calculates where to place the support material and the material that constitutes the piece to manufacture. The jetting head moves by placing and curing through ultraviolet light, the photopolymer and the support material that forms superimposed layers as the tray, descends vertically. Finally, the material is removed using water and air in a high-

pressure water cleaner (waterjet unit). Later curing of the workpiece material is not required.

5.2.3 Verification of mechanical properties and roughness

The measurement of the scaffolds geometric properties is carried out using an electron microscope scan or SEM (Scanning Electron Microscopy JSM-6010LA, JEOL, USA) and Outside Micrometer 103-138 (Mitutoyo, Japan) and the mechanical properties in a material testing machine (TinusOlsen H5KT single column materials testing machine, USA). Surface roughness was determined using a surface roughness tester (Surftest SJ-301, Mitutoyo, Japan).

In the case of mechanical properties, the scaffolds were subjected to compression tests according to the standard ISO604 Plastics - Determination of Compressive Properties, applying a load of 890 N (approx. 200 lbf). Stress strains were graphed in order to characterize the scaffolds behavior to compression loads and to obtain the variable elasticity module.

5.3 Results

5.3.1 Reaction diffusion model

Morphogens concentrations after a certain reaction time T_a form labyrinth distributions for each one of the proposed domains. In all cases the model parameters are $d = 8{,}6123$, $a = 0{,}1$, $\gamma = 346{,}3578$, $b = 0.9$. A value of $T_a = 2$ is used considering it is the minimum time to patterns occurrence. In addition, a computational parameter of $\Delta t = 0.01$ with a total number of increments of 2000 is used to solve the proposed equations system in (2). Elements with high concentrations of *u* will be considered void spaces and elements with high concentrations of *v* will be considered solid components in order to obtain porous structure that resembles a porous scaffold for bone tissue engineering applications. Loss of geometric features like curved details, appear in all domains due to a voxelization effect when the threshold value is applied to define the solid portion of the initial volume. The maximum and minimum values for *u* and *v* concentrations are displayed in Table 5-1.

Table 5-1: Concentrations u and v for cubic, cylindrical and wedge domains

CONCENTRATION	CUBE	CYLINDER	WEDGE
u	0.9603 - 1.044	0.9615 - 1.044	0.9603 - 1.044
v	0.08837 - 0.9179	0.8834 - 0.9169	0.8745 - 0.9248

In the cubic domain, the morphogen *v* forms a pattern with dots and stripes irregularly arranged over the domain (Figure 5-3b) similar to a high density trabecular bone [316]. To define the elements considered as solid scaffold components, a threshold value v_{ref} = *0,9008* is defined. Thus, the elements having a higher concentration than value v_{ref} conform a geometry made of plateau and rods components (visible as orange elements in Figure 5-3c). Therefore, a structure with channels and interconnected trabeculae are achieved. The mesh is subsequently exported to a STL file (Figure 5-3d). The solid obtained has a volume of *13,53* mm^3, a porosity of *57.54%* considering the volume of the cubic domain of *27* mm^3, a surface of *259,63* mm^2, *70652* facets and *33618* nodes.

Figure 5-3: Modeling and printing of a porous structure from a cubic domain. a) Front view of the finite element mesh, b) Concentration distributions *u* and *v*, c) Determination of the solid elements (orange) from the reference value, and d) three-dimensional model

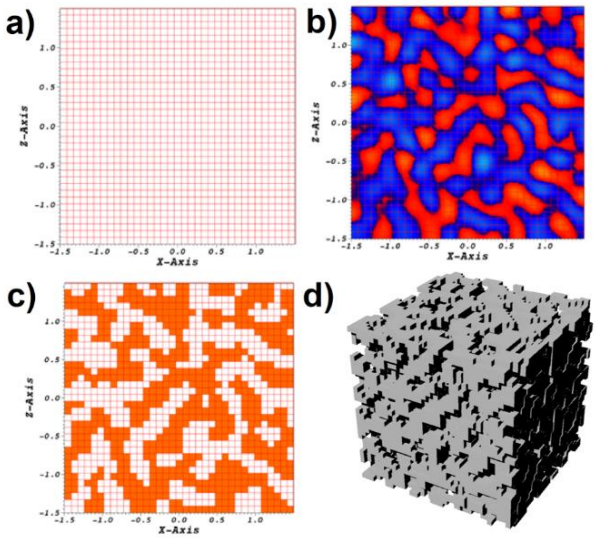

In the wedge domain, the morphogen *v* forms a pattern with dots and stripes irregularly arranged over the wedge domain (Figure 5-4b) in a similar way than the previous cube. To define the elements considered as solid scaffold components, a threshold value v_{ref} = *0,8997* is defined. A geometry with predominant plateau components oriented along the x axis is obtained (visible as orange elements in Figure 5-4c). The solid obtained has a

volume of volume of *17,56 mm*^{3}, a porosity of *48.79%* considering the wedge volume of *36 mm*^{3}, a surface of *315,06 mm*^{2}, *52264* facets and *24145* nodes (Figure 5-4d).

In the cylinder domain, the morphogen *v* forms a pattern with dots and stripes irregularly arranged over the domain (Figure 5-5b) in a similar way than the previous domains. To define the elements considered as solid, a threshold value v_{ref} = *0,9001* is defined. A geometry with plateau components is obtained (visible as orange elements in Figure 5-5c). The solid obtained has a volume of volume *10,80 mm*^{3}, a porosity of *50,93%* considering the volume of the cylinder of *21,21 mm*^{3}, a surface of *204,59 mm*^{2}, *55048* facets and *26143* nodes were obtained (see Figure 5-5d).

Figure 5-4: Modeling and printing of a porous structure from a domain in a wedge shape. a) Front view of the finite element mesh, b) distributions *u* and *v* in the wedge domain, c) determination of the solid elements (orange) from the reference value, and d) three-dimensional model

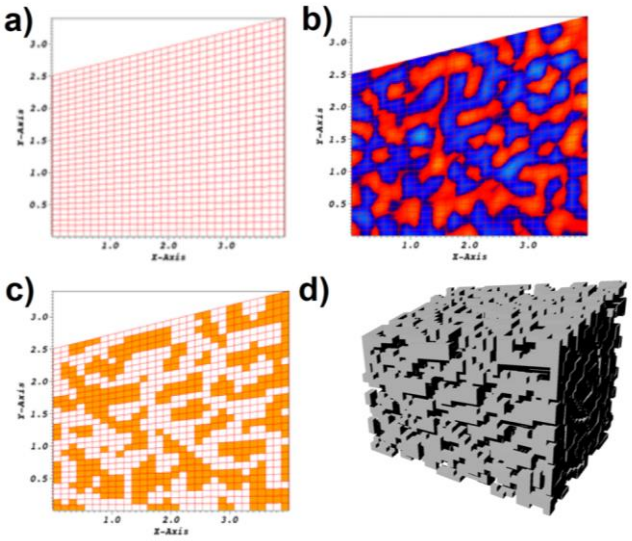

Additionally, to verify the possibility of controlling the porous structure, a different case over the same cylinder domain is proposed with parameters *d = 8,5737*, *a = 0,1*, *γ = 700,4675*, *b = 0.9* solved in value of T_a = *15* in order to obtain a Turing pattern following the methodology described in [317]. A porosity of *50,93%* is achieved when a threshold value v_{ref} = *0,9012* is defined. It can be seen that channels and trabeculae are oriented in parallel to cylinder base as showed in Figure 5-6.

Figure 5-5: Modeling and printing of a porous structure from a domain in the form of cylinder. a) Front view of the finite element mesh, b) distributions *u* and *v* in the cylinder domain, c) Determination of the solid elements (orange) from the reference value, and d) three-dimensional model

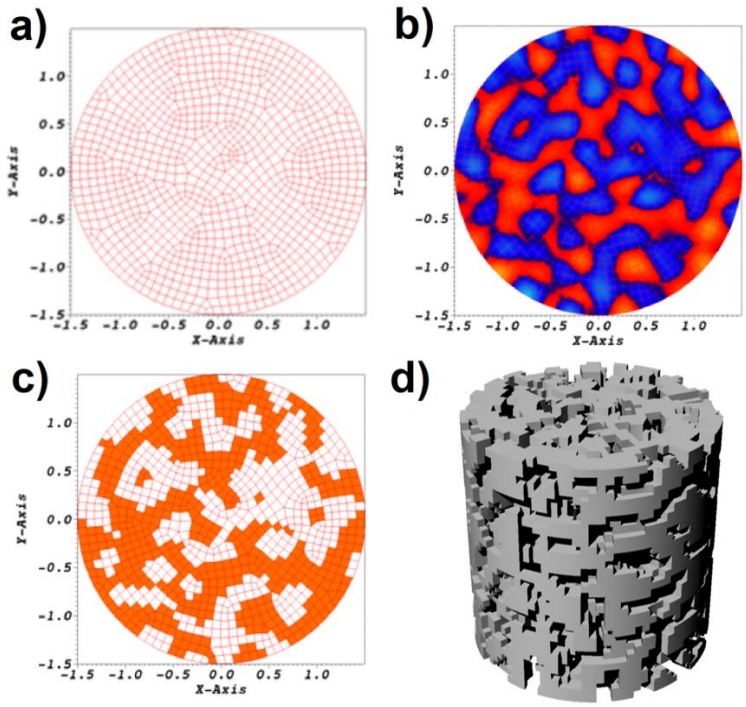

Figure 5-6: Modeling and printing of a porous oriented structure from a domain in the form of cylinder

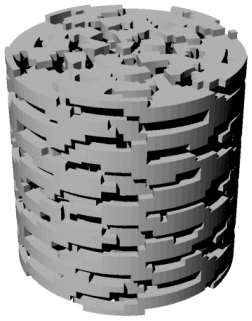

5.3.2 Analysis of manufactured scaffolds

Using the models in STL format, different scaffolds were fabricated using the Polyjet additive manufacturing system to make an analysis of geometric properties. The cube-shaped scaffold was printed at *1x*, *5x* and *10x* scales to review the ability of the printing

system to reproduce details of the designed geometry (see Figure 5-7). Assessment between designed models and obtained parts is made by visual inspection.

External dimensions vary slightly depending on the surfaces orientation respect to the printing direction. Dimensions perpendicular to the print direction were on average 0,12 mm greater than the design dimensions. While the dimensions in the x axis were 0.05 mm less than the nominal dimension.

The measurement of the trabeculae in the scaffold scale *10x* shows that trabeculae can be up to *0.1 mm* wider in the *x* and *y* directions inside scaffolds faces and up to *0.05 mm* at the trabeculae close to the vertexes (Figure 5-7). This causes the width of the channels are lesser than the designed dimension. For example, when the geometry is printed to a *1x* scale, the channels having the width of an element of the domain (*0,086 mm*) are smaller than the space of *0,1 mm* estimated to be occupied by sobrematerial and therefore they are not reproducible.

Figure 5-7: Comparison between designed geometry and Polyjet technology made cubic scaffold geometry at *10x* scale. a) and b) Nominal measurements details of trabeculae and channel in the STL model, c) trabecular detail at the corner, d) L shape pore, e) trabecular measurements in a vertex half (compare with STL detail in b).

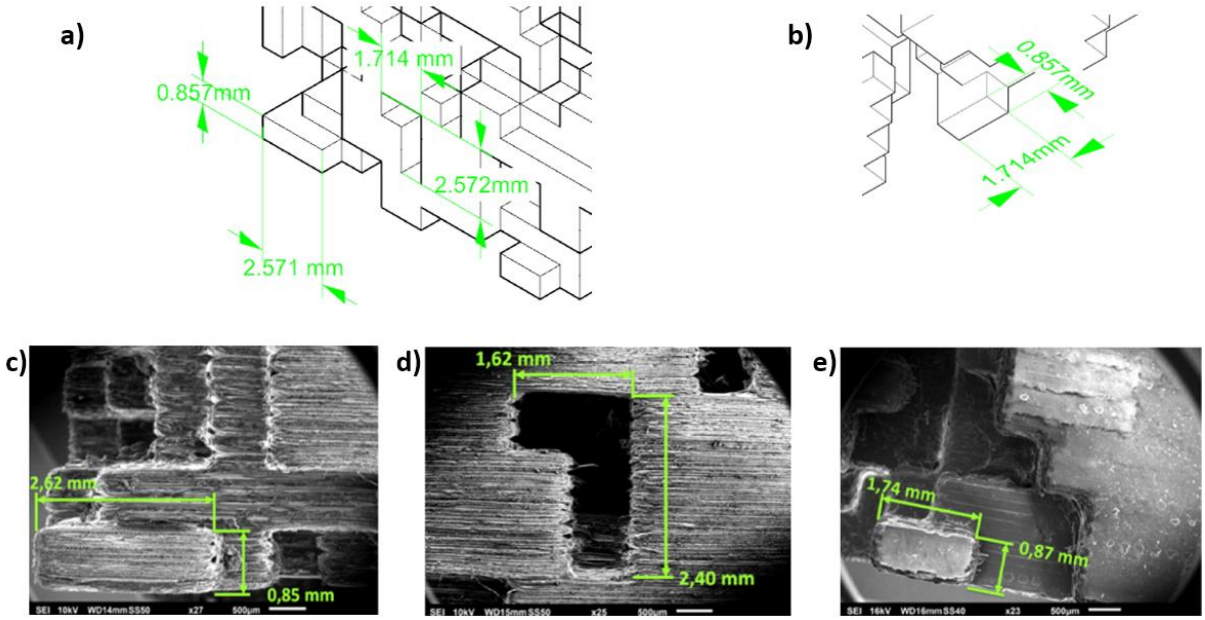

It is not possible to obtain right angles both in concave and also the convex details of the geometry. There are rounding radii among *250 µm* and *360 µm* according to the face orientation in regard to the *z* axis and edges proximity. Straight corners have been rounded by effect of systems used for the removal of the support material which can cause wear on the details with straight angles. Wear causes a decrease in dimensions as can be seen in trabeculae close to the scaffold edge. Rounded corners can be seen in cubic scaffold at *10x* scale (Figure 5-7) as well as in cubic scaffold at *5x* scale (Figure 5-8).

Figure 5-8: Details of finished surfaces of Polyjet technology made cubic scaffold at *5x* scale. a) Trabecula at the corner of the scaffold in the STL model b) Trabecula details at the middle of a vertex in the STL model, c) Trabecula at the corner of the scaffold in the manufactured scaffold, d) Trabecula at the middle of a vertex in the manufactured scaffold.

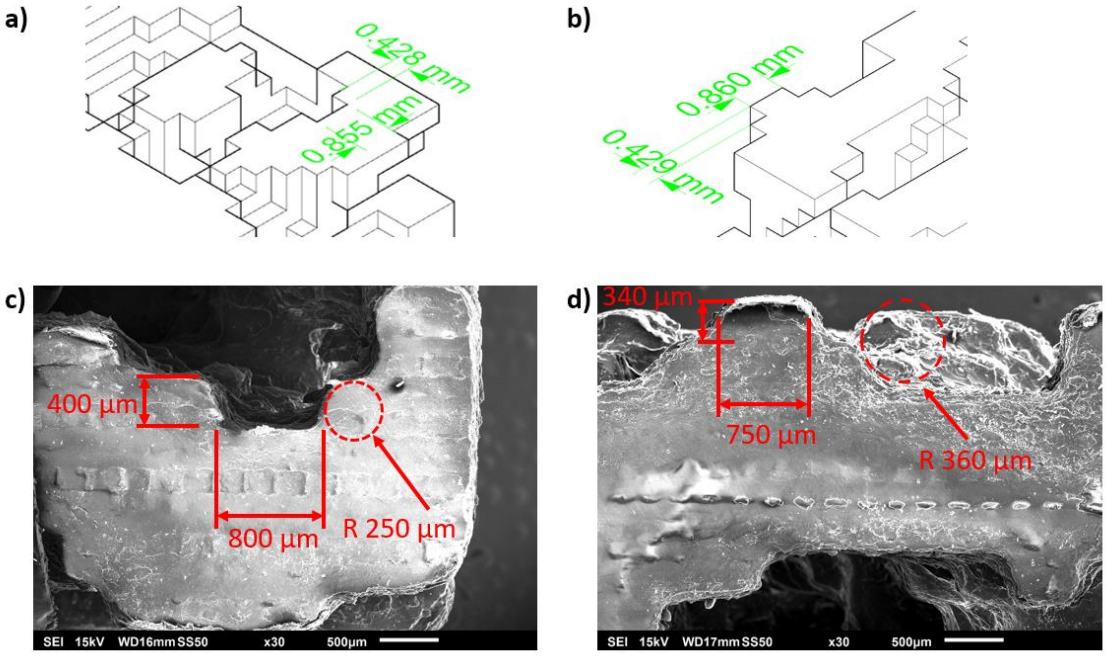

The designs of STL files and printed elements have different degrees of similarity depending on the printing scale. The general form of geometric features as trabeculae and channels are visible at *5x* and *10x* printing scales; but, at *1x* scale, it is not possible to appreciate the internal structure of the scaffold. It seems that the material occupies the whole space of the channels. Therefore, the printed scaffold does not replicate the details of trabeculae and pores properly (Figure 5-9).

Figure 5-9: Micrograph Polyjet technology made cubic scaffold at *1x* scale

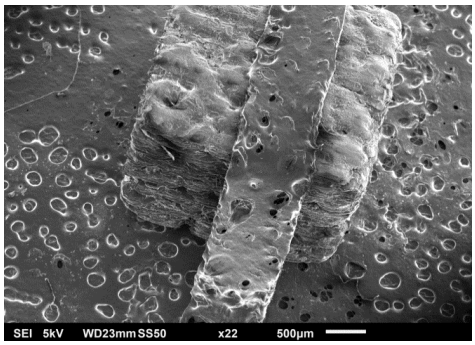

5.3.3 Surface roughness

The surface roughness has a defined orientation and its value depends on the surface position in respect to the *z* axis which is the printing axis (Figure 5-10). Parallel faces to the printing axis have an average roughness *Ra=4,55µm*. The profile of the surfaces is not uniform and has peaks and valleys making the maximum height of the roughness profile *Rz* to raise to *30.28 µm* (Figure 5-11a). These faces have grooves clearly oriented in the direction where material layers were deposited. On the other hand, perpendicular faces to the printing axis show a smoother surface with an average roughness *Ra* of *0.40µm* although still appreciable irregularities cause the total height of valley-to-peak, can be up to *Rz = 4.02 µm* (Figure 5-11b).

Figure 5-10: Detail of the scaffold surface on a surface parallel to the *z* axis direction

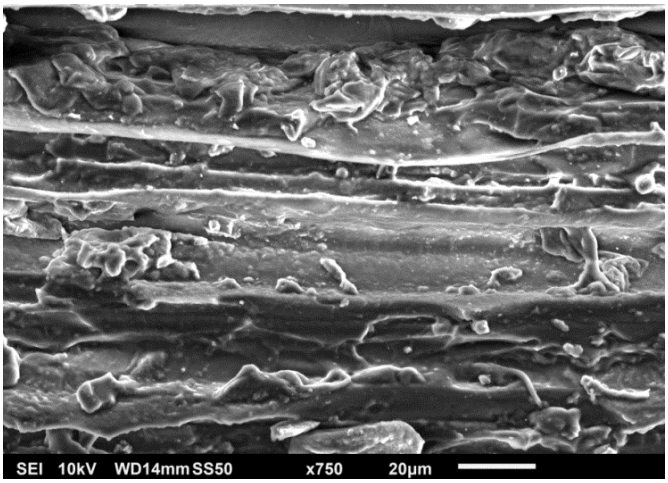

5.3.4 Mechanical properties

The mechanical behavior evaluation of the designed scaffolds is made by the following assessments: test compression of the cubic scaffold printed at *5x* scale in each of its three axes to evaluate the anisotropy of the element, test compression of cylindrical scaffolds at *5x* scale and *10x* scale to check the size effect on the properties and compression tests of cylindrical scaffold with oriented channels at *5x* scale to evaluate the effect of pore geometry.

Figure 5-11: Surface textures and roughness profiles of manufactured scaffolds a) Surface parallel to the *z* axis direction, b) Surface perpendicular to the *z* axis direction

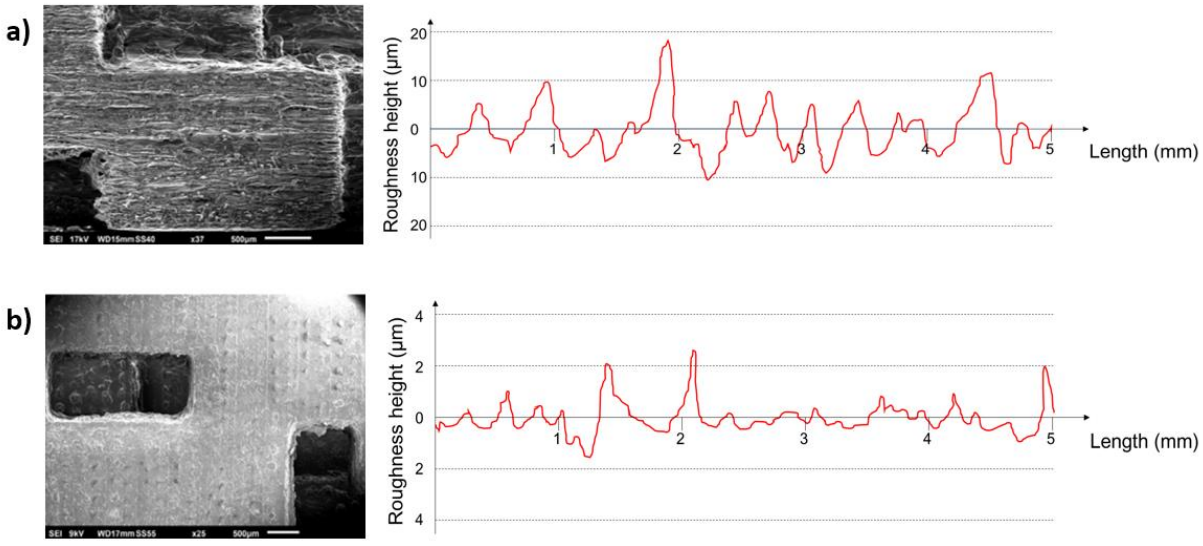

The cubic solid at *5x* scale exhibits an anisotropic elastoplastic behavior with a strain hardening stage at the end of the stress-strain curve. The modulus of elasticity in the linear portion of the stress-strain curve corresponds to $E_x = 68\ MPa$, $E_y = 64\ MPa$ and $E_z = 32\ MPa$ (Figure 5-12) in *x*, *y* and *z* axis respectively. It can be seen that elasticity modulus in the *z*-axis is almost *50%* of the measured at the other two axes.

It is evident a size effect in mechanical properties in cylindrical scaffolds. There is a non-linear behavior in scaffold printed at *5x* scale different to the almost linear behavior exhibited for the same geometry printed at *10x* scale. Besides, it is visible an increase in

the elasticity modulus from E_z = *66 MPa* to E_z = *125 MPa* on each scaffold respectively (Figure 5-13 and Figure 5-14).

Figure 5-12: Stress - Strain curve by applying axial compression load on the on *x*, *y* and *z* axis of the cubic scaffold at *10x* scale

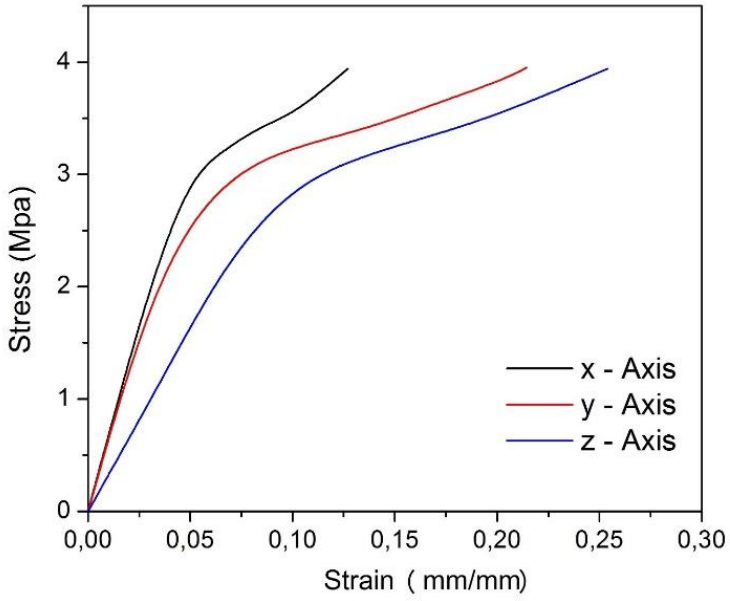

Figure 5-13: Stress - Strain curve by applying axial compression load on the *z* axis of the cylindrical scaffold with random pores at *5x* scale

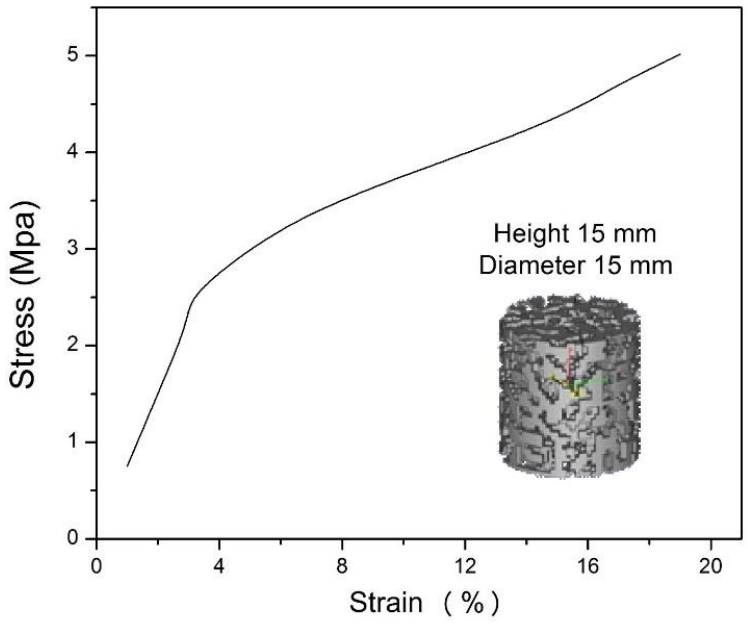

Figure 5-14: Stress - Strain curve by applying axial compression load on the *z* axis of the cylindrical scaffold with random pores at *10x* scale

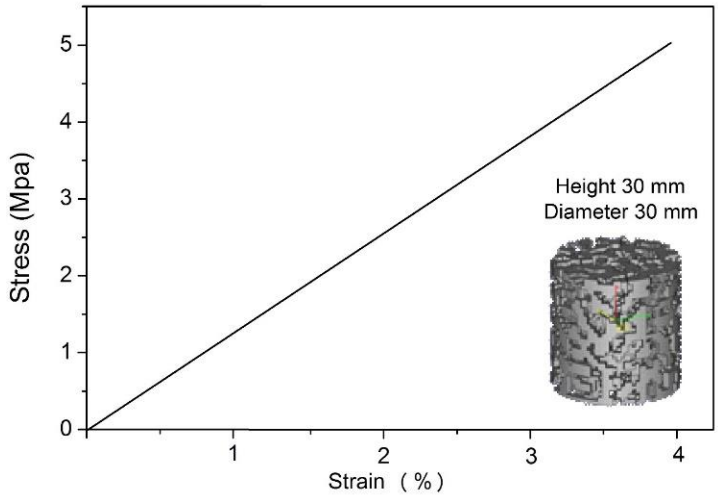

Pore size and orientation change the mechanical behavior of cylindrical scaffolds. Oriented channels scaffold exhibit an elasticity modulus of $E_z = 10\ MPa$ at the beginning of stress-strain curve lower than elasticity modulus of scaffold at *5x* scale even they have the same external size and similar porosity. A strain hardening behavior is also evident (Figure 5-15).

Figure 5-15: Stress - Strain curve by applying axial compression load on the *z* axis of the cylindrical scaffold with oriented pores at *5x* scale

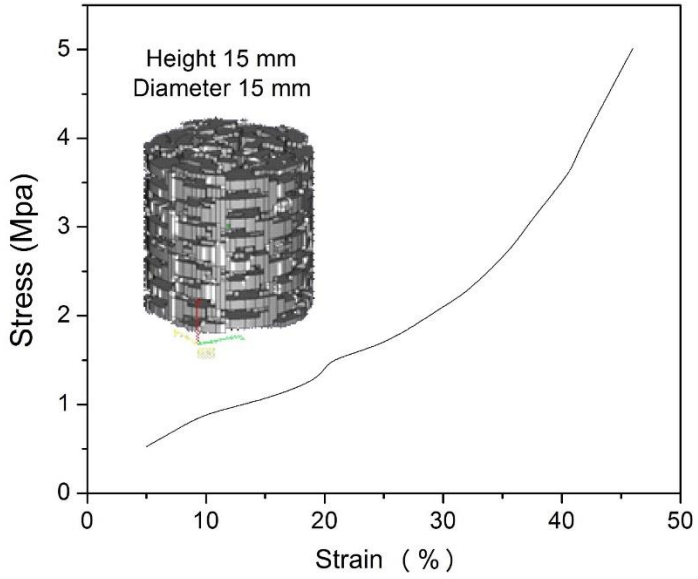

5.4 Discussion

The studied reaction-diffusion system generates an interconnected network of channels and trabeculae. Although the components of the structure are dispersed in the domain trabeculae and channels, width is relatively uniform. This may be due to local activation - by lateral inhibition principle proposed by Gierer and Meinhardt [318]. From this principle, it is possible to generate a periodic distribution of morphogens forming an arrangement that resembles dots or lines, those figures combined can form different configurations. These patterns may be irregular as described in [319], or periodic minimal surfaces similar to those studied by De Wit et al [320]. Besides reaction-diffusion systems parameters, the shape of porous structure is determined by the size of mesh elements. A smaller element size can result in a geometric pattern that more closely resembles the visible distribution pattern of morphogens before the application of threshold value V_{ref} to define solid elements. The smaller size of the elements decreases the voxelization effect but has the disadvantage of greater computational cost. To improve this aspect, smoothing surface from voxels can be obtained using techniques such as marching cubes [321] and additional work must be done in order to determine the appropriate size of the elements of the mesh to achieve a balance between geometry resolution and computational cost to solve the reaction-diffusion system. It is also important to study how the element size affects the size of the trabeculae or channels generated. For now, it is suggested that the element size should not exceed the recommended maximum pore size that can be close to 800 µm [76], [322].

Considering the manufacturing process, it is appreciated that the Polyjet system adequately reproduces geometry details. This can be attributed to the printing system used in this work that allows a high resolution of up to 16 µm compared to 100 µm of FDM or 3DP printing and SLS 80 µm process resolution [323]. In a similar way to these systems, variations in the geometry and mechanical properties are influenced by the orientation of the printing axis [140], [324].

Dimensional errors that can be up to 0.1 mm agree with other printing systems such as SLS [140], [145]. But the intricate geometry obtained by the reaction-diffusion system make difficult the deletion of the support material. This issue limits the minimum pore size which can be used for geometry design. It was also visible that the methods for support

material removal cause wear especially at the edges of the scaffold as shown in Figure 5-8. This raises the need for studies that consider how to design the scaffold considering the effects orientation in the size of the channels and the effects of cleaning the support material.

The surface roughness of a scaffold helps to increase the surface where cells can be attached promoting proliferation. It is estimated that the roughness must be of the same order of size of osteoblasts (2-8 μm) to influence attachment and growth rates [325]. Roughness of Ra = 4.55 μm present in surfaces parallel to the printing axis, is similar to the roughness of scaffold surfaces with other polymers [326], [327]. This roughness could facilitate cell adhesion and differentiation of mesenchymal cells into osteoblasts [328]. On the other hand, in the case studied, roughness is the most affected feature by the orientation of the surfaces relative to the axis printing. This phenomenon could be used to control cell growth, as the preferential orientation of roughness profile can influence cell proliferation direction and osteoblasts depending on the surface roughness for proper adhesion [329], [330].

Results of Figure 5-12 show a scaffold with transversely isotropic or orthotropic behavior. Similar modules elasticity in the x and y axis were obtained, which differ from those obtained in the z axis. This may be by reason of the material orientation due to the layer by layer printing system, or the mechanical properties of the scaffolds that can be modulated according to pores orientation. The mechanical properties obtained are similar to those of scaffolds made from unit cells repeated in space [331] [332], to those of scaffolds designed from periodic minimal surfaces [139] or bone tissue whose properties are conditioned by the orientation of the collagen fibers that compose it [333], [334]. Furthermore, the strain hardening observed in the stress-strain curves of Figure 5-13, 5-14 and 5-15 may prevent apoptosis by high stress or deformation [335] or prevent so high deformations that do not promote formation of bone but cartilage [27,28].

This is important because the mechanical properties condition the processes of tissue regeneration in two ways: The tissue will grow faster in areas with higher mechanical stimulus that will correspond to greater stress or strain [262]. Moreover, stem cells differentiate in osteoblast cells in more rigid areas and chondrocytes in less rigid areas

[238], [269]. That is, bone regeneration tends to follow the direction of apparent maximum stiffness; therefore, if pores are oriented, it is possible to modulate the rate and type of created tissue. Computer simulations and experimental tests must be made to quantify the contribution of design and printing systems in the anisotropy of the observed mechanical properties. The subsequent work may include the effect of mechanical properties gradient not only of geometrical characteristics as porosity but also the possibility of working with blending materials with gradient properties taking advantage of the Polyjet printing system.

The print scale significantly affects geometry and mechanical properties of the printed parts. Resolution of the printed object and the fidelity with which the scaffold reproduces details of designed geometry depends on the ratio between the width of the channels and dimensional error due to printing method. Besides, an increase in print scale tends to cause a linear behavior in the stress-strain curve as shown in Figure 5-14.

Finally, results of elasticity modulus for the manufactured scaffolds are within the range of elastic modulus between 10 and 1000 MPa reported for trabecular bone [336]. More precisely, the elasticity modulus are similar to those available for trabecular tissue in tibia and vertebrae according to the data available on Lakatos [334] so they could be used for scaffolds to replace trabecular bone tissue in those bones.

5.5 Conclusion

This chapter presents a method for generating irregular porous geometries that can be used in designing scaffolds for bone tissue applications besides geometric and mechanical properties after they were manufactured by a Polyjet printing system. The difference between the STL model geometry and the manufactured might be due to inherent characteristics of the manufacturing processes used, such as resolution, printing scale, and cleaning methods to remove support material. It is also observed that the orientation of the surfaces with respect to the direction of deposition is a very important factor affecting the mechanical and geometric properties of the produced parts. All the above factors cause an anisotropic behavior that can be taken into account in a more realistic modeling of the scaffold geometric features and physical properties.

6 Conclusions and perspectives

This thesis presents a study of the factors involved in the design, manufacture, and performance of degradable scaffolds for bone tissue engineering. The main conclusions are as follows:

- A geometry obtained from the simulation of a reaction diffusion process can be a starting point for the design and manufacture of scaffolds for bone tissue engineering.
- A design methodology based on analyzing reaction-diffusion system parameters for controlling geometry features was developed. It has been shown that complex structures with pores or channels can be obtained. The size and distance between those geometric features are relatively uniform. Although the structures obtained may have seemed disorderly or randomly organized, trabecula widths were relatively uniform.
- The ability to vary implant pore size and orientation can be used to provide anisotropic physical properties similar to those observed on bones.
- The typical nonlinear behavior of reaction-diffusion systems could be observed with small parameter changes in all simulations and domains, causing significant changes in the morphology of the obtained pattern and the interaction between various reaction-diffusion system parameters.
- The concept that a scaffold for tissue engineering must be removed as new tissue grows is widely accepted by the scientific community. However, the change of mechanical properties like stiffness can lead to a scaffold premature failure. To avoid this problem, it is important to know how the scaffold degradation and erosion occurs but this is a complex and challenging task.
- The degradation model used here is the basis for describing the behavior of the polyesters utilized as biomaterials since hydrolysis is the main degradation

mechanism for these polymers. However, more complex models that contemplate autocatalysis besides enzymatic or mechanical process are required to obtain results closer to real material behavior.

- In the case of PLA, bulk erosion is the phenomenon that usually occurs due to hydrolysis. But surface erosion should be preferred because its effects on mechanical properties are easier to control. Therefore, it is desirable to use high molecular weight polymers.
- It was shown that the rate of degradation, porosity and shape of the pores affect the rate of bone regeneration and, therefore, are important factors in scaffolds design.
- Mechanical strength can be increased by decreasing the porosity and degradation rate of the polymer.
- The geometric differences between the modeled and the fabricated scaffold might be due to inherent characteristics of the manufacturing processes such as resolution, printing scale and cleaning methods to remove support material.
- It is also observed that the orientation of the surfaces with respect to the material deposition direction is a very important factor affecting the mechanical and geometric properties of the produced parts. They cause an anisotropic behavior that must be considered in order to obtain a more realistic modeling of the scaffold geometric features and physical properties.
- Computational models of bone regeneration can contribute to the design process because they can help to understand the effect of scaffold properties on bone ingrowth. A disadvantage of these models is that they involve many parameters whose values have to be estimated with in-vitro or in-vivo experimentation that was not considered in this work.

In summary, the scaffold design process implies many considerations: biofunctionality, biocompatibility, biodegradability, mechanical properties, and porosity that are among others the most important ones. Therefore, biodegradable scaffold design is a complex process: there are contradictions between the design parameters which must be solved, i.e., high porosity versus high mechanical stiffness. Scaffolds must be designed using tailor-made parameter values in order to satisfy functional requirements for specific patients, thus it is necessary to estimate individual porosity, pore size and mechanical

properties of the tissue to be replaced. Finally, scaffolds must be designed considering the manufacturing process.

On the other hand, considering what has been done in this thesis, the research perspectives are concerning the different elements involved in bone tissue engineering:

- Design of irregular porous structures obtained through simulation of reaction-diffusion or stochastic processes. This line of work is relatively new and should be considered as an alternative to the current design lines of scaffolds proposing relatively uniform structures. It proposes irregular structures that more closely resemble the trabecular bone, and its geometry would be less susceptible to sudden failure or crack propagation.
- This type of porous and irregular designed geometry requires additive manufacturing methods that do not require support material. Therefore, development of biomaterials for fabrication by stereolithography or sintering methods must be done.
- The effect of the principles of operation of manufacturing methods in geometric and physical properties of the manufactured scaffolds should be studied in depth.
- The computer simulation must be accompanied with in-vitro or in-vivo experiments. Once obtained the scaffold, studies with osteoblast cultures in them must be carried and gradually increase the amount of factors, as adding types of stimulation and cells. Then, animal models can be performed in order to feedback the computer simulations.
- An extension of this study is necessary in order to analyze the effect of domain size and elements of the mesh used in the FEM method with respect to the wave length of the patterns obtained.

7 Appendix A: Dimensionless model of the Schnakenberg reaction-diffusion system

Let the dimensional reaction-diffusion equation given by (A.1):

$$\frac{d[X]}{d\tau} = D_1\nabla^2[X] + K_1[A] - K_2[X] + K_3[X]^2[Y] \qquad (A.1)$$
$$\frac{d[Y]}{d\tau} = D_2\nabla^2[Y] + K_4[B] - K_3[X]^2[Y]$$

Let the variables $[X]$, $[Y]$ and the time τ values defined by (A.2):

$$[X] = u*[X_{REF}] \qquad (A.2.1)$$
$$[Y] = v*[Y_{REF}] \qquad (A.2.2)$$
$$\tau = t*T \qquad (A.2.3)$$

Where *u, v* and *t* are the dimensionless values, and X_{REF}, Y_{REF} and *T* are the references values of the process to be studied. Also, considering that X_{REF} and Y_{REF} have the same order of magnitude, it can be assumed that $Z = X_{REF} = Y_{REF}$. Replacing (A.2) in (A.1) gives (brackets omitted):

$$\frac{Z}{T}\frac{du}{dt} = ZD_1\nabla^2 u + K_1[A] - ZK_2 u + Z^3K_3u^2v \qquad (A.3.1)$$
$$\frac{Z}{T}\frac{dv}{dt} = ZD_2\nabla^2 v + K_4[B] - Z^3K_3u^2v \qquad (A.3.2)$$

Furthermore, the Laplacian can be dimensionless using $\mathbf{x} = \bar{\mathbf{x}} * L$, then (A.4) is obtained:

$$\nabla^2(*) = \frac{1}{L^2}\bar{\nabla}^2(*) \qquad (A.4)$$

Where L is the reference value of length, $\bar{x}$ is the dimensionless value of ***x*** coordinate and $\bar{\nabla}^2(*)$ is the Laplacian for which derivatives are made with respect to the dimensionless $\bar{x}$ coordinate. Using (A.4), replacing in (A.3) and by algebraic manipulation gives (A.5.):

$$\frac{du}{dt} = \frac{TD_1}{L^2}\nabla^2 u + \frac{K_1 T[A]}{Z} - TK_2 u + TZ^2 K_3 u^2 v \quad \text{(A.5.1)}$$

$$\frac{dv}{dt} = \frac{TD_2}{L^2}\nabla^2 v + \frac{K_4 T[B]}{Z} - TZ^2 K_3 u^2 v \quad \text{(A.5.2)}$$

Following [1], [11] is possible to choose $D_1 = \frac{L^2}{T}$ and $Z = \sqrt{\frac{K_2}{K_3}}$, then (A.6) is given by:

$$\frac{du}{dt} = \nabla^2 u + TK_2\left(\frac{K_1[A]}{K_2}\sqrt{\frac{K_3}{K_2}} - u + u^2 v\right) \quad \text{(A.6.1)}$$

$$\frac{dv}{dt} = \frac{D_2}{D_1}\nabla^2 v + TK_2\left(\frac{K_4[B]}{K_2}\sqrt{\frac{K_3}{K_2}} - u^2 v\right) \quad \text{(A.6.2)}$$

Therefore, it is possible to choose the following dimensionless numbers (A.7):

$$\gamma = TK_2 \quad \text{(A.7.1)}$$

$$a = \frac{K_1[A]}{K_2}\sqrt{\frac{K_3}{K_2}} \quad \text{(A.7.2)}$$

$$b = \frac{K_4[B]}{K_2}\sqrt{\frac{K_3}{K_2}} \quad \text{(A.7.3)}$$

$$d = \frac{D_2}{D_1} \quad \text{(A.7.4)}$$

In order to have the biomaterial equation dimensionless (A.8) is considered:

$$\frac{dM}{d\tau} = C\frac{[X]^n}{[X]^n + [S]^n}\frac{\tau^p}{\tau^p + T_1^p} \quad \text{(A.8)}$$

Choosing again the dimensionless values as in (A.2) equation (A.9) is:

$$\frac{M_{REF}}{T}\frac{dm_s}{dt} = C\frac{u^n}{u^n + \left(\frac{[S]}{Z}\right)^n}\frac{t^p}{t^p + \left(\frac{T_1}{T}\right)^p} \tag{A.9}$$

Where $M=m_s*M_{REF}$, with m_s equals to the dimensionless value of concentration biomaterial and M_{REF} is the concentration reference value. Using some algebra (A.10):

$$\frac{dm_s}{dt} = \frac{CT}{M_{REF}}\frac{u^n}{u^n + \left(\frac{[S]}{Z}\right)^n}\frac{t^p}{t^p + \left(\frac{T_1}{T}\right)^p} \tag{A.10}$$

Where the dimensionless numbers are given by (A.11):

$$c = \frac{CT}{M_{REF}} \tag{A.11.1}$$

(A.11.2)

$$s = \frac{[S]}{Z} \tag{A.11.3}$$

$$T_a = \frac{T_1}{T}$$

8 Appendix B: Analysis of dimensionless Schnakenberg reaction-diffusion model

For the case of the reaction-diffusion Schnakenberg model, the reaction-diffusion system (2) can be written as (B.1):

$$\begin{aligned} &\frac{\partial u}{\partial t} - \nabla^2 u = \gamma(a - u + u^2 v) \\ &\frac{\partial v}{\partial t} - d\nabla^2 v = \gamma(b - u^2 v) \end{aligned} \quad \text{en } \Omega \tag{B.1}$$

Where u, v are the chemical species, $\nabla^2 u$ and $d\nabla^2 v$ the diffusive terms and $f(u,v) = (a - u + u^2 v)$ and $g(u,v) = (b - u^2 v)$ reactive terms. Moreover, γ is a dimensionless constant and a and b are constant parameters of the model. Neumann homogeneous conditions have been imposed and initial conditions are small perturbations around the homogeneous steady state of each of the reactive terms, so $f(u_s, v_s) = 0$ and $g(u_s, v_s) = 0$

Conditions for instability by diffusion

From Murray [165] we can establish that without the presence of the diffusive term, u and v must satisfy (B.3):

$$\begin{aligned} &\frac{du}{dt} = \gamma(a - u + u^2 v) \\ &\frac{dv}{dt} = \gamma(b - u^2 v) \end{aligned} \tag{B.2}$$

For small perturbations around the steady state (ξ, η) (i.e. $(u,v) = (u_s + \xi, v_s + \eta)$), equation (B.2) is linearized as (B.3):

$$\underbrace{\begin{pmatrix} \frac{\partial u}{\partial t} \\ \frac{\partial v}{\partial t} \end{pmatrix} = \begin{pmatrix} \frac{\partial \xi}{\partial t} \\ \frac{\partial \eta}{\partial t} \end{pmatrix}}_{\frac{\partial \Psi}{\partial t}} = \gamma \underbrace{\begin{pmatrix} f_u & f_v \\ g_u & g_v \end{pmatrix}}_{J} \underbrace{\begin{pmatrix} \xi \\ \eta \end{pmatrix}}_{\Psi} \tag{B.3}$$

Where $f_u = 2uv - 1$, $f_v = u^2$, $g_u = -2uv$ and $g_v = -u^2$. In (6), a series expansion took place and terms of order greater than 2 have been neglected. It should be noted that $f(u,v)$ and $g(u,v)$ are evaluated at a steady state $(u_s, v_s) = \left(a+b, \frac{b}{(a+b)^2} \right)$.

A solution to (B.3) can be written as (B.4):

$$\mathbf{\Psi} \cong \mathbf{a} e^{\lambda_t t} \tag{B.4}$$

Where **a** is a vector containing information on initial conditions. Replacing (B.4) in (B.3) gives (B.5):

$$\left(\mathbf{J} - \lambda_t \mathbf{I}\right)\mathbf{a} = \mathbf{0} \tag{B.5}$$

Where $\mathbf{I}$ is the identity matrix. For a nontrivial solution it is required $\det\left(\mathbf{J} - \lambda_t \mathbf{I}\right) = 0$, the following characteristic equation is obtained (B.6):

$$\lambda_t^2 - \underbrace{\left(f_u + g_v\right)}_{tr(\mathbf{J})} \lambda_t + \underbrace{\left(f_u g_v - f_v g_h\right)}_{\det(\mathbf{J})} = 0 \tag{B.6}$$

Then (B.3) is linearly stable if and only if the conditions (B.6) for which the real part of the eigenvalues λ_t are negative. Note that these conditions are analogous to the Routh-Hurwitz [165]:

$$\begin{aligned} tr(J) &= f_u + g_v < 0 \\ Det(J) &= f_u g_v - f_v g_h > 0 \end{aligned} \tag{B.7}$$

If a diffusive term is considered the linear differential equation is (B.8):

$$\frac{\partial \mathbf{\Psi}}{\partial \mathrm{t}} = \gamma \mathbf{J} \mathbf{\Psi} + \mathbf{D} \nabla^2 \mathbf{\Psi} \tag{B.8}$$

With $\mathbf{D} = diag(1, d)$. Using the homogeneous boundary conditions ($(n \bullet \nabla)\Psi = 0$), equation (B.8) can be solved by variables separation, with $\mathbf{\Psi(x,}t) = \varphi\mathbf{(x)\varphi}(t)$, so a solution of the form (B.9) is obtained:

$$\Psi(\mathbf{x},t) = \sum_k \mathbf{c_k} e^{\lambda t} \varphi_k(\mathbf{x}) \qquad \text{(B.9)}$$

Where k is the wave number or eigenvalue of the spatial pattern described in [28], $\mathbf{c_k}$ is Fourier coefficients vector and $\varphi_k(\mathbf{x})$ is the eigenfunction of the Laplacian (with $(n \bullet \nabla)\varphi = 0$) given by (B.10):

$$\nabla^2 \varphi_k + k^2 \varphi_k = 0 \qquad \text{(B.10)}$$

Replacing (B.9) in (B.10) gives:

$$\left(\lambda \mathbf{I} - \gamma \mathbf{J} + \mathbf{D}k^2\right)\mathbf{c_k} = \mathbf{0} \qquad \text{(B.11)}$$

Where $\mathbf{0}$ is the zero vector and $\mathbf{I}$ is the identity matrix. As in the case of the differential equation without diffusion, requires that the vector of Fourier coefficients is not trivial, so you must verify the following condition:

$$\det\left(\lambda \mathbf{I} - \gamma \mathbf{J} + \mathbf{D}k^2\right) = 0 \qquad \text{(B.12)}$$

Then a dispersion relation (or characteristic equation of (B.11)) can be written as (B.13):

$$\begin{aligned} &\lambda^2 + b(k^2)\lambda + c(k^2) = 0, \text{con} \\ &b(k^2) = k^2(1+d) - \gamma(f_u + g_v) \\ &c(k^2) = dk^4 - \gamma(df_u + g_v)k^2 + \gamma^2(f_u g_v - f_v g_u) \end{aligned} \qquad \text{(B.13)}$$

Therefore, if Turing instability occurs, the roots of (B.13) must satisfy $\mathrm{Re}\,\lambda(k^2) > 0$ for any k^2. According to Ruth-Hurwitz conditions, real part of the eigenvalues is positive, it is required $b(k^2) > 0$ and $c(k^2) < 0$, or vice versa. From the condition (B.7 1) it can be concluded $b(k^2) > 0$ for all k^2. So $c(k^2) < 0$ is required.

Equation (B.13) shows that $d > 0$ and using (9.2) is known that $f_u g_v - f_v g_u > 0$, so $df_u + g_v > 0$, must be satisfied although it is a necessary but not sufficient condition. Additional relation is found by minimizing $c(k^2)$ where they must meet $c_{\min}(k^2) < 0$. This is done by $\frac{dc(k^2)}{dk^2} = 2dk^2 - \gamma(df_u + g_v) = 0$, where (B. 14) is obtained:

$$k^2 = \frac{\gamma(df_u + g_v)}{2d} \tag{B.14}$$

Replacing (B.14) in (B.13.3) yields (b.15):

$$c_{\min}(k^2) = -\frac{(df_u + g_v)^2}{4d} + (f_u g_v - f_v g_u) < 0 \tag{B.15}$$

From which the last condition for Turing instability is obtained. Reorganizing the conditions to be met, in summary, the following inequalities (B.16) are defined:

$$\begin{aligned} & f_u g_v - f_v g_u > 0 \\ & f_u + g_v < 0 \\ & df_u + g_v > 0 \\ & (df_u + g_v)^2 > 4d(f_u g_v - f_v g_u) \end{aligned} \tag{B.16}$$

B.1.1. Wave number definition. From [167] in points where $c_{\min}(k^2) = 0$ a bifurcation parameter is obtained. Therefore, from (B.16.4) $c_{\min}(k^2) = -\frac{(d_c f_u + g_v)^2}{4d_c} + (f_u g_v - f_v g_u) = 0$ determines the bifurcation point, for a value d_c, called critical diffusion coefficient, above from this point Turing instabilities are obtained. Therefore, the critical value of diffusion d_c is given by (B.17):

$$f_u d_c^2 + 2(2 f_v g_u - f_u g_v) d_c + g_v^2 = 0 \tag{B.17}$$

On the other hand, making $c(k^2)=0$ the value k^2 for which there is a range of possible wave numbers is obtained as long as $d > d_c$. This is shown in Figure 1.B.

Figure 8-1: Graphics for $c(k^2)$. Each curve is drawn for the Schnakenberg reaction model with $a=0.1$, $b=0.9$ and $\gamma=176.72$. Previously, using equation (19) $d_c=8.5676$ has been found. Using d_c and replacing its value in $c(k^2)$ (equation (15.3)) red curve is obtained. The magenta curve is obtained with $d=8.0$ and the green curve is obtained for $d=9.1676$. In the graphic $K^2_{\min}=43.1469$ and $K^2_{\max}=78.9525$

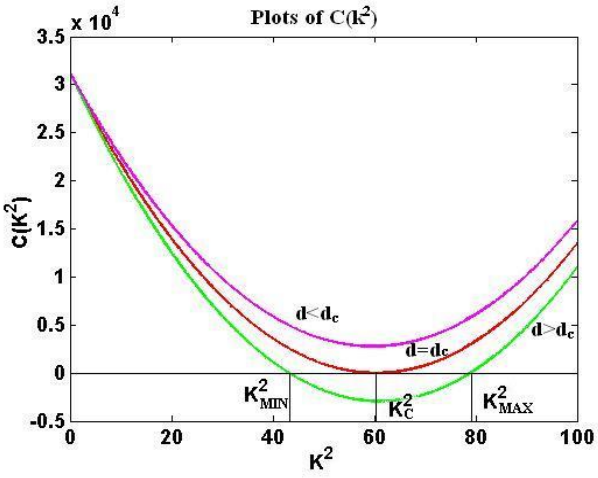

As shown in Figure 1.B, if $d > d_c$ it is satisfied at the intersecting point of $c(k^2)$ with k^2 axis (in other words, points where $c(k^2)=0$) two important points can be obtained, $K^2_{\min}$ y $K^2_{\max}$. These points define a range where the wave numbers or eigenvalues present the solution of the reaction-diffusion system. These values are given by:

$$K^2_{\min}=\frac{\gamma(df_u+g_v)-\sqrt{(\gamma(df_u+g_v))^2-4d\gamma^2(f_ug_v-f_vg_u)}}{2d} \qquad (B.18)$$

$$K^2_{\max}=\frac{\gamma(df_u+g_v)+\sqrt{(\gamma(df_u+g_v))^2-4d\gamma^2(f_ug_v-f_vg_u)}}{2d}$$

The interval $(K^2_{\min},K^2_{\max})$ defines the wave number of the reaction-diffusion system solution in a Turing space. To define the behavior of the instability it is necessary to define

the domain over which the solution takes place. In [1, 28] is solved on a square, but for generality information about a rectangle will be provided.

B.1.2 Eigenfunctions of a rectangle. Consider a rectangle which sides lengths are L_x and L_y in *x* and *y* directions respectively [1, 28]:

$$R = \left\{(x, y) \in \Re^2 \middle| 0 < x < L_x \wedge 0 < y < L_y \right\} \tag{B.19}$$

In [28] could be verified that eigenfunctions for the equation (B.9) are given by (B.20):

$$\varphi_k = \varphi_{L_x, L_Y} = \cos\left(\frac{m\pi x}{L_x}\right)\cos\left(\frac{n\pi y}{L_y}\right) \tag{B.20}$$

Eigenvalues are of the form:

$$k^2 = \pi^2\left(\frac{m^2}{L_x^2} + \frac{n^2}{L_y^2}\right) \tag{B.21}$$

When $t \to \infty$, the solution of the linearized system (B.8) takes the form:

$$\Psi(\mathbf{x}, t) = \sum_{m,n \in I} \mathbf{c}_{m,n} e^{\lambda t} \cos\left(\frac{m\pi x}{L_x}\right)\cos\left(\frac{n\pi y}{L_y}\right) \tag{B.22}$$

Where

$$I = \left\{(m, n) \in Z^2 \middle| K_{\min}^2 < \pi^2\left(\frac{m^2}{L_x^2} + \frac{n^2}{L_y^2}\right) < K_{\max}^2 \right\} \tag{B. 23}$$

For example, in the case shown for Figure 1.B, with $a = 0.1$, $b = 0.9$, $\gamma = 176.72$ and $d = 9.1676$, it follows that $K_{\min}^2 = 43.1469$ and $K_{\max}^2 = 78.9525$. Then, in a unitary square ($L_x = L_y = 1.0$) interval is given by ($4.3717 < m^2 + n^2 < 7.9996$). It is necessary to choose m y n so that they comply the whole proposed range. In this case the values are $m = 2$ and $n = 1$, or vice versa. In conclusion, the wave number is given by (2.1). Following a

similar analysis yields Table B.1 [28] where wave numbers and values for d and γ with constant values $a = 0.1$ and $b = 0.9$ are observed.

Table 8-1: Vibration modes (m,n) for different values of d and γ for Schnakenberg model [28]

MODE (m, n)	d	γ
(1,0)	10.0000	29.0000
(1,1)	11.5776	70.6000
(2,0)	10.0000	114.0000
(2,1)	9.1676	176.7200
(2,2)	8.6676	230.8200
(3,0)	8.6176	265.2200
(3,1)	8.6676	329.2000
(3,2)	8.8676	379.2100
(3,3)	8.6076	535.0900
(4,0)	8.6676	435.9900
(4,1)	8.5876	492.2800
(4,2)	8.7176	625.3500
(4,3)	8.6676	666.8200
(4,4)	8.6076	909.6600

9 Appendix C: List of Publications

Peer-reviewed papers:

- D.A. Garzón-Alvarado, M.A. Velasco, C.A. Narváez-Tovar, Self-assembled scaffolds using reaction-diffusion systems: a hypothesis for bone regeneration, Journal Of Mechanics In Medicine And Biology, ISSN: 0219-5194, Vol. 11, P. 231-272, 2011

- D.A. Garzón-Alvarado, M.A. Velasco, C.A. Narváez-Tovar, Modeling porous scaffold microstructure by a reaction-diffusion system and its degradation by hydrolysis, Computers in Biology and Medicine, ISSN: 0010-4825, Vol. 42, P. 147-155, 2012

- M.A. Velasco, D.A. Garzón-Alvarado, Bone Tissue Formation under Ideal Conditions in a Scaffold Generated by a Reaction-Diffusion System, Molecular & Cellular Biomechanics, ISSN: 1556-5297, Vol.10, P. 137-157, 2013

- M.A. Velasco, D.A. Garzón-Alvarado, C.A. Narváez-Tovar, Design, Materials, and Mechanobiology of Biodegradable Scaffolds for Bone Tissue Engineering, BioMed Research International, ISSN: 2314-6141, Vol. 2015, Article ID 729076, 21 pages, doi:10.1155/2015/729076, 2015

- M.A. Velasco, D.A. Garzón-Alvarado, Y. Lancheros, Geometric and mechanical properties evaluation of scaffolds for bone tissue applications designing by a reaction-diffusion models and manufactured with a material jetting system, Journal of Computational Design and Engineering, ISSN: 2288-4300, Vol. 3, P. 385–397, 2016

- M.A. Velasco, D.A. Garzón-Alvarado, Implantes Scaffolds para regeneración ósea. Materiales, técnicas y modelado mediante sistemas de reacción-difusión, Revista Cubana de Investigaciones Biomédicas, ISSN: 0864-0300, Vol.29, P. 140-154, 2010

- D.A. Garzón-Alvarado, M.A. Velasco, Aplicación de sistemas reacción-difusión en el diseño de la geometría interna de matrices para regeneración ósea, Revista Cubana de Investigaciones Biomédicas, ISSN: 0864-0300, Vol. 30 P.83-96, 2011

- M.A. Velasco, D.A. Garzón-Alvarado, Desarrollo de los modelos computacionales de remodelación ósea, Revista Cubana de Investigaciones Biomédicas, ISSN: 0864-0300, Vol. 30, P. 163-173, 2011

- D.A. Garzón-Alvarado, M.A. Velasco, Modelado de la degradación hidrolítica de un implante óseo, Revista Cubana de Investigaciones Biomédicas, ISSN: 0864-0300, Vol. 31, P. 210-222, 2012

Abstracts selected for oral presentation

- M.A. Velasco, D.A. Garzón-Alvarado, Mathematical modeling of bone regeneration on biodegradable scaffolds, International Conference on Computational & Experimental Engineering and Sciences ICCES 2012, Chania, Greece, May 2012

- M.A. Velasco, D.A. Garzón-Alvarado, C.A. Narváez-Tovar, Bone Tissue Regeneration in a Biodegradable Scaffold, 12th International Symposium on Computer Methods in Biomechanics and Biomedical Engineering CMBBE2014, Amsterdam, Netherlands, October 2014

10 Bibliography

[1] Ministerio de Salud Colombia, “Sistema Integral de Información de la Protección Social,” 2013. [Online]. Available: http://www.sispro.gov.co/. [Accessed: 11-May-2016].

[2] J. A. Buckwalter, J. D. Heckman, and D. P. Petrie, “Aging of the North American population: new challenges for orthopaedics,” *. J. Bone Jt. Surg.*, vol. 85A, pp. 748–758, 2003.

[3] Ministerio de Salud Colombia, “Observatorio Nacional de Discapacidad,” *Mapa dinámico*, 2016. [Online]. Available: http://ondiscapacidad.minsalud.gov.co/indicadores/Paginas/Mapa-dinamico.aspx. [Accessed: 11-May-2016].

[4] C. Satizábal, O. Calderón, and A. García, “Avances en el manejo de heridos en combate en el Hospital Militar Central de Bogotá, Colombia,” *Rev. Med*, vol. 14, no. 1, pp. 116–121, 2006.

[5] Dirección contra minas, “Víctimas de Minas Antipersonal,” 2016. [Online]. Available: http://www.accioncontraminas.gov.co/estadisticas/Paginas/victimas-minas-antipersonal.aspx. [Accessed: 11-May-2016].

[6] M. Bohner, “Resorbable biomaterials as bone graft substitutes,” *Mater. Today*, vol. 13, no. 1–2, pp. 24–30, Jan. 2010.

[7] E. S. Place, N. D. Evans, and M. M. Stevens, “Complexity in biomaterials for tissue engineering,” *Nat. Mater.*, vol. 8, no. 6, pp. 457–470, Jun. 2009.

[8] Ministerio de Salud Colombia, “Datos globales donacion transplantes, 2014,” 2015. [Online]. Available: https://www.minsalud.gov.co/sites/rid/Lists/BibliotecaDigital/RIDE/VS/MET/Datos-Globales-Donacion-Trasplantes.pdf. [Accessed: 11-May-2016].

[9] J. E. Aubin and J. N. M. Heersche, “Bone Cell Biology Osteoblasts, Osteocytes, and Osteoclasts,” in *Pediatric Bone: Biology & Diseases*, F. H. Glorieux, J. M.

Pettifor, and H. Juppner, Eds. Elsevier Inc., 2003, pp. 43–75.

[10] J. Lian, “The Cells of Bone,” *Proteins*, 2006.

[11] S. C. Cowin, *Bone Mechanics Handbook*, 2nd ed. New York, NY, USA: CRC Press LLC, 2001.

[12] O. Fricke, Z. Sumnik, B. Tutlewski, A. Stabrey, T. Remer, and E. Schoenau, “Local body composition is associated with gender differences of bone development at the forearm in puberty,” *Horm. Res.*, vol. 70, no. 2, pp. 105–111, Jan. 2008.

[13] S. Weiner and H. D. Wagner, “The material bone: Structure-Mechanical Function Relations,” *Annu. Rev. Mater. Sci.*, vol. 28, no. 1, pp. 271–298, Aug. 1998.

[14] L. C. Chow, “Solubility of calcium phosphates,” *Monogr. Oral Sci.*, vol. 18, pp. 94–111, Jan. 2001.

[15] M. Wendel, “Bone Matrix Proteins: Isolation and Characterization of a Novel Cell-binding Keratan Sulfate Proteoglycan (Osteoadherin) from Bovine Bone,” *J. Cell Biol.*, vol. 141, no. 3, pp. 839–847, May 1998.

[16] C. M. Gundberg, “Matrix proteins,” *Osteoporos. Int.*, vol. 14, no. Supplement 5, pp. S37–S42, Sep. 2003.

[17] P. G. Robey *et al.*, “Structure and molecular regulation of bone matrix proteins.,” *J. bone Miner. Res.*, vol. 8, no. Supplement 2, pp. S483–S487, Dec. 1993.

[18] S. J. Morrison and D. T. Scadden, “The bone marrow niche for haematopoietic stem cells,” *Nature*, vol. 505, no. 7483, pp. 327–334, Jan. 2014.

[19] J. F. Raposo, L. G. Sobrinho, and H. G. Ferreira, “A minimal mathematical model of calcium homeostasis,” *J. Clin. Endocrinol. Metab.*, vol. 87, no. 9, pp. 4330–4340, Sep. 2002.

[20] F. Barrère, T. A. Mahmood, K. de Groot, and C. A. van Blitterswijk, “Advanced biomaterials for skeletal tissue regeneration: Instructive and smart functions,” *Mater. Sci. Eng. R Reports*, vol. 59, no. 1–6, pp. 38–71, Feb. 2008.

[21] M. Pawlikowski, M. Klasztorny, and K. Skalski, “Studies on constitutive equation that models bone tissue,” *Acta Bioeng. Biomech. / Wrocław Univ. Technol.*, vol. 10, no. 4, pp. 39–47, Jan. 2008.

[22] B. Helgason, E. Perilli, E. Schileo, F. Taddei, S. Brynjólfsson, and M. Viceconti, “Mathematical relationships between bone density and mechanical properties: a literature review.,” *Clin. Biomech.*, vol. 23, no. 2, pp. 135–146, Feb. 2008.

[23] M. C. and J. K. Y. C. Chao Le Meng Bao, Erin Y. Teo, Mark S.K. Chong, Yuchun Liu, *Regenerative Medicine and Tissue Engineering*. InTech, 2013.

[24] P. X. Ma and J. Elisseeff, *Scaffolding in Tissue Engineering*. CRC Press, 2006.

[25] S. Bandyopadhyay-Ghosh, “Bone as a collagen-hydroxyapatite composite and its repair,” *Trends Biomater. Artif. Organs*, vol. 22, no. 2, pp. 116–124, 2008.

[26] D. Knudson, *Fundamentals of Biomechanics*. Springer, 2007.

[27] U. Meyer, T. Meyer, J. Handschel, and H. P. Wiesmann, *Fundamentals of Tissue Engineering and Regenerative Medicine*. Springer, 2009.

[28] M. A. Meyers, P. Chen, A. Y. Lin, and Y. Seki, “Biological materials: Structure and mechanical properties,” *Prog. Mater. Sci.*, vol. 53, no. 1, pp. 1–206, Jan. 2008.

[29] M. Doblaré, J. M. García-Aznar, and M. J. Gómez-Benito, “Modelling bone tissue fracture and healing: a review,” *Eng. Fract. Mech.*, vol. 71, no. 13–14, pp. 1809–1840, Sep. 2004.

[30] K. Piper and G. Valentine, “Bone pathology.,” *Methods Mol. Biol.*, vol. 915, pp. 51–88, Jan. 2012.

[31] N. Peel, “Bone remodelling and disorders of bone metabolism,” *Surg.*, vol. 27, no. 2, pp. 70–74, Feb. 2009.

[32] J. L. Marsh *et al.*, “Fracture and dislocation classification compendium - 2007: Orthopaedic Trauma Association classification, database and outcomes committee.,” *J. Orthop. Trauma*, vol. 21, no. 10 Suppl, pp. S1–S133, Jan. 2007.

[33] F. Rauch and F. H. Glorieux, “Osteogenesis imperfecta,” *Lancet*, vol. 363, no. 9418, pp. 1377–1385, Apr. 2004.

[34] P. Meunier, *Osteoporosis: diagnosis and management*. London: Taylor & Francis, 1998.

[35] J. A. Eisman, “Osteomalacia,” *Baillieres. Clin. Endocrinol. Metab.*, vol. 2, no. 1, pp. 125–155, Feb. 1988.

[36] P. J. Carek, L. M. Dickerson, and J. L. Sack, “Diagnosis and management of osteomyelitis,” *Am. Fam. Physician*, vol. 63, no. 12, pp. 2413–2420, Jun. 2001.

[37] H. A. Mousa, “Bone infection,” *East. Mediterr. Heal. J.*, vol. 9, no. 1–2, pp. 208–214, Jan. 2003.

[38] J. A. Buckwalter and E. A. Brandser, “Metastatic disease of the skeleton,” *Am. Fam. Physician*, vol. 55, no. 5, pp. 1761–1768, Apr. 1997.

[39] R. Lanza, R. Langer, and J. Vacanti, *Principles of Tissue Engineering*, 3rd ed. Academic Press, 2011.

[40] J. Hollinger, T. A. Einhorn, B. Doll, and C. Sfeir, *Bone Tissue Engineering*. CRC Press, 2004.

[41] D. W. Hutmacher, “Scaffolds in tissue engineering bone and cartilage,” *Biomaterials*, vol. 21, no. 24, pp. 2529–2543, Dec. 2000.

[42] M. J. Lysaght, A. Jaklenec, and E. Deweerd, “Great expectations: private sector activity in tissue engineering, regenerative medicine, and stem cell therapeutics,” *Tissue Eng. Part A*, vol. 14, no. 2, pp. 305–315, Feb. 2008.

[43] G. Lewis, “Regenerative medicine at a global level: current patterns and global trends,” in *The Global Dynamics of Regenerative Medicine: A Social Science Critique*, 1st ed., A. Webster, Ed. Palgrave Macmillan, 2013, p. 248.

[44] A. Greenwald *et al.*, “The evolving role of bone-graft substitutes,” in *American academy of orthopaedic surgeons 77th annual meeting*, 2010, p. 6.

[45] L. Geris, J. Vander Sloten, and H. Van Oosterwyck, “In silico biology of bone modelling and remodelling: regeneration,” *Philos. Trans. A. Math. Phys. Eng. Sci.*, vol. 367, no. 1895, pp. 2031–2053, May 2009.

[46] Global Data, “Bone Graft Substitutes - Global Pipeline Analysis, Competitive Landscape and Market Forecast to 2017,” London, 2011.

[47] iData Research, “U.S Orthopedic Biomaterials Market,” Dallas, 2013.

[48] Medtech Insight/Elsevier Business Intelligence, “European markets for bone graft substitute products for spinal fusion,” Huntington Beach, 2011.

[49] A.-K. Bock, E. Rodríguez-Cerezo, B. Hüsing, B. Bührlen, and M. Nusser, “Human tissue-engineered products: Potential socio-economic impacts of a new European regulatory framework for authorisation, supervision and vigilance. Technical Report EUR 21838 EN,” Sevilla, 2005.

[50] Knowledge Enterprises, *The worldwide orthopedic market – 2005-2006*. Chagrin Falls: Knowledge Enterprises, 2006.

[51] C. A. Kirker-Head, “Potential applications and delivery strategies for bone morphogenetic proteins,” *Adv. Drug Deliv. Rev.*, vol. 43, no. 1, pp. 65–92, Sep. 2000.

[52] L. Grgurevic *et al.*, “Bone morphogenetic protein (BMP)1-3 enhances bone repair,” *Biochem. Biophys. Res. Commun.*, vol. 408, no. 1, pp. 25–31, Apr. 2011.

[53] N. Sykaras and L. a Opperman, “Bone morphogenetic proteins (BMPs): how do they function and what can they offer the clinician?,” *J. Oral Sci.*, vol. 45, no. 2, pp. 57–73, Jun. 2003.

[54] J. W. Lee, K. S. Kang, S. H. Lee, J.-Y. Kim, B.-K. Lee, and D.-W. Cho, “Bone regeneration using a microstereolithography-produced customized poly(propylene

fumarate)/diethyl fumarate photopolymer 3D scaffold incorporating BMP-2 loaded PLGA microspheres," *Biomaterials*, vol. 32, no. 3, pp. 744–752, Jan. 2011.

[55] Z. Chen, D. Li, B. Lu, Y. Tang, M. Sun, and S. Xu, "Fabrication of osteo-structure analogous scaffolds via fused deposition modeling," *Scr. Mater.*, vol. 52, no. 2, pp. 157–161, Jan. 2005.

[56] J.-Y. Lee *et al.*, "Osteoblastic differentiation of human bone marrow stromal cells in self-assembled BMP-2 receptor-binding peptide-amphiphiles," *Biomaterials*, vol. 30, no. 21, pp. 3532–3541, Jul. 2009.

[57] S. C.-N. Chang *et al.*, "Cranial repair using BMP-2 gene engineered bone marrow stromal cells," *J. Surg. Res.*, vol. 119, no. 1, pp. 85–91, Jun. 2004.

[58] Y. Bai *et al.*, "Localized delivery of growth factors for angiogenesis and bone formation in tissue engineering," *Int. Immunopharmacol.*, vol. 16, no. 2, pp. 214–223, Jun. 2013.

[59] V. I. Sikavitsas, J. S. Temenoff, and A. G. Mikos, "Biomaterials and bone mechanotransduction.," *Biomaterials*, vol. 22, no. 19, pp. 2581–2593, Oct. 2001.

[60] M. Bosetti, F. Boccafoschi, M. Leigheb, and M. F. Cannas, "Effect of different growth factors on human osteoblasts activities: a possible application in bone regeneration for tissue engineering," *Biomol. Eng.*, vol. 24, no. 6, pp. 613–618, Dec. 2007.

[61] Y. Ikada, "Challenges in tissue engineering," *Interface*, vol. 3, no. 10, pp. 589–601, 2006.

[62] T. Adachi, Y. Osako, M. Tanaka, M. Hojo, and S. J. Hollister, "Framework for optimal design of porous scaffold microstructure by computational simulation of bone regeneration," *Biomaterials*, vol. 27, no. 21, pp. 3964–3972, 2006.

[63] Y. Chen, S. Zhou, and Q. Li, "Microstructure design of biodegradable scaffold and its effect on tissue regeneration," *Biomaterials*, vol. 32, no. 22, pp. 5003–5014, Aug. 2011.

[64] S. J. Hollister, R. D. Maddox, and J. M. Taboas, "Optimal design and fabrication of scaffolds to mimic tissue properties and satisfy biological constraints," *Biomaterials*, vol. 23, no. 20, pp. 4095–4103, Oct. 2002.

[65] S. J. Hollister, "Porous scaffold design for tissue engineering," *Nat. Mater.*, vol. 4, no. 7, pp. 518–524, 2005.

[66] M. Schieker, H. Seitz, I. Drosse, S. Seitz, and W. Mutschler, "Biomaterials as Scaffold for Bone Tissue Engineering," *Eur. J. Trauma*, vol. 32, no. 2, pp. 114–124,

Apr. 2006.

[67] A. W. Lloyd, “Interfacial bioengineering to enhance surface biocompatibility.,” *Med. Device Technol.*, vol. 13, no. 1, pp. 18–21, 2002.

[68] D. P. Byrne, D. Lacroix, J. A. Planell, D. J. Kelly, and P. J. Prendergast, “Simulation of tissue differentiation in a scaffold as a function of porosity, Young’s modulus and dissolution rate: Application of mechanobiological models in tissue engineering,” *Biomaterials*, vol. 28, no. 36, pp. 5544–5554, 2007.

[69] A. Kolk *et al.*, “Current trends and future perspectives of bone substitute materials - from space holders to innovative biomaterials,” *J. Craniomaxillofac. Surg.*, vol. 40, no. 8, pp. 706–718, Dec. 2012.

[70] S. Rajagopalan and R. Robb, “Schwarz meets Schwann: design and fabrication of biomorphic and durataxic tissue engineering scaffolds,” *Med. Image Anal.*, vol. 10, pp. 693–712, 2006.

[71] M. Vert, “Polymeric biomaterials: Strategies of the past vs. strategies of the future,” *Prog. Polym. Sci.*, vol. 32, no. 8–9, pp. 755–761, Aug. 2007.

[72] S. M. Giannitelli, D. Accoto, M. Trombetta, and A. Rainer, “Current trends in the design of scaffolds for computer-aided tissue engineering,” *Acta Biomater.*, vol. 10, no. 2, pp. 580–594, Feb. 2014.

[73] C. Estrada, A. C. Paz, and L. E. López, “Ingeniería de tejido óseo : consideraciones básicas,” *Rev. EIA*, no. 5, pp. 93–100, 2006.

[74] S. Bose, M. Roy, and A. Bandyopadhyay, “Recent advances in bone tissue engineering scaffolds,” *Trends Biotechnol.*, vol. 30, no. 10, pp. 546–554, Oct. 2012.

[75] F. Edalat, H. Bae, S. Manoucheri, J. M. Cha, and A. Khademhosseini, “Engineering approaches toward deconstructing and controlling the stem cell environment,” *Ann. Biomed. Eng.*, vol. 40, no. 6, pp. 1301–1315, Jun. 2012.

[76] V. Karageorgiou and D. Kaplan, “Porosity of 3D biomaterial scaffolds and osteogenesis,” *Biomaterials*, vol. 26, pp. 5474–5491, 2005.

[77] Y. Kuboki *et al.*, “BMP-induced osteogenesis on the surface of hydroxyapatite with geometrically feasible and nonfeasible structures: topology of osteogenesis,” *J. Biomed. Mater. Res.*, vol. 39, no. 2, pp. 190–199, Feb. 1998.

[78] M. Fröhlich, W. L. Grayson, L. Q. Wan, D. Marolt, M. Drobnic, and G. Vunjak-Novakovic, “Tissue engineered bone grafts: biological requirements, tissue culture and clinical relevance,” *Curr. Stem Cell Res. Ther.*, vol. 3, no. 4, pp. 254–264, Dec. 2008.

[79] S. F. Hulbert, F. A. Young, R. S. Mathews, J. J. Klawitter, C. D. Talbert, and F. H. Stelling, “Potential of ceramic materials as permanently implantable skeletal prostheses,” *J. Biomed. Mater. Res.*, vol. 4, no. 3, pp. 433–456, Sep. 1970.

[80] K. Whang *et al.*, “Engineering Bone Regeneration with Bioabsorbable Scaffolds with Novel Microarchitecture,” *Tissue Eng.*, vol. 5, no. 1, pp. 35–51, 1999.

[81] C. N. Cornell, “Osteoconductive materials and their role as substitutes for autogenous bone grafts,” *Orthop. Clin. North Am.*, vol. 30, no. 4, pp. 591–598, 1999.

[82] S. J. Hollister *et al.*, “Engineering craniofacial scaffolds,” *Orthod. Craniofac. Res.*, vol. 8, no. 3, pp. 162–173, Aug. 2005.

[83] M. Bohner, Y. Loosli, G. Baroud, and D. Lacroix, “Commentary: Deciphering the link between architecture and biological response of a bone graft substitute,” *Acta Biomater.*, vol. 7, no. 2, pp. 478–484, Feb. 2011.

[84] S. Bose, S. Vahabzadeh, and A. Bandyopadhyay, “Bone tissue engineering using 3D printing,” *Mater. Today*, vol. 16, no. 12, pp. 496–504, Dec. 2013.

[85] X. Li, D. Li, B. Lu, L. Wang, and Z. Wang, “Fabrication and evaluation of calcium phosphate cement scaffold with controlled internal channel architecture and complex shape,” *Proc. Inst. Mech. Eng. Part H J. Eng. Med.*, vol. 221, no. 8, pp. 951–958, Jan. 2007.

[86] L. Liulan, H. Qingxi, H. Xianxu, and X. Gaochun, “Design and Fabrication of Bone Tissue Engineering Scaffolds via Rapid Prototyping and CAD,” *J. Rare Earths*, vol. 25, pp. 379–383, Jun. 2007.

[87] J. Guo, Q. X. Hu, Y. Yao, Q. Lu, Y. W. Yu, and Y. Qian, “A Pore Network Model Based Method for Tissue Engineering Scaffold Design,” *2010 Int. Conf. Biomed. Eng. Comput. Sci.*, pp. 1–4, Apr. 2010.

[88] Q. Lian, D. Li, Y. Tang, and Y. Zhang, “Computer modeling approach for a novel internal architecture of artificial bone,” *Comput. Des.*, vol. 38, no. 5, pp. 507–514, May 2006.

[89] L. Jongpaiboonkit, J. W. Halloran, and S. J. Hollister, “Internal Structure Evaluation of Three-Dimensional Calcium Phosphate Bone Scaffolds: A Micro-Computed Tomographic Study,” *J. Am. Ceram. Soc.*, vol. 89, no. 10, pp. 3176–3181, Oct. 2006.

[90] A. Armillotta and R. Pelzer, “Modeling of porous structures for rapid prototyping of tissue engineering scaffolds,” *Int. J. Adv. Manuf. Technol.*, vol. 39, no. 5–6, pp.

501–511, Oct. 2007.

[91] Z. Chen, X. Feng, and Z. Jiang, “Structural design and optimization of interior scaffolds in artificial bone,” in *2007 1st International Conference on Bioinformatics and Biomedical Engineering, ICBBE*, 2007, no. 1, pp. 330–333.

[92] C. M. Cheah, C. K. Chua, K. F. Leong, and S. W. Chua, “Development of a Tissue Engineering Scaffold Structure Library for Rapid Prototyping. Part 1: Investigation and Classification,” *Int. J. Adv. Manuf. Technol.*, vol. 21, no. 4, pp. 291–301, Feb. 2003.

[93] A. L. Olivares, E. Marsal, J. A. Planell, and D. Lacroix, “Finite element study of scaffold architecture design and culture conditions for tissue engineering,” *Biomaterials*, vol. 30, no. 30, pp. 6142–6149, 2009.

[94] F. P. W. Melchels, A. M. C. Barradas, C. A. van Blitterswijk, J. de Boer, J. Feijen, and D. W. Grijpma, “Effects of the architecture of tissue engineering scaffolds on cell seeding and culturing,” *Acta Biomater.*, vol. 6, no. 11, pp. 4208–4217, Nov. 2010.

[95] F. P. W. Melchels, K. Bertoldi, R. Gabbrielli, A. H. Velders, J. Feijen, and D. W. Grijpma, “Mathematically defined tissue engineering scaffold architectures prepared by stereolithography,” *Biomaterials*, vol. 31, no. 27, pp. 6909–6916, Sep. 2010.

[96] S. C. Kapfer, S. T. Hyde, K. Mecke, C. H. Arns, and G. E. Schröder-Turk, “Minimal surface scaffold designs for tissue engineering,” *Biomaterials*, vol. 32, no. 29, pp. 6875–6782, Oct. 2011.

[97] D. Yoo, “New paradigms in internal architecture design and freeform fabrication of tissue engineering porous scaffolds,” *Med. Eng. Phys.*, vol. 34, no. 6, pp. 762–776, Jul. 2012.

[98] A. Pasko, O. Fryazinov, T. Vilbrandt, P.-A. Fayolle, and V. Adzhiev, “Procedural Function-based Modelling of Volumetric Microstructures,” *Graph. Models*, vol. 73, no. 5, pp. 165–181, 2011.

[99] P. Pandithevan and G. S. Kumar, “Personalised bone tissue engineering scaffold with controlled architecture using fractal tool paths in layered manufacturing,” *Virtual Phys. Prototyp.*, vol. 4, no. 3, pp. 165–180, 2009.

[100] W. Sun, B. Starly, J. Nam, and A. Darling, “Bio-CAD modeling and its applications in computer-aided tissue engineering,” *Comput. Des.*, vol. 37, pp. 1097–1114, 2005.

[101] B. S. Bucklen, W. A. Wettergreen, E. Yuksel, and M. A. K. Liebschner, “Bone-derived CAD library for assembly of scaffolds in computer-aided tissue engineering,” *Virtual Phys. Prototyp.*, vol. 3, no. 1, pp. 13–23, Mar. 2008.

[102] G. H. van Lenthe, H. Hagenmüller, M. Bohner, S. J. Hollister, L. Meinel, and R. Müller, “Nondestructive micro-computed tomography for biological imaging and quantification of scaffold-bone interaction in vivo,” *Biomaterials*, vol. 28, no. 15, pp. 2479–2490, May 2007.

[103] Z. Hu *et al.*, “On Modeling Bio-Scaffolds: Structural and Fluid Transport Characterization Based on 3-D Imaging Data,” *Tsinghua Sci. Technol.*, vol. 14, no. Supplement 1, pp. 20–23, Jun. 2009.

[104] X. Y. Kou and S. T. Tan, “A simple and effective geometric representation for irregular porous structure modeling,” *Comput. Des.*, vol. 42, no. 10, pp. 930–941, Oct. 2010.

[105] Z. Fang, B. Starly, and W. Sun, “Computer-aided characterization for effective mechanical properties of porous tissue scaffolds,” *Comput. Des.*, vol. 37, pp. 65–72, 2005.

[106] R. J. Shipley *et al.*, “Design criteria for a printed tissue engineering construct: a mathematical homogenization approach.,” *J. Theor. Biol.*, vol. 259, no. 3, pp. 489–502, Aug. 2009.

[107] S. Cowin, “Remarks on optimization and the prediction of bone adaptation to altered loading,” *New York Cent. Biomed. Eng. …*, pp. 1–4, 2003.

[108] C. Yu, N. Kikuchi, and S. J. Hollister, “A novel method for biomaterial scaffold internal architecture design to match bone elastic properties with desired porosity,” *Methods*, vol. 37, pp. 623–636, 2004.

[109] S. J. Hollister and C. Lin, “Computational design of tissue engineering scaffolds,” *Comput. Methods Appl. Mech. Eng.*, vol. 196, pp. 2991–2998, 2007.

[110] H. de Amorim Almeida and P. J. da Silva Bártolo, “Virtual topological optimisation of scaffolds for rapid prototyping,” *Med. Eng. Phys.*, vol. 32, no. 7, pp. 775–782, Sep. 2010.

[111] M. Vert *et al.*, “Terminology for biorelated polymers and applications (IUPAC Recommendations 2012),” *Pure Appl. Chem.*, vol. 84, no. 2, pp. 377–410, Jan. 2012.

[112] D. F. Williams, “On the nature of biomaterials,” *Biomaterials*, vol. 30, no. 30, pp. 5897–5909, Oct. 2009.

[113] M. Stevens, “Biomaterials for bone tissue engineering,” *Mater. Today*, vol. 11, no. 5, pp. 18–25, May 2008.

[114] A. S. AlGhamdi, O. Shibly, and S. G. Ciancio, “Osseous grafting part II: xenografts and alloplasts for periodontal regeneration-a literature review,” *J. Int. Acad. Periodontol.*, vol. 12, no. 2, pp. 39–44, May 2010.

[115] A. Oryan, S. Alidadi, A. Moshiri, and N. Maffulli, “Bone regenerative medicine: classic options, novel strategies, and future directions,” *J. Orthop. Surg. Res.*, vol. 9, no. 1, p. 18, Jan. 2014.

[116] C. Verwilghen, M. Chkir, S. Rio, A. Nzihou, P. Sharrock, and G. Depelsenaire, “Convenient conversion of calcium carbonate to hydroxyapatite at ambient pressure,” *Mater. Sci. Eng. C*, vol. 29, no. 3, pp. 771–773, Apr. 2009.

[117] T. Guda, M. Appleford, S. Oh, and J. L. Ong, “A cellular perspective to bioceramic scaffolds for bone tissue engineering: the state of the art,” *Curr. Top. Med. Chem.*, vol. 8, no. 4, pp. 290–299, Jan. 2008.

[118] R. Z. LeGeros, “Properties of osteoconductive biomaterials: calcium phosphates,” *Clin. Orthop. Relat. Res.*, no. 395, pp. 81–98, Mar. 2002.

[119] S. Samavedi, A. R. Whittington, and A. S. Goldstein, “Calcium phosphate ceramics in bone tissue engineering: a review of properties and their influence on cell behavior,” *Acta Biomater.*, vol. 9, no. 9, pp. 8037–8045, Sep. 2013.

[120] J. R. Porter, T. T. Ruckh, and K. C. Popat, “Bone tissue engineering: a review in bone biomimetics and drug delivery strategies,” *Biotechnol. Prog.*, vol. 25, no. 6, pp. 1539–1560, 2009.

[121] L. Tzvetanov, S. Nikolaeva, I. Michailov, and P. Tivchev, “Bone and ceramic interaction in the bone union process,” *Ultrastruct. Pathol.*, vol. 26, no. 3, pp. 171–175, 2002.

[122] A. Ravaglioli, A. Krajewski, G. Baldi, F. Tateo, L. Peruzzo, and A. Piancastelli, “Glass–ceramic scaffolds for tissue engineering,” *Adv. Appl. Ceram.*, vol. 107, no. 5, pp. 268–273, Oct. 2008.

[123] L. L. Hench, N. Roki, and M. B. Fenn, “Bioactive glasses: Importance of structure and properties in bone regeneration,” *J. Mol. Struct.*, pp. 1–7, Apr. 2014.

[124] J. R. Jones, “Review of bioactive glass: from Hench to hybrids,” *Acta Biomater.*, vol. 9, no. 1, pp. 4457–4486, Jan. 2013.

[125] K. Madhavan Nampoothiri, N. R. Nair, and R. P. John, “An overview of the recent developments in polylactide (PLA) research.,” *Bioresour. Technol.*, vol. 101, no. 22,

pp. 8493–501, Nov. 2010.

[126] a Göpferich, “Mechanisms of polymer degradation and erosion.,” *Biomaterials*, vol. 17, no. 2, pp. 103–14, Jan. 1996.

[127] Y. Wang, J. Pan, X. Han, C. Sinka, and L. Ding, “A phenomenological model for the degradation of biodegradable polymers.,” *Biomaterials*, vol. 29, no. 23, pp. 3393–401, Aug. 2008.

[128] Y. Chen, S. Zhou, and Q. Li, “Mathematical modeling of degradation for bulk-erosive polymers: Applications in tissue engineering scaffolds and drug delivery systems,” *Acta Biomater.*, vol. 7, no. 3, pp. 1140–1149, 2011.

[129] Y. Kang *et al.*, “A comparative study of the in vitro degradation of poly(l-lactic acid)/B-tricalcium phosphate scaffold in static and dynamic simulated body fluid,” *Eur. Polym. J.*, vol. 43, no. 5, pp. 1768–1778, May 2007.

[130] Q. Chen, C. Zhu, and G. a Thouas, “Progress and challenges in biomaterials used for bone tissue engineering: bioactive glasses and elastomeric composites,” *Prog. Biomater.*, vol. 1, no. 1, p. 22, 2012.

[131] J. L. Brown, S. G. Kumbar, and C. T. Laurencin, “Bone Tissue Engineering,” in *Biomaterials Science*, B. Ratner, A. S. Hoffman, F. J. Schoen, and J. E. Lemons, Eds. Oxford: Elsevier, 2013, pp. 1194–1214.

[132] M. P. Ginebra, T. Traykova, and J. A. Planell, “Calcium phosphate cements as bone drug delivery systems: A review,” *J. Control. Release*, vol. 113, pp. 102–110, 2006.

[133] M. Ginebra, F. Gil, and J. Planell, “Acrylic Bone Cements,” in *Integrated Biomaterials Science*, 1st ed., R. Barbucci, Ed. Kluwer Academy / Plenum Publisher, 2002, pp. 569–588.

[134] S. M. Kenny and M. Buggy, “Bone cements and fillers: A review,” *J. Mater. Sci.*, vol. 14, pp. 923–938, 2003.

[135] C. K. Chua, K. F. Leong, C. M. Cheah, and S. W. Chua, “Development of a Tissue Engineering Scaffold Structure Library for Rapid Prototyping . Part 2 : Parametric Library and Assembly Program,” *Adv. Manuf. Technol.*, vol. 21, pp. 302–312, 2003.

[136] N. Yang and K. Zhou, “Effective method for multi-scale gradient porous scaffold design and fabrication,” *Mater. Sci. Eng. C. Mater. Biol. Appl.*, vol. 43, pp. 502–505, Oct. 2014.

[137] A. Sutradhar and G. Paulino, “Topological optimization for designing patient-specific large craniofacial segmental bone replacements,” *Proc. Natl. Acad. Sci.*,

vol. 107, no. 30, pp. 13222–13227, 2010.

[138] P. Gonçalves Coelho, P. Rui Fernandes, and H. Carriço Rodrigues, “Multiscale modeling of bone tissue with surface and permeability control,” *J. Biomech.*, vol. 44, no. 2, pp. 321–329, Jan. 2011.

[139] P. G. Coelho, S. J. Hollister, C. L. Flanagan, and P. R. Fernandes, “Bioresorbable scaffolds for bone tissue engineering: optimal design, fabrication, mechanical testing and scale-size effects analysis,” *Med. Eng. Phys.*, vol. 37, no. 3, pp. 287–296, Mar. 2015.

[140] M. R. Dias, J. M. Guedes, C. L. Flanagan, S. J. Hollister, and P. R. Fernandes, “Optimization of scaffold design for bone tissue engineering: A computational and experimental study,” *Med. Eng. Phys.*, vol. 36, no. 4, pp. 448–457, Apr. 2014.

[141] J. Woo Jung *et al.*, “Evaluation of the effective diffusivity of a freeform fabricated scaffold using computational simulation,” *J. Biomech. Eng.*, vol. 135, no. 8, p. 7, Aug. 2013.

[142] C. Provin, K. Takano, Y. Sakai, T. Fujii, and R. Shirakashi, “A method for the design of 3D scaffolds for high-density cell attachment and determination of optimum perfusion culture conditions,” *J. Biomech.*, vol. 41, no. 7, pp. 1436–1449, 2008.

[143] B. Starly and W. Sun, “Internal Scaffold Architecture Designs using Lindenmayer Systems,” *Comput. Aided. Des. Appl.*, vol. 4, no. 1–4, pp. 395–403, Jan. 2007.

[144] M. Bashoor-Zadeh, G. Baroud, and M. Bohner, “Geometric analysis of porous bone substitutes using micro-computed tomography and fuzzy distance transform,” *Acta Biomater.*, vol. 6, no. 3, pp. 864–875, Mar. 2010.

[145] L. Podshivalov, C. M. Gomes, A. Zocca, J. Guenster, P. Bar-Yoseph, and A. Fischer, “Design, Analysis and Additive Manufacturing of Porous Structures for Biocompatible Micro-Scale Scaffolds,” *Procedia CIRP*, vol. 5, pp. 247–252, Jan. 2013.

[146] S. J. Hollister, R. A. Levy, T.-M. Chu, J. W. Halloran, and S. E. Feinberg, “An image-based approach for designing and manufacturing craniofacial scaffolds,” *Int. J. Oral Maxillofac. Surg.*, vol. 29, no. 1, pp. 67–71, Feb. 2000.

[147] A. P. Sughanthy, M. N. M. N. M. Ansari, A. P. S. Siva, and M. N. M. N. M. Ansari, “A Review on Bone Scaffold Fabrication Methods,” *Int. Res. J. Eng. Technol.*, vol. 2, no. 6, pp. 1232–1238, 2015.

[148] M. Mullender, a J. El Haj, Y. Yang, M. a van Duin, E. H. Burger, and J. Klein-

Nulend, “Mechanotransduction of bone cells in vitro: mechanobiology of bone tissue,” *Med. Biol. Eng. Comput.*, vol. 42, no. 1, pp. 14–21, Jan. 2004.

[149] T. Adachi *et al.*, “Osteocyte calcium signaling response to bone matrix deformation,” *J. Biomech.*, vol. 42, no. 15, pp. 2507–2512, 2009.

[150] M. Alkhader and M. Vural, “Mechanical response of cellular solids: Role of cellular topology and microstructural irregularity,” *Int. J. Eng. Sci.*, vol. 46, no. 10, pp. 1035–1051, Oct. 2008.

[151] B. G. Sengers, M. Taylor, C. P. Please, and R. O. C. Oreffo, “Computational modelling of cell spreading and tissue regeneration in porous scaffolds,” *Biomaterials*, vol. 28, no. 10, pp. 1926–1940, Apr. 2007.

[152] J. Petrasch, F. Meier, H. Friess, and A. Steinfeld, “Tomography based determination of permeability, Dupuit–Forchheimer coefficient, and interfacial heat transfer coefficient in reticulate porous ceramics,” *Int. J. Heat Fluid Flow*, vol. 29, no. 1, pp. 315–326, Feb. 2008.

[153] A. Okabe, B. Boots, K. Sugihara, S. N. Chiu, and D. G. Kendall, “Chapter 6. Spatial Interpolation,” in *Spatial Tessellations: Concepts and Applications of Voronoi Diagrams*, 2nd ed., Hoboken, NJ, USA: John Wiley & Sons, Inc., 2000.

[154] X. Y. Kou and S. T. Tan, “A simple and effective geometric representation for irregular porous structure modeling,” *Comput. Des.*, vol. 42, no. 10, pp. 930–941, Oct. 2010.

[155] T. Leppänen, M. Karttunen, and K. Kaski, “A new dimension to Turing patterns,” *Phys. D*, vol. 169, pp. 35–44, 2002.

[156] H. Shoji, K. Yamada, D. Ueyama, and T. Ohta, “Turing patterns in three dimensions,” *Phys. Rev. E*, pp. 1–13, 2007.

[157] B. Grzybowski, K. Bishop, and C. Campbell, “Micro- and nanotechnology via reaction – diffusion,” *Soft Matter*, vol. 1, pp. 114–128, 2005.

[158] A. M. Turing, “The chemical basis of morphogenesis,” *Philos. Trans. R. Soc.*, vol. 237, pp. 37–72, 1957.

[159] A. N. Zaikin and A. M. Zhabotinsky, “Concentration wave propagation in two-dimensional liquid-phase self-oscillating system.,” *Nature*, vol. 225, no. 5232, pp. 535–7, Feb. 1970.

[160] G. Turk, “Generating textures on arbitrary surfaces using reaction-diffusion,” *ACM SIGGRAPH Comput. Graph.*, vol. 25, no. 4, pp. 289–298, Jul. 1991.

[161] S. Kondo, “The reaction-diffusion system: a mechanism for autonomous,” *Genes to*

Cells, pp. 535–541, 2002.

[162] V. Volpert and S. Petrovskii, “Reaction-diffusion waves in biology,” *Phys. Life Rev.*, vol. 6, no. 4, pp. 267–310, Oct. 2009.

[163] B. N. Nagorcka, “Evidence for a reaction-diffusion system as a mechanism controlling mammalian hair growth,” *Biosystems*, vol. 16, pp. 323–332, 1983.

[164] G. Rajagopalan, “Diffusion and reaction of epoxy and amine in polysulfone-transport modeling and experimental validation,” *Polymer (Guildf).*, vol. 41, no. 24, pp. 8543–8556, Nov. 2000.

[165] J. D. Murray, *Mathematical Biology I*. Springer, 2001.

[166] H. Meinhardt, *Models of biological pattern formation*, vol. 6. Academic Press London, 1982.

[167] D. Garzón-Alvarado, J. M. García-Aznar, and M. Doblaré, “Appearance and location of secondary ossification centres may be explained by a reaction-diffusion mechanism,” *Comput. Biol. Med.*, vol. 39, no. 6, pp. 554–61, Jun. 2009.

[168] Z. Tabor, E. Rokita, and T. Cichocki, “Origin of the pattern of trabecular bone: An experiment and a model,” *Phys. Rev. E*, vol. 66, no. 5, p. 51906, Nov. 2002.

[169] K. Tezuka, Y. Wada, A. Takahashi, and M. Kikuchi, “Computer-simulated bone architecture in a simple bone-remodeling model based on a reaction-diffusion system,” *J. Bone Miner. Metab.*, vol. 23, no. 1, pp. 1–7, Jan. 2005.

[170] B. Courtin, a M. Perault-Staub, and J. F. Staub, “Spatio-temporal self-organization of bone mineral metabolism and trabecular structure of primary bone.,” *Acta Biotheor.*, vol. 43, no. 4, pp. 373–86, Dec. 1995.

[171] R. Chaturvedi *et al.*, “On multiscale approaches to three-dimensional modelling of morphogenesis.,” *J. R. Soc. Interface*, vol. 2, no. 3, pp. 237–53, Jun. 2005.

[172] T. K. Callahan and E. Knobloch, “Pattern formation in three-dimensional reaction-diffusion systems,” *Phys. D Nonlinear Phenom.*, vol. 132, pp. 339–362, 1999.

[173] H. Shoji and K. Yamada, “Most stable patterns among three-dimensional Turing patterns,” *Jpn. J. Ind. Appl. Math.*, vol. 24, no. 1, pp. 67–77, Feb. 2007.

[174] J. Maselko, “Self-organization as a new method for synthesizing smart and structured materials,” *Mater. Sci. Eng. C*, vol. 4, no. 3, pp. 199–204, 1996.

[175] Y. Suetsugu, D. Walsh, J. Tanaka, and S. Mann, “Hydroxyapatite pattern formation in PVA gels,” *J. Mater. Sci.*, vol. 44, no. 21, pp. 5806–5814, Aug. 2009.

[176] K. Furuichi, Y. Oaki, H. Ichimiya, J. Komotori, and H. Imai, “Preparation of hierarchically organized calcium phosphate – organic polymer composites by

calcification of hydrogel," *Sci. Technol. Adv. Mater.*, vol. 219, 2006.

[177] B. Grzybowski, *Chemistry in motion: reaction-diffusion systems for micro-and nanotechnology*. Wiley Online Library, 2009.

[178] F. Cui, Y. Li, and J. Ge, "Self-assembly of mineralized collagen composites," *Mater. Sci.*, vol. 57, pp. 1–27, 2007.

[179] Q. Li, C. Zheng, and N. Wang, "Spiral waves in LIMA model and its LBGK simulation," *Commun. Nonlinear Sci. Numer. Simul.*, vol. 6, pp. 68–73, 2001.

[180] S. Ristori, F. Rossi, G. Biosa, N. Marchettini, M. Rustici, and E. Tiezzi, "Interplay between the Belousov-Zhabotinsky reaction-diffusion system and biomimetic matrices," *Chem. Phys. Lett.*, vol. 436, pp. 175–178, 2007.

[181] K. M. Page, P. K. Maini, and N. A. M. Monk, "Complex pattern formation in reaction-diffusion systems with spatially varying parameters," *Phys. D Nonlinear Phenom.*, vol. 202, pp. 95–115, 2005.

[182] A. Madzvamuse, R. Thomas, P. K. Maini, and A. Wathen, "A numerical approach to the study of spatial pattern formation in the ligaments of arcoidbivalves.," *Bull. Math. Biol.*, vol. 64(3), pp. 501–530, 2002.

[183] E. Perilli, M. Baleani, W. Raatjes, F. Baruffaldi, A. Cappello, and A. Toni, "Compressive properties of trabecular bone related to microct evaluated morphometric parameters: preliminary results," *J. Mech. Med. Biol.*, vol. 5, pp. 349–355, Nov. 2011.

[184] A. Boccaccio, L. Lamberti, C. Pappalettere, and L. Quagliarella, "Accuracy of finite element predictions on bone/implant interface contact pressures for models reconstructed from CT scans," *J. Mech. Med. Biol.*, vol. 8, pp. 161–182, 2008.

[185] R. Singh *et al.*, "Characterization of the deformation behavior of intermediate porosity interconnected Ti foams using micro-computed tomography and direct finite element modeling," *Acta Biomater.*, vol. 6, no. 6, pp. 2342–2351, Jun. 2010.

[186] P. K. Maini and H. G. Othmer, *Mathematical models in morphogenesis*. Springer, 1999.

[187] B. Courtin, A. M. Perault-Staub, and J. F. Staub, "Spatio-temporal self-organization of bone mineral metabolism and trabecular structure of primary bone," *Acta Biotheor.*, vol. 43, no. 4, pp. 373–386, 1995.

[188] M. Zhang, S. M. June, T. E. Long, and J. Kong, *Principles of Step-Growth Polymerization (Polycondensation and Polyaddition)*. 2016.

[189] A. Madzvamuse, "A numerical approach to the study of spatial pattern formation,"

phdthesis, University of Oxford, 2000.

[190] E. Javierre, P. Moreo, M. Doblaré, and J. M. García-Aznar, “Numerical modeling of a mechano-chemical theory for wound contraction analysis,” *Int. J. Solids Struct.*, vol. 46, no. 20, pp. 3597–3606, Oct. 2009.

[191] T. Leppänen, “Computational Studies of Pattern Formation in Turing Systems,” 2004.

[192] Kasios, *Duowedge. Catalogo del fabricante*. Kasios, 2008.

[193] R. Kapral, “Pattern formation in chemical systems,” *Science (80-.).*, vol. 86, pp. 149–157, 1995.

[194] T. Leppänen, M. Karttunen, R. Barrio, and K. Kaski, “Turing Systems as Models of Complex Pattern Formation,” *Brazilian J. Phys.*, vol. 34, no. 2, pp. 368–372, 2003.

[195] D. Rekow, P. Van Thompson, and J. Ricci, “Influence of scaffold meso-scale features on bone tissue response,” *J. Mater. Sci.*, no. July, pp. 5113–5121, 2006.

[196] A. M. Turing, “The chemical basis of morphogensis,” *Phil. Trans. R. Soc*, vol. 327, pp. 37–72, 1952.

[197] S. Yang, K. F. Leong, Z. Du, and C. K. Chua, “The design of scaffolds for use in tissue engineering. Part I. Traditional factors,” *Tissue Eng.*, vol. 7, no. 6, pp. 679–689, Dec. 2001.

[198] S. Yang, K.-F. Leong, Z. Du, and C.-K. Chua, “The design of scaffolds for use in tissue engineering. Part II. Rapid prototyping techniques.,” *Tissue Eng.*, vol. 8, no. 1, pp. 1–11, Feb. 2002.

[199] M. H. Too *et al.*, “Investigation of 3D Non-Random Porous Structures by Fused Deposition Modelling,” *Int. J. Adv. Manuf. Technol.*, vol. 19, no. 3, pp. 217–223, Feb. 2002.

[200] I. Zein, D. W. Hutmacher, K. C. Tan, and S. H. Teoh, “Fused deposition modeling of novel scaffold architectures for tissue engineering applications.,” *Biomaterials*, vol. 23, no. 4, pp. 1169–85, Feb. 2002.

[201] B. C. Tellis, J. A. Szivek, C. L. Bliss, D. S. Margolis, R. K. Vaidyanathan, and P. Calvert, “Trabecular scaffolds created using micro CT guided fused deposition modeling,” *Mater. Sci. Eng. C*, vol. 28, no. 1, pp. 171–178, Jan. 2008.

[202] H. S. Ramanath, M. Chandrasekaran, C. K. Chua, K. F. Leong, and K. D. Shah, “Modelling of Extrusion Behaviour of Biopolymer and Composites in Fused Deposition Modelling,” in *Key Engineering Materials*, 2007, vol. 334–335, pp. 1241–1244.

[203] C. K. Chua, K. F. Leong, C. M. Cheah, and S. W. Chua, “Development of a Tissue Engineering Scaffold Structure Library for Rapid Prototyping . Part 1 : Investigation and Classification,” *Tissue Eng.*, pp. 291–301, 2003.

[204] M. W. Naing, C. K. Chua, K. F. Leong, and Y. Wang, “Fabrication of customised scaffolds using computer-aided design and rapid prototyping techniques,” *Rapid Prototyp. J.*, vol. 11, no. 4, pp. 249–259, Jan. 2005.

[205] G. V. Salmoria, P. Klauss, R. A. Paggi, L. A. Kanis, and A. Lago, “Structure and mechanical properties of cellulose based scaffolds fabricated by selective laser sintering,” *Polym. Test.*, vol. 28, no. 6, pp. 648–652, Sep. 2009.

[206] L. Hao, S. Dadbakhsh, O. Seaman, and M. Felstead, “Selective laser melting of a stainless steel and hydroxyapatite composite for load-bearing implant development,” *J. Mater. Process. Technol.*, vol. 209, no. 17, pp. 5793–5801, Aug. 2009.

[207] S. Eosoly, D. Brabazon, S. Lohfeld, and L. Looney, “Selective laser sintering of hydroxyapatite/poly-epsilon-caprolactone scaffolds.,” *Acta Biomater.*, vol. 6, no. 7, pp. 2511–7, Jul. 2010.

[208] W. Yeong, C. Chua, K. Leong, M. Chandrasekaran, and M. Lee, “Indirect fabrication of collagen scaffold based on inkjet printing technique,” *Rapid Prototyp. J.*, vol. 12, no. 4, pp. 229–237, Aug. 2006.

[209] B. Utela, D. Storti, R. Anderson, and M. Ganter, “A review of process development steps for new material systems in three dimensional printing (3DP),” *J. Manuf. Process.*, vol. 10, no. 2, pp. 96–104, Jul. 2008.

[210] J. Y. Tan, C. K. Chua, and K. F. Leong, “Indirect fabrication of gelatin scaffolds using rapid prototyping technology,” *Virtual Phys. Prototyp.*, vol. 5, no. 1, pp. 45–53, Mar. 2010.

[211] A. Butscher, M. Bohner, S. Hofmann, L. Gauckler, and R. Müller, “Structural and material approaches to bone tissue engineering in powder-based three-dimensional printing,” *Acta Biomater.*, vol. 7, no. 3, pp. 907–920, Mar. 2011.

[212] S. V Dorozhkin, “Amorphous calcium (ortho)phosphates,” *Acta Biomater.*, vol. 6, no. 12, pp. 4457–4475, Dec. 2010.

[213] L. S. Nair and C. T. Laurencin, “Biodegradable polymers as biomaterials,” *Prog. Polym. Sci.*, vol. 32, no. 8–9, pp. 762–798, Aug. 2007.

[214] K. Rezwan, Q. Z. Chen, J. J. Blaker, and A. R. Boccaccini, “Biodegradable and bioactive porous polymer/inorganic composite scaffolds for bone tissue

engineering," *Biomaterials*, vol. 27, no. 18, pp. 3413–3431, Jun. 2006.

[215] M. Okada, "Chemical syntheses of biodegradable polymers," *Prog. Polym. Sci.*, vol. 27, no. 1, pp. 87–133, Feb. 2002.

[216] A. Göpferich, "Polymer Bulk Erosion," *Macromolecules*, vol. 30, no. 9, pp. 2598–2604, May 1997.

[217] E. J. Frazza and E. E. Schmitt, "A new absorbable suture," *J. Biomed. Mater. Res.*, vol. 5, no. 2, pp. 43–58, Jan. 1971.

[218] P. B. Maurus and C. C. Kaeding, "Bioabsorbable implant material review," *Oper. Tech. Sports Med.*, vol. 12, no. 3, pp. 158–160, Jul. 2004.

[219] G. Chen, H. Kim, E. Kim, and J. Yoon, "Synthesis of high-molecular-weight poly (L -lactic acid) through the direct condensation polymerization of L-lactic acid in bulk state," *Eur. Polym. J.*, vol. 42, pp. 468–472, 2006.

[220] M. S. Lopes, A. . Jardini, and R. M. Filho, "Poly (Lactic Acid) Production for Tissue Engineering Applications," *Procedia Eng.*, vol. 42, no. August, pp. 1402–1413, Jan. 2012.

[221] G. Perego, G. D. Cella, and C. Bastioli, "Effect of molecular weight and crystallinity on poly(lactic acid) mechanical properties," *J. Appl. Polym. Sci.*, vol. 59, no. 1, pp. 37–43, Jan. 1996.

[222] J. E. Bergsma, F. R. Rozema, R. R. Bos, G. Boering, W. C. de Bruijn, and A. J. Pennings, "In vivo degradation and biocompatibility study of in vitro pre-degraded as-polymerized polyactide particles," *Biomaterials*, vol. 16, no. 4, pp. 267–274, Mar. 1995.

[223] S. Jacobsen and H. G. Fritz, "Plasticizing polylactide - the effect of different plasticizers on the mechanical properties," *Polym. Eng. Sci.*, vol. 39, no. 7, pp. 1303–1310, Jul. 1999.

[224] P. Gunatillake, R. Mayadunne, and R. Adhikari, "Recent developments in biodegradable synthetic polymers," *Biotechnol. Annu. Rev.*, vol. 12, pp. 301–347, Jan. 2006.

[225] H. Chim *et al.*, "A comparative analysis of scaffold material modifications for load-bearing applications in bone tissue engineering.," *Int. J. Oral Maxillofac. Surg.*, vol. 35, no. 10, pp. 928–934, Oct. 2006.

[226] Y. Chen, S. Zhou, and Q. Li, "Mathematical modeling of degradation for bulk-erosive polymers: Applications in tissue engineering scaffolds and drug delivery systems," *Acta Biomater.*, vol. 7, no. 3, pp. 1140–1149, Mar. 2011.

[227] X. Han and J. Pan, “A model for simultaneous crystallisation and biodegradation of biodegradable polymers,” *Biomaterials*, vol. 30, no. 3, pp. 423–430, Jan. 2009.

[228] J. A. Sanz-Herrera and A. R. Boccaccini, “Modelling bioactivity and degradation of bioactive glass based tissue engineering scaffolds,” *Int. J. Solids Struct.*, vol. 48, no. 2, pp. 257–268, Jan. 2011.

[229] S. Wu, X. Liu, K. W. K. Yeung, C. Liu, and X. Yang, “Biomimetic porous scaffolds for bone tissue engineering,” *Mater. Sci. Eng. R Reports*, vol. 80, pp. 1–36, Jun. 2014.

[230] J. C. Middleton and A. J. Tipton, “Synthetic biodegradable polymers as orthopedic devices,” *Biomaterials*, vol. 21, no. 23, pp. 2335–2346, Dec. 2000.

[231] R. Huikes, M. C. H. van der Meulen, R. Huiskes, and M. C. H. der Meulen, “Why Mechanobiology?,” *J. Biomech.*, vol. 35(4), no. 4, pp. 401–414, Apr. 2002.

[232] D. J. Kelly and P. J. Prendergast, “Mechano-regulation of stem cell differentiation and tissue regeneration in osteochondral defects.,” *J. Biomech.*, vol. 38, no. 7, pp. 1413–1422, Jul. 2005.

[233] R. G. Bacabac and M. G. Mullender, “Mechanobiology of bone tissue,” *Faseb J.*, vol. 53, pp. 576–580, 2005.

[234] R. P. Gehron, “The biochemistry of bone,” *Endocrinol. Metab. Clin. North Am.*, vol. 18, no. 4, pp. 858–902, 1989.

[235] H. Cölfen, “Biomineralization: A crystal-clear view,” *Nat. Mater.*, vol. 9, no. 12, pp. 960–961, Dec. 2010.

[236] M. Olszta *et al.*, “Bone structure and formation: A new perspective,” *Mater. Sci. Eng. R Reports*, vol. 58, no. 3–5, pp. 77–116, Nov. 2007.

[237] L. Raisz, “Bone Biology: Bone Structure and Remodeling,” in *Bone Disease of Organ Transplantation*, J. Compston and E. Shane, Eds. Elsevier Inc., 2005, pp. 31–45.

[238] L. M. McNamara and P. J. Prendergast, “Bone remodelling algorithms incorporating both strain and microdamage stimuli,” *J. Biomech.*, vol. 40, no. 6, pp. 1381–1391, Jan. 2007.

[239] R. Baron, “Anatomy and ultrastructure of bone - histogenesis, growth and remodeling .,” in *Diseases of Bone and Mineral Metabolism*, F. Singer, Ed. Soth Dartmouth: MDText, 2006.

[240] C. C. Ko, M. J. Somerman, and K. A. An, “Motion and Bone Regeneration,” in *Engineering of Functional Skeletal Tissues*, F. Bronner, M. Farach, and A. Mikos,

Eds. London: Springer-Verlag, 2007, pp. 110–128.

[241] L. Geris, J. Vander Sloten, H. Van Oosterwyck, and H. Van Oosterwyck, “Mathematical modeling of bone regeneration including the angiogenic process,” *J. Biomech.*, vol. 39, no. Supplement 1, pp. S411–S412, 2006.

[242] P. V Giannoudis, T. A. Einhorn, and D. Marsh, “Fracture healing: The diamond concept,” *Injury*, vol. 38, no. Supplement 4, pp. S3–S6, Sep. 2007.

[243] N. A. Sims and J. H. Gooi, “Bone remodeling: Multiple cellular interactions required for coupling of bone formation and resorption,” *Semin. Cell Dev. Biol.*, vol. 19, no. 5, pp. 444–451, Oct. 2008.

[244] A. Parfitt, “Modeling and remodeling: how bone cells work together,” in *Vitamin D*, D. Feldman, J. Pike, and F. Glorieux, Eds. Burlington: Elsevier Academic Press, 2005, pp. 497–513.

[245] P. Pivonka *et al.*, “Model structure and control of bone remodeling: a theoretical study,” *Bone*, vol. 43, no. 2, pp. 249–263, Aug. 2008.

[246] G. R. Mundy, “Cellular and molecular regulation of bone turnover,” *Bone*, vol. 24, no. 5 Suppl, p. 35S–38S, May 1999.

[247] H. Tsurukami, “Disorder of bone quality in Paget’s disease,” *Clin. Calcium*, vol. 15, no. 6, pp. 1000–1006, Jun. 2005.

[248] S. Nomura and T. Takano-Yamamoto, “Molecular events caused by mechanical stress in bone,” *Matrix Biol.*, vol. 19, no. 2, pp. 91–96, 2000.

[249] V. Lemaire, F. L. Tobin, L. D. Greller, C. R. Cho, and L. J. Suva, “Modeling the interactions between osteoblast and osteoclast activities in bone remodeling,” *J. Theor. Biol.*, vol. 229, no. 3, pp. 293–309, Aug. 2004.

[250] C. H. Turner, “Functional determinants of bone structure: Beyond Wolff’s law of bone transformation,” *Bone*, vol. 13, no. 6, pp. 403–409, Nov. 1992.

[251] J. G. Skedros and S. L. Baucom, “Mathematical analysis of trabecular ‘trajectories’ in apparent trajectorial structures: the unfortunate historical emphasis on the human proximal femur,” *J. Theor. Biol.*, vol. 244, no. 1, pp. 15–45, Jan. 2007.

[252] R. E. Guldberg, C. S. Gemmiti, Y. Kolambkar, and B. Porter, “Physical Stress as a Factor in Tissue Growth and Remodeling,” in *Principles of Regenerative Medicine*, San Diego, Calif: Academic Press, 2008, pp. 512–535.

[253] F. Forriol, “Bone response to mechanical demand under physiological conditions,” *Rev. Esp. Cir. Ortop. Traumatol.*, vol. 45, no. 3, pp. 258–265, 2001.

[254] A. Boccaccio, A. Ballini, C. Pappalettere, D. Tullo, S. Cantore, and A. Desiate,

"Finite element method (FEM), mechanobiology and biomimetic scaffolds in bone tissue engineering," *Int. J. Biol. Sci.*, vol. 7, no. 1, pp. 112–132, Jan. 2011.

[255] M. C. H. der Meulen and R. Huiskes, "Why mecanobiology?," 2002.

[256] D. E. Ingber, "Cellular mechanotransduction: putting all the pieces together again.," *FASEB J.*, vol. 20, no. 7, pp. 811–827, May 2006.

[257] H. Isaksson, W. Wilson, C. C. van Donkelaar, R. Huiskes, and K. Ito, "Comparison of biophysical stimuli for mechano-regulation of tissue differentiation during fracture healing," *J. Biomech.*, vol. 39, no. 8, pp. 1507–1516, Jan. 2006.

[258] Weinbaum S., S. C. Cowin, and Y. Zeng, "A model for the excitation of osteocytes by mechanical loading-induced bone fluid shear stresses," *J Biom*, vol. 27, pp. 339–360, 1994.

[259] J. P. Stains and R. Civitelli, "Cell-to-cell interactions in bone," *Biochem. Biophys. Res. Commun.*, vol. 328, no. 3, pp. 721–727, Mar. 2005.

[260] C. P. Huang, C. XM, and Z. Q. Chen, "Osteocyte: The impresario in the electrical stimulation for bone fracture healing," *Med. Hypotheses*, vol. 70, pp. 287–290, 2008.

[261] E. H. Burger and J. Klein-Nulend, "Mechanotransduction in bone-role of the lacuno-canalicular network.," *FASEB J.*, vol. 13 Suppl, pp. S101-12, Jan. 1999.

[262] H. Frost, *The laws of bone structure*, 1st ed. Springfield, Ill: Charles C Thomas Publishers, 1964.

[263] H. M. Frost, "Functional determinants of bone structure: Beyond Wolff's law of bone transformation," *Angle Orthod.*, vol. 64, no. 3, pp. 175–188, Jul. 1994.

[264] H. M. Frost, "Vital biomechanics: Proposed general concepts for skeletal adaptations to mechanical usage," *Calcif. Tissue Int.*, vol. 42, no. 3, pp. 145–156, May 1988.

[265] D. R. Carter, G. S. Beaupré, N. J. Giori, and J. A. Helms, "Mechanobiology of skeletal regeneration," *Clin. Orthop. Relat. Res.*, no. 355 Suppl, pp. S41–S55, Oct. 1998.

[266] L. E. Claes and C. A. Heigele, "Magnitudes of local stress and strain along bony surfaces predict the course and type of fracture healing," *J. Biomech.*, vol. 32, no. 3, pp. 255–266, Mar. 1999.

[267] D. Lacroix and P. J. Prendergast, "A mechano-regulation model for tissue differentiation during fracture healing: analysis of gap size and loading," *J. Biomech.*, vol. 35, no. 9, pp. 1163–1171, Sep. 2002.

[268] R. Huiskes, H. Weinans, H. J. Grootenboer, M. Dalstra, B. Fudala, and T. J. Slooff, “Adaptive bone-remodeling theory applied to prosthetic-design analysis,” *J. Biomech.*, vol. 20, no. 11–12, pp. 1135–1150, Jan. 1987.

[269] F. Pauwels, “A new theory on the influence of mechanical stimuli on the differentiation of supporting tissue,” *Z. Anat. Entwicklungsgesch.*, vol. 121, pp. 478–515, Jan. 1960.

[270] P. Prendergast, “Finite element models in tissue mechanics and orthopaedic implant design,” *Clin. Biomech.*, vol. 12, no. 6, pp. 343–366, Sep. 1997.

[271] D. P. Fyhrie and D. R. Carter, “A unifying principle relating stress to trabecular bone morphology,” *J. Orthop. Res.*, vol. 4, no. 3, pp. 304–317, Jan. 1986.

[272] J. C. Y. Dunn *et al.*, “Analysis of cell growth in three-dimensional scaffolds,” *Tissue Eng.*, vol. 12, no. 4, pp. 705–716, Apr. 2006.

[273] D. Jeong, A. Yun, and J. Kim, “Mathematical model and numerical simulation of the cell growth in scaffolds,” *Biomech. Model. Mechanobiol.*, vol. 11, no. 5, pp. 677–688, May 2012.

[274] M. Kassem, L. Ankersen, E. F. Eriksen, B. F. Clark, and S. I. Rattan, “Demonstration of cellular aging and senescence in serially passaged long-term cultures of human trabecular osteoblasts,” *Osteoporos. Int.*, vol. 7, no. 6, pp. 514–524, Jan. 1997.

[275] M. Pérez and P. Prendergast, “Random-walk models of cell dispersal included in mechanobiological simulations of tissue differentiation,” *J. Biomech.*, vol. 40, pp. 2244–2253, 2007.

[276] A. Roshan-Ghias, A. Vogel, L. Rakotomanana, and D. P. Pioletti, “Prediction of spatio-temporal bone formation in scaffold by diffusion equation,” *Biomaterials*, vol. 32, no. 29, pp. 7006–7012, Oct. 2011.

[277] D. Wilson, J. King, and H. Byrne, “Modelling scaffold occupation by a growing, nutrient-rich tissue,” *Math. Model. Methods …*, vol. 17, pp. 1721–1750, 2007.

[278] Y. Cao, G. Mitchell, A. Messina, and L. Price, “The influence of architecture on degradation and tissue ingrowth into three-dimensional poly (lactic- co-glycolic acid) scaffolds in vitro and in vivo,” *Biomaterials*, vol. 27, no. 14, pp. 2854–2864, 2006.

[279] M. W. Laschke, A. Strohe, C. Scheuer, D. Eglin, and S. Verrier, “In vivo biocompatibility and vascularization of biodegradable porous polyurethane scaffolds for tissue engineering,” *Acta Biomater.*, vol. 5, no. 6, pp. 1991–2001,

2009.

[280] A. A. Deschamps *et al.*, “In vivo and in vitro degradation of poly(ether ester) block copolymers based on poly(ethylene glycol) and poly(butylene terephthalate),” *Biomaterials*, vol. 25, no. 2, pp. 247–258, Jan. 2004.

[281] H. Tsuji and K. Ikarashi, “In vitro hydrolysis of poly(L-lactide) crystalline residues as extended-chain crystallites. Part I: long-term hydrolysis in phosphate-buffered solution at 37 degrees C,” *Biomaterials*, vol. 25, no. 24, pp. 5449–5455, Nov. 2004.

[282] C. J. Kirkpatrick *et al.*, “In vitro methodologies to evaluate biocompatibility: status quo and perspective,” *ITBM-RBM*, vol. 26, no. 3, pp. 192–199, Jun. 2005.

[283] B. Vailhé, D. Vittet, and J. J. Feige, “In vitro models of vasculogenesis and angiogenesis,” *Lab. Investig.*, vol. 81, no. 4, pp. 439–452, 2001.

[284] H. Kim, R. P. Camata, S. Chowdhury, and Y. K. Vohra, “In vitro dissolution and mechanical behavior of c-axis preferentially oriented hydroxyapatite thin films fabricated by pulsed laser deposition,” *Acta Biomater.*, vol. 6, no. 8, pp. 3234–3241, Aug. 2010.

[285] P. Buma, W. Schreurs, and N. Verdonschot, “Skeletal tissue engineering - from in vitro studies to large animal models,” *Biomaterials*, vol. 25, no. 9, pp. 1487–1495, Apr. 2004.

[286] Y. Kang *et al.*, “A study on the in vitro degradation properties of poly(L-lactic acid)/beta-tricalcuim phosphate (PLLA/beta-TCP) scaffold under dynamic loading,” *Med. Eng. Phys.*, vol. 31, no. 5, pp. 589–594, Jun. 2009.

[287] C. A. Chung, T.-H. Lin, S.-D. Chen, and H.-I. Huang, “Hybrid cellular automaton modeling of nutrient modulated cell growth in tissue engineering constructs,” *J. Theor. Biol.*, vol. 262, no. 2, pp. 267–278, Jan. 2010.

[288] J.-T. Schantz, A. Brandwood, D. W. Hutmacher, H. L. Khor, and K. Bittner, “Osteogenic differentiation of mesenchymal progenitor cells in computer designed fibrin-polymer-ceramic scaffolds manufactured by fused deposition modeling,” *J. Mater. Sci. Mater. Med.*, vol. 16, no. 9, pp. 807–819, Sep. 2005.

[289] R. Voronov, S. VanGordon, V. I. Sikavitsas, and D. V Papavassiliou, “Computational modeling of flow-induced shear stresses within 3D salt-leached porous scaffolds imaged via micro-CT,” *J. Biomech.*, vol. 43, no. 7, pp. 1279–1286, May 2010.

[290] J. Pierre, B. David, K. Oudina, H. Petite, C. Ribreau, and C. Oddou, “Modeling of large bone implant culture in a perfusion bioreactor,” *J. Biomech.*, vol. 39, no.

Supplement 1, pp. S220–S220, 2006.

[291] P. Miranda, A. Pajares, and F. Guiberteau, “Finite element modeling as a tool for predicting the fracture behavior of robocast scaffolds,” *Acta Biomater.*, vol. 4, no. 6, pp. 1715–1724, Nov. 2008.

[292] S. V Komarova, “Bone remodeling in health and disease: lessons from mathematical modeling,” *Ann. N. Y. Acad. Sci.*, vol. 1068, pp. 557–559, Apr. 2006.

[293] J. A. Sanz-Herrera and E. Reina-Romo, “Cell-biomaterial mechanical interaction in the framework of tissue engineering: insights, computational modeling and perspectives,” *Int. J. Mol. Sci.*, vol. 12, no. 11, pp. 8217–8244, Jan. 2011.

[294] J. A. Sanz-Herrera, J. M. García-Aznar, and M. Doblaré, “On scaffold designing for bone regeneration: A computational multiscale approach,” *Acta Biomater.*, vol. 5, no. 1, pp. 219–229, Jan. 2009.

[295] H. Kang, C.-Y. Lin, and S. J. Hollister, “Topology optimization of three dimensional tissue engineering scaffold architectures for prescribed bulk modulus and diffusivity,” *Struct. Multidiscip. Optim.*, vol. 42, no. 4, pp. 633–644, May 2010.

[296] D. Lacroix, J. A. Planell, and P. J. Prendergast, “Computer-aided design and finite-element modelling of biomaterial scaffolds for bone tissue engineering,” *Philos. Trans. A. Math. Phys. Eng. Sci.*, vol. 367, no. 1895, pp. 1993–2009, May 2009.

[297] J. A. Sanz-Herrera, J. M. García-Aznar, and M. Doblaré, “A mathematical approach to bone tissue engineering.,” *Philos. Trans. A. Math. Phys. Eng. Sci.*, vol. 367, no. 1895, pp. 2055–2078, May 2009.

[298] D. P. Byrne, P. J. Prendergast, and D. J. Kelly, “Optimisation of scaffold porosity using a stochastic model for cell proliferation and migration in mechanobiological simulations,” *J. Biomech.*, vol. 39, no. Supplement 1, pp. S413–S414, 2006.

[299] P. Swider *et al.*, “Use of high-resolution MRI for investigation of fluid flow and global permeability in a material with interconnected porosity,” *J. Biomech.*, vol. 40, no. 9, pp. 2112–2118, 2007.

[300] W. A. Comisar, N. H. Kazmers, D. J. Mooney, and J. J. Linderman, “Engineering RGD nanopatterned hydrogels to control preosteoblast behavior: A combined computational and experimental approach,” *Biomaterials*, vol. 28, no. 30, pp. 4409–4417, Oct. 2007.

[301] V. J. Chen, L. a Smith, and P. X. Ma, “Bone regeneration on computer-designed nano-fibrous scaffolds,” *Biomaterials*, vol. 27, no. 21, pp. 3973–3979, Jul. 2006.

[302] K. Karunratanakul, J. Schrooten, and H. Van Oosterwyck, “Finite element

modelling of a unilateral fixator for bone reconstruction: Importance of contact settings," *Med. Eng. Phys.*, vol. 32, no. 5, pp. 461–467, Jun. 2010.

[303] J. Sanz-Herrera, J. García-Aznar, and M. Doblaré, "Micro-macro numerical modelling of bone regeneration in tissue engineering," *Comput. Methods Appl. Mech. Eng.*, vol. 197, no. 33–40, pp. 3092–3107, 2008.

[304] K. S. Chan, W. Liang, W. L. Francis, and D. P. Nicolella, "A multiscale modeling approach to scaffold design and property prediction," *J. Mech. Behav. Biomed. Mater.*, vol. 3, no. 8, pp. 584–593, Nov. 2010.

[305] H. Ye, D. B. Das, J. T. Triffitt, and Z. Cui, "Modelling nutrient transport in hollow fibre membrane bioreactors for growing three-dimensional bone tissue," *J. Memb. Sci.*, vol. 272, no. 1–2, pp. 169–178, Mar. 2006.

[306] T. S. Karande, J. L. Ong, and C. M. Agrawal, "Diffusion in musculoskeletal tissue engineering scaffolds: design issues related to porosity, permeability, architecture, and nutrient mixing," *Ann. Biomed. Eng.*, vol. 32, no. 12, pp. 1728–1743, Dec. 2004.

[307] D. P. Pioletti, "Biomechanical considerations can serve as design rules in the development of bone tissue engineering scaffold," *Comput. Methods Biomech. Biomed. Engin.*, vol. 12, no. 919687423, pp. 17–18, Aug. 2009.

[308] J. Sanz-Herrera, J. García-Aznar, and M. Doblaré, "A mathematical model for bone tissue regeneration inside a specific type of scaffold," *Biomech. Model. Mechanobiol.*, vol. 7, no. 5, pp. 355–366, 2008.

[309] F. Galbusera and L. Bertolazzi, "Combined computational study of mechanical behaviour and drug delivery from a porous, hydroxyapatite-based bone graft," *Biomech. Model. Mechanobiol.*, vol. 8, no. 3, pp. 209–216, 2009.

[310] X. Liu and G. L. Niebur, "Bone ingrowth into a porous coated implant predicted by a mechano-regulatory tissue differentiation algorithm," *Biomech. Model. Mechanobiol.*, vol. 7, no. 4, pp. 335–344, Aug. 2008.

[311] C. A. Narváez-Tovar and D. A. Garzón-Alvarado, "Computational modeling of the mechanical modulation of the growth plate by sustained loading.," *Theor. Biol. Med. Model.*, vol. 9, p. 41, Jan. 2012.

[312] C. Gorriz, F. Ribeiro, J. M. Guedes, and P. R. Fernandes, "A Biomechanical Approach for Bone Regeneration inside Scaffolds," *Procedia Eng.*, vol. 110, pp. 82–89, 2015.

[313] D. J. Yoo, "Porous scaffold design using the distance field and triply periodic

minimal surface models.," *Biomaterials*, vol. 32, no. 31, pp. 7741–54, Nov. 2011.

[314] X. Wang, E. Wenk, X. Zhang, L. Meinel, G. Vunjak-Novakovic, and D. L. Kaplan, "Growth factor gradients via microsphere delivery in biopolymer scaffolds for osteochondral tissue engineering," *J. Control. Release*, vol. 134, no. 2, pp. 81–90, 2009.

[315] D. A. Wahl and J. T. Czernuszka, "Collagen-hydroxyapatite composites for hard tissue repair," *Eur. Cell. Mater.*, vol. 11, pp. 43–56.

[316] D. Chappard, L. Terranova, R. Mallet, and P. Mercier, "3D Porous Architecture of Stacks of β-TCP Granules Compared with That of Trabecular Bone: A microCT, Vector Analysis, and Compression Study.," *Front. Endocrinol. (Lausanne).*, vol. 6, no. 161, p. 8, Jan. 2015.

[317] D. A. Garzón-Alvarado, M. A. Velasco, and C. A. Narváez-Tovar, "Self-Assembled Scaffolds Using Reaction–Diffusion Systems: a Hypothesis for Bone Regeneration," *J. Mech. Med. Biol.*, vol. 11, no. 1, pp. 1–36, 2011.

[318] A. Gierer and H. Meinhardt, "A theory of biological pattern formation," *Kybernetik*, vol. 12, no. 1, pp. 30–39, Dec. 1972.

[319] S. Miyazawa, M. Okamoto, and S. Kondo, "Blending of animal colour patterns by hybridization," *Nat. Commun.*, vol. 1, no. 66, p. 6, Jan. 2010.

[320] A. De Wit, P. Borckmans, and G. Dewel, "Twist grain boundaries in three-dimensional lamellar Turing structures," *Proc. Natl. Acad. Sci. U. S. A.*, vol. 94, no. 24, pp. 12765–12768, Nov. 1997.

[321] W. E. Lorensen and H. E. Cline, "Marching cubes: A high resolution 3D surface construction algorithm," *ACM SIGGRAPH Comput. Graph.*, vol. 21, no. 4, pp. 163–169, Aug. 1987.

[322] C. M. Murphy, M. G. Haugh, and F. J. O'Brien, "The effect of mean pore size on cell attachment, proliferation and migration in collagen-glycosaminoglycan scaffolds for bone tissue engineering," *Biomaterials*, vol. 31, no. 3, pp. 461–466, Jan. 2010.

[323] H. N. Chia and B. M. Wu, "Recent advances in 3D printing of biomaterials," *J. Biol. Eng.*, vol. 9, no. 1, p. 4, Mar. 2015.

[324] R. Bibb, D. Thompson, and J. Winder, "Computed tomography characterisation of additive manufacturing materials," *Med. Eng. Phys.*, vol. 33, no. 5, pp. 590–596, Jun. 2011.

[325] J. R. Woodard *et al.*, "The mechanical properties and osteoconductivity of

hydroxyapatite bone scaffolds with multi-scale porosity," *Biomaterials*, vol. 28, no. 1, pp. 45–54, Jan. 2007.

[326] T. Dutta Roy, J. L. Simon, J. L. Ricci, E. D. Rekow, V. P. Thompson, and J. R. Parsons, "Performance of hydroxyapatite bone repair scaffolds created via three-dimensional fabrication techniques," *J. Biomed. Mater. Res. A*, vol. 67, no. 4, pp. 1228–1237, Dec. 2003.

[327] T. M. G. Chu, D. G. Orton, S. J. Hollister, S. E. Feinberg, and J. W. Halloran, "Mechanical and in vivo performance of hydroxyapatite implants with controlled architectures," *Biomaterials*, vol. 23, no. 5, pp. 1283–1293, Mar. 2002.

[328] B. B. Mandal, A. Grinberg, E. S. Gil, B. Panilaitis, and D. L. Kaplan, "High-strength silk protein scaffolds for bone repair," *Proc. Natl. Acad. Sci. U. S. A.*, vol. 109, no. 20, pp. 7699–7704, May 2012.

[329] T. P. Kunzler, T. Drobek, M. Schuler, and N. D. Spencer, "Systematic study of osteoblast and fibroblast response to roughness by means of surface-morphology gradients," *Biomaterials*, vol. 28, no. 13, pp. 2175–2182, Apr. 2007.

[330] S. Lenhert, M.-B. Meier, U. Meyer, L. Chi, and H. P. Wiesmann, "Osteoblast alignment, elongation and migration on grooved polystyrene surfaces patterned by Langmuir-Blodgett lithography," *Biomaterials*, vol. 26, no. 5, pp. 563–570, Feb. 2005.

[331] A. L. Oliveira *et al.*, "Aligned silk-based 3-D architectures for contact guidance in tissue engineering," *Acta Biomater.*, vol. 8, no. 4, pp. 1530–1542, Apr. 2012.

[332] K. W. Luczynski, T. Brynk, B. Ostrowska, W. Swieszkowski, R. Reihsner, and C. Hellmich, "Consistent quasistatic and acoustic elasticity determination of poly-L-lactide-based rapid-prototyped tissue engineering scaffolds," *J. Biomed. Mater. Res. A*, vol. 101, no. 1, pp. 138–144, Jan. 2013.

[333] S. C. Cowin and L. Cardoso, "Fabric dependence of wave propagation in anisotropic porous media," *Biomech. Model. Mechanobiol.*, vol. 10, no. 1, pp. 39–65, 2011.

[334] É. Lakatos, L. Magyar, and I. Bojtár, "Material Properties of the Mandibular Trabecular Bone," *J. Med. Eng.*, vol. 2014, no. ID 470539, p. 7, Jan. 2014.

[335] D. B. Burr, R. B. Martin, M. B. Schaffler, and E. L. Radin, "Bone remodeling in response to in vivo fatigue microdamage," *J. Biomech.*, vol. 18, no. 3, pp. 189–200, Jan. 1985.

[336] W. C. Hayes, S. J. Piazza, and P. K. Zysset, "Biomechanics of fracture risk

prediction of the hip and spine by quantitative computed tomography," *Radiol. Clin. North Am.*, vol. 29, no. 1, pp. 1–18, Jan. 1991.